Absolute Value of the Magnetic Penetration Depth and Field Profile in the Meissner State of Exotic Superconductors

With concentration on YBCO and Pnictides

by

Md Masrur Hossain

M.Sc., The University of British Columbia, 2006

A Thesis Submitted In Partial Fulfillment
Of The Requirements For The Degree Of

Doctor of Philosophy

in

The Faculty Of Graduate Studies
(Physics)

THE UNIVERSITY OF BRITISH COLUMBIA
(Vancouver)

April 2012

Abstract

One of the fundamental quantities of a superconductor is the London penetration depth, λ, which is the characteristic length scale that a magnetic field penetrates into the surface of a superconductor while in the Meissner state. In the clean limit the absolute value of λ is directly related to the superfluid density n_s via $1/\lambda^2 = \mu_0 e^2 n_s/m$ and consequently its variation as a function of temperature, doping and orientation are of central importance in testing microscopic theories of exotic superconductors. Low energy($\leq$ 30 keV) μSR beam of muon (μ^+) such as in Paul Scherrer Instituit (PSI), Switzerland, is ideal to measure London penetration depth λ. When a muon (μ^+) decays, it emits a fast decay positron preferentially along the direction of its spin due to the parity violating decay. The time evolution of statistical average direction of the spin polarization of the muon ensemble depends very sensitively on the spatial distribution and dynamical fluctuations of the muons' magnetic environment.

In this thesis, accurate measurements of λ and the anisotropies$\left(\equiv \lambda_a/\lambda_b\right)$ have been done for three different oxygen ($x = 6.52, 6.92, 6.998$) contents of $YBa_2Cu_3O_{6+x}$ and for $Ba(Co_{0.07}Fe_{0.93})_2As_2$. The measured values of λ and the anisotropies are considerably different from that of literature, often found with indirect methods. We observe an exponential decay of the magnetic field and corresponding supercurrent density deep inside the crystals. Small deviations from the London model are observed which indicate there is a suppression of the supercurrent density close to the surface. The measured (λ) values are also found to depart substantially from the widely reported relation $\left(T_c \propto 1/\lambda_a^2\right)$.

Preface

Results presented in section 4.1.1 has been published [1], under the title "Direct measurement of the London penetration depth in $YBa_2Cu_3O_{6.92}$ using low-energy μSR " with me being the second author. Sections 4.1.2 and 4.1.3 are currently in the process of being published. The design of research methods, literature review, data analysis, were done by myself in consultation with my supervisor R. F. Kiefl. Manuscript of the published paper [1] was written primarily by R. F. Kiefl. The co-authors have been partly involved in taking the data and reviewing and commenting on the manuscripts, or supplying the studied samples. The results presented in section 4.2 is published in Physical Review B(R) [2]. A significant of part of data analysis was done by me. Manuscript was written by O. Ofer & microwave analysis was done by J. C. Baglo.

The large majority of figures presented in this thesis are vector graphics, i.e, can be zoomed to inspect specific areas without any loss of resolution. To avoid large whitespaces in figures, they are purposefully made compact.

This document is best viewed with freely available Adobe Reader. Other suboptimal viewers (in order of pereference) are Preview (Machintosh only), Foxit Reader (Windows only), Evince (Go Forward/Backward links nonresponsive), Okular (appearance of broken lines in figures).

Table of Contents

List of Tables

List of Figures

List of Symbols

$\Delta(k,T)$	Momentum & energy dependent superconducting energy gap, page 16	eV
κ	Ginzburg-Landau parameter, page 3	
T_c	Superconducting critical temperature, page 1	K
ξ	Ginzburg-Landau coherence length, page 5	m
λ	London penetration depth, page 1	m
λ_{ab}	Average magnetic penetration depth, page 65	m
ϕ_0	Unit of flux quantum, page 5	
ψ	Superconducting order parameter, page 1	
σ	Optical conductivity, page 10	
τ	Relaxation time, page 18	
H_c	Critical magnetic field, page 3	Tesla
n_s	Superfluid density, page 5	
T^*	Strange metallic phase temperature, page 8	K
γ_μ	Muon gyromagnetic ratio, page 26	MHz/Tesla
$\mathcal{A}(t)$	Time dependent muon asymmetry, page 33	
$\mathcal{R}$	Ratio of magnetic penetration depth, ie, $\frac{\lambda_a}{\lambda_b}$, page 45	
τ_μ	Muon lifetime, page 26	s

Glossary

UBC University of British Columbia

PSI Paul Scherrer Institute, Villigen, Switzerland

CIFAR Canadian Institute for Advanced Research, Canada

TRIUMF TRI-University Meson Facility, Canada

NSERC Natural Sciences and Engineering Research Council of Canada

YBCO Yttrium barium copper oxide/$YBa_2Cu_3O_{6+x}$

FE-PNICTIDE Fe-As based superconductors

MUSR Muon spin resonance/rotation/relaxation

QCP Quantum Critical Point

HTSC High Temperature Superconductor

ODLRO Off Diagonal Long Range Order

YBCO-I $YBa_2Cu_3O_{6.92}$

YBCO-II $YBa_2Cu_3O_{6.998}$

YBCO-III $YBa_2Cu_3O_{6.52}$

Acknowledgments

First and foremost I would like to thank my supervisor Rob Kiefl and his support and advice throughout the course of my PhD. I am very grateful for his responses to my inquiries and availability during my entire stay at UBC. I would also like to thank my committee members: D. A. Bonn, M. Franz, and A. Damascelli for their comments, and for reading the thesis.

I also thank Zaher Salman and Gerald Morris who have always been very helpful in providing software expertise and acting as general UNIX/LINUX gurus. Zaher's super-fast response to queries for technical help has been invaluable in many occasions. Special thanks to D. Arseneau for letting me use the fastest computer in μSR group in TRIUMF. This has saved many precious hours of analysis time & possible frustrations. Many thanks to R. Liang for providing the YBCO samples with 3 different oxygen contents. Also thanks to AMES laboratory for providing the FE-PNICTIDE samples.

I wish also to thank my colleagues in β-NMR group. Special thanks to Susan Q. Song for helping taking magnetization data at AMPEL. A big thanks to J.C. Baglo for providing supplementary microwave analysis. My colleagues Terry Parolin, Dong Wang, Micheal Smadella, Hassan Saadaoui, Susan Q. Song, J.C. Baglo and others have spent many nights taking the actual data; for that and for the helpful discussions and good times we had together, I am very grateful.

The data in this project was taken over many years and a lot of people, other than the ones that have been already mentioned above, have helped to take shifts & helped doing supplementary analysis. I will also like to thank μSR support staff & colleagues at PSI, B. M. Wojek, T. Prokscha, A. Suter. Special thanks goes to B. M. Wojek for his critical & thorough analysis of data and valuable insight.

I would like to mention the β-NMR technical support staff R. Abasalti, D. Arseneau, K. H. Chow, S. Dunsiger, B. Hitti, C. D. P. Levy, R. Miller, M. R. Pearson, and D. Vyas.

The μSR measurements were performed at PSI. These works were supported by NSERC, CIFAR and the U.S. Department of Energy.

Finally, thanks to the writers of LaTeX and many accompanying packages, used in typesetting this thesis.

1

Introduction

1.1 Brief History Of Superconductivity

Historically superconductivity has played an important role in condensed matter physics. With the discovery of superconductivity in Hg [3], hundred years ago, it remains a very active area of research and continuing surprises. Figure 1.1 roughly shows the number of publications on the phenomenon of superconductivity in the last decade. Before the discovery of the phenomena of superconductivity, it was known that the resistivity of a metal drops with decreasing temperature. Resistivity in metals is generally attributed to electron-phonon scattering, the rate of which is proportional to the thermally excited phonons. However, the number of thermally excited phonons is finite above absolute zero and thus the resistivity is expected to be non zero at any finite temperature. Consequently, K. Onnes' discovery of virtual absence of resistivity in Mercury below 4.15K, in 1911 [4] was rather surprising. Soon after, in 1913, Lead was found to be superconducting below 7.2 K and after 17 years of this discovery, niobium was found to be superconducting at 9.2 K. The virtual absence of resistance in superconductor has been demonstrated by experiments with persistent currents in superconducting rings. Such currents have a decay time of magnitude of 10^5 years. The other important characteristic beyond zero resistivity is the phenomenon of the Meissner effect in which magnetic field is expelled ([5] figure 1.2) out of a sample when it's cooled below the so called critical temperature T_c. The phenomenon of the Meissner effect is different from perfect diamagnetism. In perfect diamagnetism, currents are generated to oppose any change in applied field. However, if the sample already had non-zero magnetic flux through it, cooling through T_c wouldn't make any change in the field whereas, in the Meissner effect, the field would be expelled from the sample when cooled below T_c. This phenomenon of the Meissner effect led London brothers [6] to propose equations to predict how the field is excluded from the sample and in particular, the field penetration near the surface. Londons' theory was later (1950) derived from the phenomenological theory of Ginzburg and Landau [7] (GL), who described superconductivity in terms of a macroscopic complex order parameter ψ which roughly dictates the extent to which a system is ordered. In the case of superconductivity, the amplitude of order parameter is proportional to superconducting electron density.

Although the phenomenological GL theory had been successful, the microscopic theory

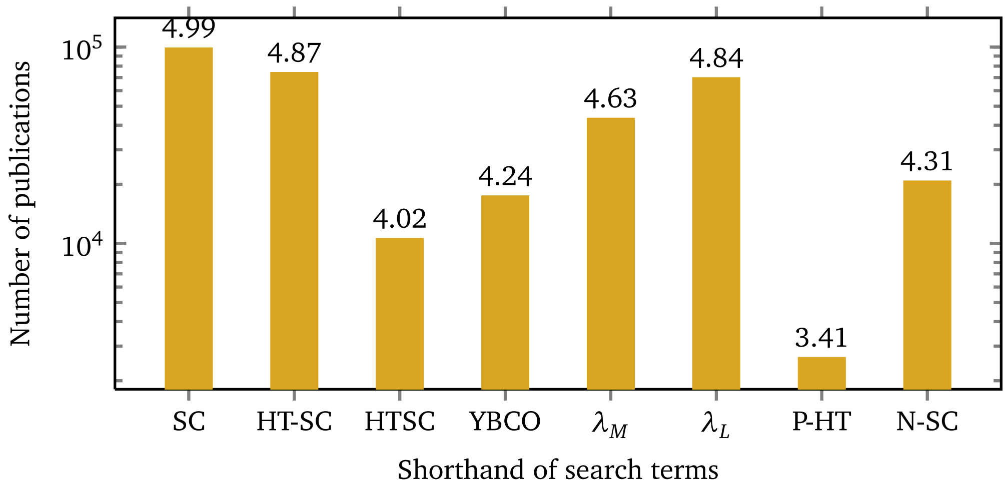

Figure 1.1: Number of publications (year 2000 onwards) in log scale, for different search terms from a prominent search engine's scholar edition, done on January 17, 2012. Expansion of the shorthand terms: SC: superconductivity; HT-SC: high temperature superconductivity; HTSC: HTSC; YBCO: YBCO; λ_M: magnetic penetration depth; λ_L: London penetration depth; P-HT: pseudogap in high temperature superconductivity; N-SC: normal state in high temperature superconductivity. As may be seen, an enormous scholarly interest in the phenomenon of superconductivity exists in the contemporary physics.

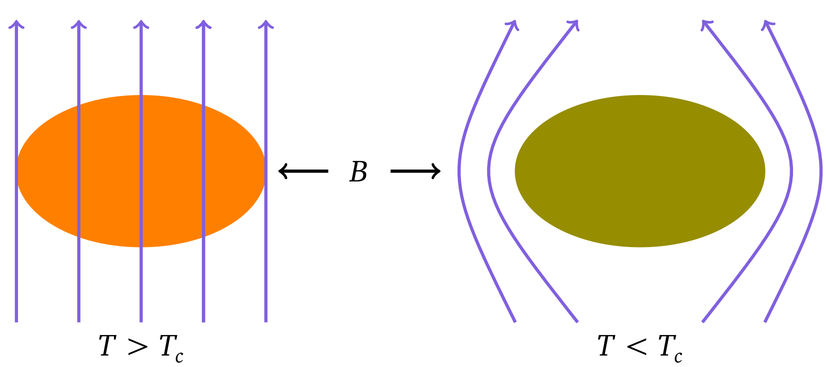

Figure 1.2: Meissner effect for a type I superconductor. When a superconductor is placed in an external magnetic field H and cooled below its superconducting temperature T_c, the magnetic flux is abruptly expelled. For $B < B_c$, it penetrates the surface of the superconductor within the penetration depth λ.

only came in 1957 from J. Bardeen, Leon Cooper and John Schrieffer [8, 9], now famously known as BCS theory. BCS theory explains superconductivity in terms of electron-electron interaction mediated by sound waves (phonons) and predicted that superconductivity may be found with critical temperature $T_c \leq 23\,\mathrm{K}$.. The carriers of supercurrents were shown to be a pair of electrons ("Cooper pairs" [10]) with opposite spin and momentum. Many new metals and alloys with superconducting properties, at low temperatures, were found by 1980, with the noted exceptions of ferromagnets such as Fe, Ni. It was later realized that magnetic order is antagonistic to superconductivity.

In 1986, J.G. Bednorz and K.A. Muller [11] discovered superconductivity in $La_{2-x}Ba_xCuO_4$ at 35K, thus initiating the era of high-temperature superconductivity. Building on that, Maw-Kuen Wu and his graduate students, Ashburn and Torng [12] at the University of Alabama discovered YBCO has a T_c of 93 K. Their work led to a rapid succession of new high temperature superconducting materials, ushering a new era in material science and chemistry. YBCO was the first family of materials to become superconducting above 77 K, the boiling point of liquid nitrogen. All materials developed before 1986 became superconducting only at temperatures near the boiling points of liquid helium (Tb = 4.2 K) or liquid hydrogen (Tb = 20.28 K) the highest being Nb_3Ge at 23 K. Although met with initial skepticism, the observations were validated when Uchida *et. al*. and Chu *et. al* reproduced original results in 1987. In 2008, one new family of Fe-based superconductors were discovered. Due to the typical antagonistic relationship of superconductivity and magnetism, this was quite surprising. Remarkable progress has been made in discovering high-T_c superconductors as shown in the figure 1.3. As superconductivity is found in so many different material families, it is considered a robust phenomenon; however high-T_c superconductivity has many open questions.

1.2 Brief Review Of Superconducting Properties

Besides having a critical temperature T_c, superconductors also have critical magnetic fields (H_c), above which their properties change. In this respect, superconductors are classified in two broad categories (figure 1.4), i) Type I, in which the material becomes normal above a critical magnetic field $H_{c,0}$. ii) Type II, in which the material has two critical magnetic fields H_{c1} and H_{c2}. In type II, at $H < H_{c1}$, the material remains in the Meissner state and at $H_{c1} < H < H_{c2}$, magnetic field penetrate the material in quantized vortices (for a very detailed review, consult [14]) and for $H > H_{c2}$, it becomes normal. Two other parameters characterize superconductivity in general, namely the coherence length ξ and the magnetic penetration depth λ. The coherence length ξ is the distance over which order parameter ψ varies appreciably and penetration depth λ is the depth over which shielding currents circulate to expel the applied external field. λ and ξ are two fundamental length scales in superconductivity. Other parameters of interest such as Ginzburg-Landau parameter $\kappa = \frac{\lambda}{\xi}$, two critical fields H_{c1}, H_{c2}, thermodynamical critical field H_c may be derived from them.

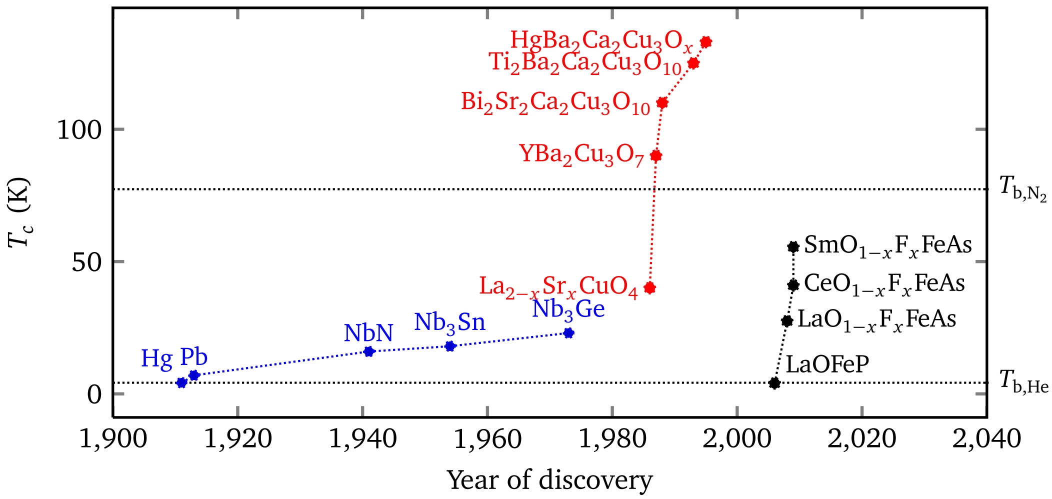

Figure 1.3: Superconducting critical temperature ([13]) T_c has risen almost linearly with time, from 4 K to 40 K till about 1986. Around 1987, one of the CuO based high temperature superconductor family was found. In 2008, one new family of Fe-based superconductors were discovered. Due to the typical antagonistic relationship of superconductivity and magnetism, this was a significant surprise for science.

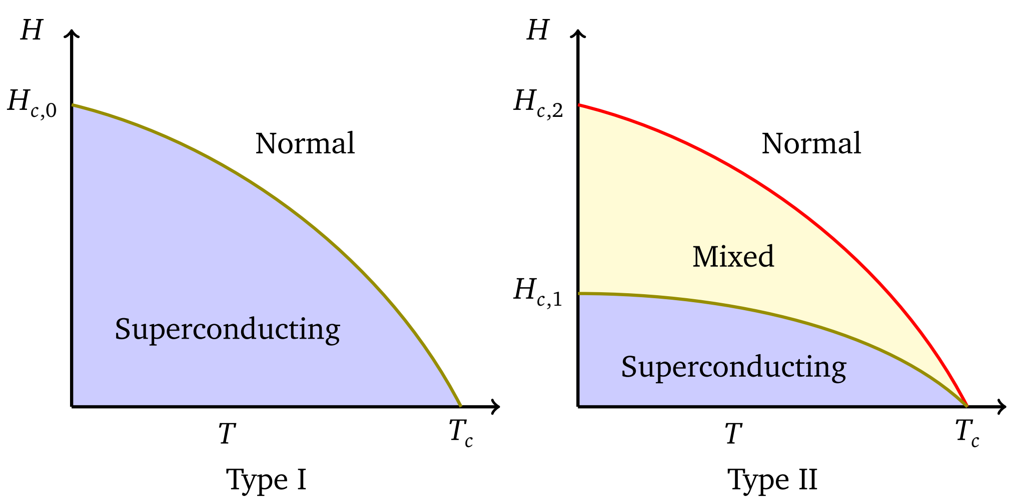

Figure 1.4: Superconductivity is destroyed when external field is too large or temperature too high. Superconductors are divided in two classes depending on the manner of this destruction. For type I superconductors, superconductivity is abruptly destroyed in a first order phase transition if $H > H_c$ or $T > T_c$. Type II superconductivity has a complete Meissner region (below $H < H_c$) in $H-T$ phase diagram, however, in the "Mixed" ($H_{c1} < H < H_{c2}$) state, laminar vortices with normal state cores enter into superconductor and superconductivity is destroyed in a continuous 2nd order phase transition to a normal state. Most high-T_c superconductors are type II.

The normal regions ("vortices") in a "mixed state" of a type II superconductor are configured to maximize surface area and minimize volume while keeping the magnetic flux constant. Abrikosov showed that this occurs if vortices are cylindrical and parallel to the local field direction. At the center of a vortex, superconductivity is completely destroyed, i.e, order parameter $|\psi|^2$ vanishes (figure 1.5). However, the velocity of the carriers tend to increase as we approach the core. Within a radial distance of ξ, carrier density n_s reaches its bulk value. The radius ξ is known as "vortex core" and contains exactly one quantum of magnetic flux $\phi_0 = \frac{c\hbar}{2e}$. The supercurrent flowing around the vortex produces a magnetic field which is maximum at the center and decays approximately exponentially, with a length scale of λ in the radial direction. The vortices are usually arranged in a periodic lattice known as the Abrikosov lattice, the flux lattice or the flux line lattice. Vortices may also be dynamic and interacting depending on the level of doping and the magnetic field [15].

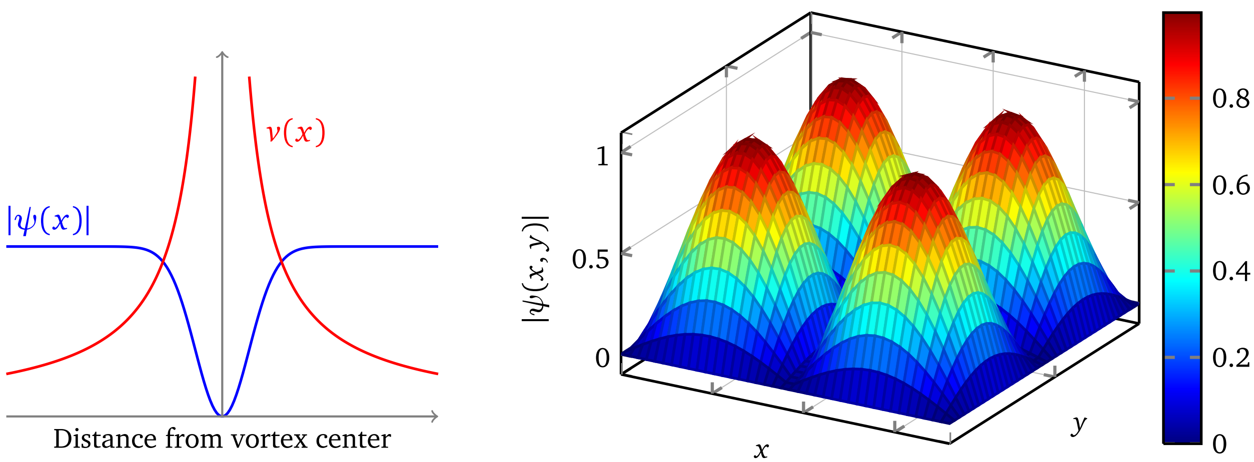

(a) **(b)**

Figure 1.5: Left: A schematic model of the electronic/magnetic structure of the HTSC vortex core. Superfluid velocity $v(x)$ rises and the HTSC order parameter $|\psi(x)|$ falls as the core is approached. Right: The superconducting order is suppressed at the cores of the vortices. The colored surface shows the envelope of this order parameter, superimposed on the vortex lattice. This type of order can be static or dynamically fluctuating depending on the level of doping and the magnetic field.

1.3 High Temperature Superconductivity: A Review

1.3.1 Cuprates: CuO_2 Layer Based High-T_c Superconductor

Discovery of superconductivity in the ceramic materials (with copper oxides) has led to a pursuit to understand this new phenomenon. This new type of superconductivity is considerably different from the "conventional" (i.e, BCS)-type superconductivity & exact microscopic mechanism is so far debated. However, significant inroads have been made in understanding different aspects of this "unconventional" superconductivity.

A traditional description of electronic behavior in solids is modeled after Drude, Sommerfield, Wiedemann and Franz, where heavier positively charged cores of atoms form periodic lattice and are immobile and electrons are almost free as in gas molecules in a jar, aptly named as “free electron gas”. This theory is also known as Landau’s “Fermi-liquid theory”. The Wiedemann-Franz (WF) law (an empirical observation) is one of the basic properties of a Fermi liquid, reflecting the fact that the ability of a “free electron” to transport heat is the same as its ability to transport charge, provided it cannot lose energy through collisions and is written as

$$\frac{k}{\sigma T} = \frac{\pi^2}{3}\left(\frac{k_B}{e}\right)^2 = \text{constant} \tag{1.1}$$

where k and σ are the heat/electrical conductivity, repectively. In high-T_c cuprate superconductor $(Pr,Ce)_2CuO_4$, the WF law is violated in the normal state, suggesting that elementary excitation that carry heat in this material are not fermions[16]. The Fermi-liquid description is highly successful in explaining metallic, insulating and semiconducting behavior, however fails to account for unconventional superconductivity where electron-electron interaction is too strong. Strong Coloumb repulsion among electrons lead to antiferromagnetic Mott insulating behavior in CuO materials at a composition where “free electron gas” theory predicts a metal. Changes in composition (O doping) leads to many exotic phenomenon such as superconductivity, charge ordering, strange metallicity, quantum criticality and Fermi liquid phenomenon. A Mott insulator is very different from a regular (band) insulator. In a band insulator, lack of conductivity arises due to Pauli exclusion principle as the highest occupied band contains two electrons per unit cell and all the orbitals are filled. In a Mott insulator, due to strong Coloumb repulsion, charge conduction is blocked, leaving charge per unit cell fixed with electron spins fluctuating at each site. This fluctuation is antiferromagnetic (figure 1.8) in nature. Doping (hole/electron) restores some electrical conductivity by creating sites to which electrons can jump without having to gain additional Coloumb energy.

High-temperature superconductivity arises in a family of layered copper oxides that all feature weakly coupled square-planar sheets of CuO_2. Structure of one of the member of this family, $YBa_2Cu_3O_{7-\delta}$ (hereafter “YBCO”, possibly the most studied) is shown in figure 1.6, as this material was a subject of this research. For $YBa_2Cu_3O_7$, three copper-oxygen layers are stacked along the tetragonal $\hat{\mathbf{c}}$ axis. Two of these layers have oxygen atoms between the copper ions in both the $\hat{\mathbf{a}}$ and $\hat{\mathbf{b}}$ directions, and are called CuO_2 plane layers. The third layer, called the CuO chain layer, has oxygen ions only along the $\hat{\mathbf{b}}$ direction [19]. The phase diagram for YBCO, dependent on oxygen(hole) doping, is shown schematically in figure 1.7. As may be noted from the phase diagram, with increased hole doping, antiferromagnetic insulating state turns to be superconducting. The dependence of critical temperature $T_c(p)$

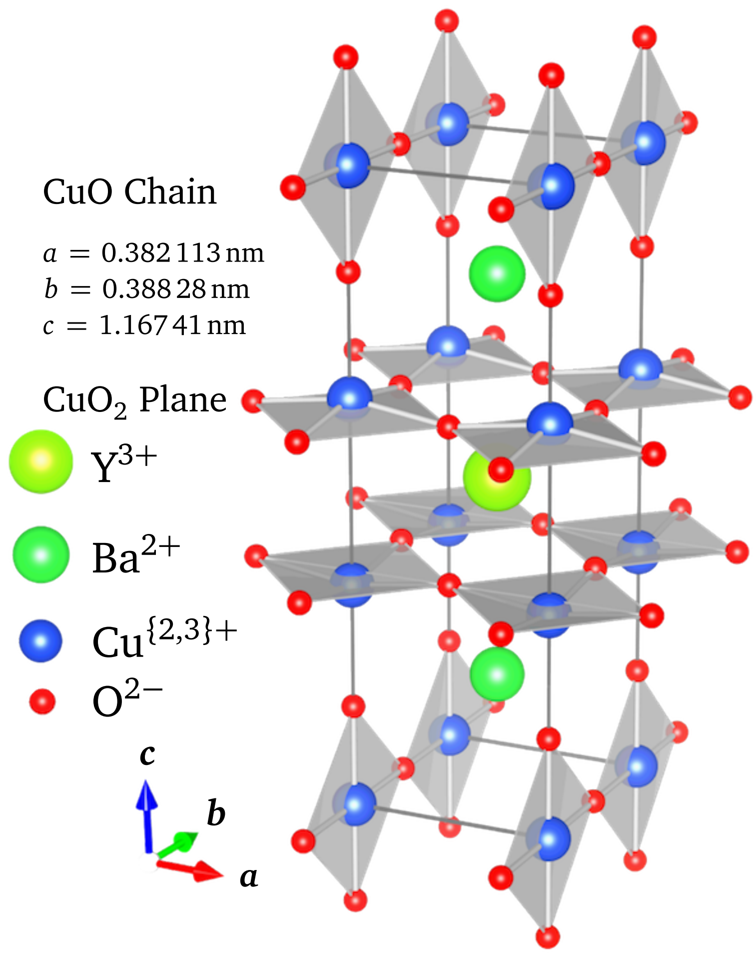

Figure 1.6: YBCO consists of CuO_2 planes & CuO chains. Each plane layer consists of a single Cu atom sharing with four Oxygen vertices and perpendicular to these CuO_2 planes, are CuO chains where each Cu atom shares two oxygen vertices. The Ytrrium atoms are found between CuO_2 planes, while the Barium atoms are found between CuO_2 planes and CuO chains. $YBa_2Cu_3O_7$ is a well-defined chemical compound with a specific stoichiometry. Non-stoichiometry is defined by oxygen vacancies as in $YBa_2Cu_3O_{7-x}$. With $x = 1$, O(1) sites in CuO_2 planes are vacant and the structure is tetragonal and insulating. For $x < 0.65$, CuO chains along b-axis start to form and the structure becomes orthorhombic. Maximum $T_c \sim 95\,\mathrm{K}$ occurs for $x \sim 0.8$ [17, 18].

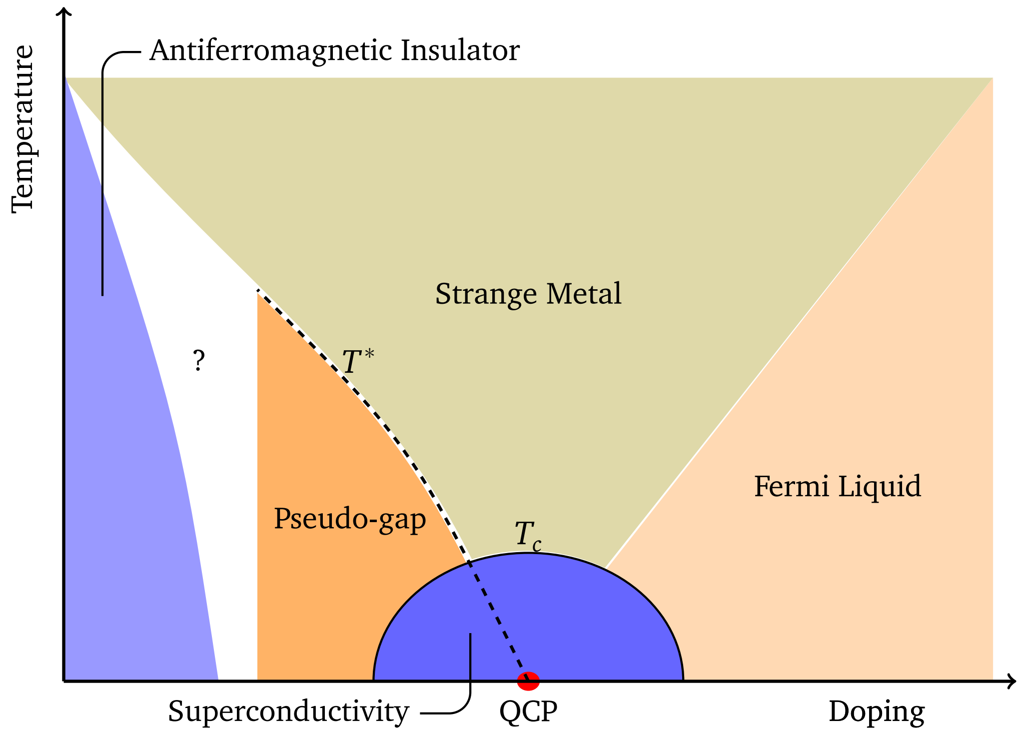

Figure 1.7: Schematic phase diagram: At very low levels of electron-hole doping, cuprates are insulating and antiferromagnetic (the materials' neighboring spins point in opposite directions). At increased doping levels, they become conducting, and the exact temperature and doping level determine which phase of matter they will be in. At temperatures below T_c, they become superconducting, and at temperatures above T_c but below T^* they fall into the pseudogap phase. The boundary of the pseudogap region at low doping levels is unknown. The transition between the Fermi-liquid phase and the strange-metal phase occurs gradually (by crossover). QCP denotes the quantum critical point at which the temperature T^* goes to absolute zero.

on doping is given by an empirical relationship [20],

$$T_c(p) = T_{c,\max}\left[1 - 82.6(p - 0.16)^2\right], \tag{1.2}$$

where doping level p varies from 0.05 to 0.27. The proximity of antiferromagnetism and superconductivity gives rise to the conjecture that superconductivity is driven by magnetic interactions between electrons rather than pairing via phonons. Also important to note that, a signature of lattice vibration driving superconductivity, ie, the "isotope effect" has not been observed in high temperature superconductivity. However there has been renewed interest in the possible role of electron-lattice coupling [21–26] in high-T_c superconductivity, although the role is suggested to be indirect [26] and small [23, 27]. A possible mechanism proposed by P. W. Anderson [28] is that "quantum fluctuations" may create instability in the antiferromagnetic order and give rise to resonating valence bond [29–31] in which the spins form a "spin-liquid" phase of singlet($s = 0$) pairs. "Spin liquid" is defined to be aggregation of pairs of antiparallel spins. The motion of such singlet pairs is similar to the resonance of π bonds in benzene, originating the term "resonating valence bond" (RVB), schematically shown in figure 1.8. In this picture, electrons are paired up in antiparallel spin-formation but cannot move due to Coloumb repulsion. Reducing average occupancy, from one, will make these singlet pairs mobile, Anderson argued, giving rise to superconductivity. In contrast, YBCO was found out to be antiferromagnets and not spin-liquid phase [32–34]. It

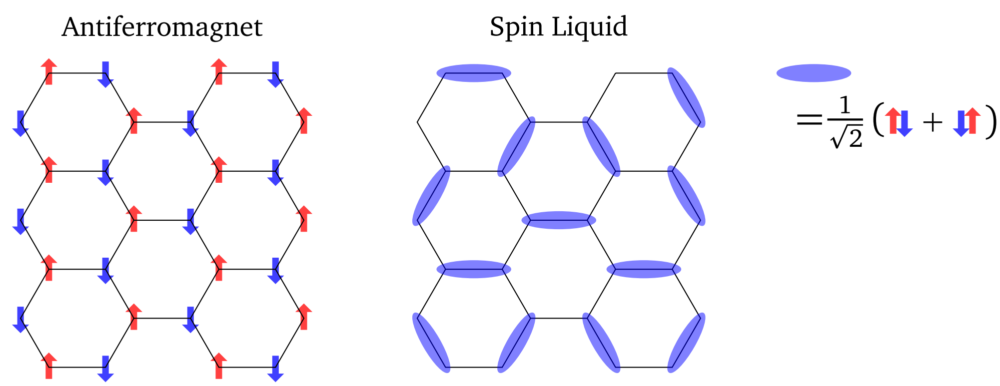

Figure 1.8: An example of a short range "resonating valence bond" (an aggregation of antiparallel neighboring spins). An oval represents a superposition of different possible spin configurations. This is a "spin-liquid" since there is no static order but their motions are highly correlated. Motions of singlet pairs are hindered due to Coloumb repulsion. Reducing average occupancy from one may make these singlet pairs mobile.

has been established that in cuprate systems, antiferromagnetic ordering resides entirely on the CuO_2 plane [35, 36], with a three-dimensional magnetic transition dictated by very weak coupling between planes. As seen in the phase diagram in figure 1.7, T_c varies (peaks at "optimal" doping) as a function of doping and is a well observed phenomenon in all CuO_2 layer based superconductors [37]. With increased doping 3D antiferromagnetic ordering gives way to a disordered state with short range correlations [37], thereby retaining some magnetism. At $T > T_c$, metallic behavior is observed for a broad range of dopings & d.c electrical resistance is T-dependent rather that T^2-dependent as would have been expected from a normal metal Fermi liquid behavior. In the overdoped regime, the copper oxides behave more like ordinary metals with a T^2 dependence of d.c resistivity [38]. A naturally overdoped Copper oxide $TlBa_2Cu_3O_{6+x}$ has been observed to show polar angular magnetoresistance oscillation [39, 40], in high field, establishing the existence of a 3D Fermi surface, consistent with the prediction from single electron band theory, i.e, metallic behavior. However, the existence of 3D coherent Fermi surface poses a challenge to the widely held belief and experimental evidence [41] that high-T_c superconductivity arises from purely 2D electron motion within the CuO_2 planes. In underdoped regime, copper oxides have been found to show quantum oscillations [42], an indication of metallic behavior, in de Haas-van Alphen spectra. As may be noted in phase diagram Cu-O based superconductors includes a "pseudogap" region [41, 43], a precursor to the superconducting state. It has been shown that this phase originates in CuO_2 planes and not in the CuO chains [44]. Whether this is a distinct phase of matter is still under debate [45]. It is metallic, however some parts of the Fermi surface show gaps [41, 43, 46].If it exists, a quantum critical point [47–49] in the cuprates would also probably be the end point of a line(T^*) [50] of phase transitions that separates the pseudogap and strange-metal regions. It has also been suggested that the phase diagram is controlled by a quantum critical point [51, 52]. A QCP develops in a material at absolute zero temperature when a new form of order emerges from it's ground state. QCP is a phenomenon of great interest because of their ability to influence the finite temperature properties of materials. The "normal" region ("strange metal") above transition temperature T_c is of very unusual properties [53–55] (thermal conductivity $k(T)$, optical conductivity $\sigma(\omega)$, the nuclear relaxation rate $T_1^{-1}(T)$), with large temperature-dependent resistivity implying a scattering rate linear in T, however several orders of magnitude of the average excitation energy $k_B T/h$ [56, 57].

With all the significant differences from conventional superconductivity, supercurrent is still carried by electron pairs, shown via quantization of magnetic flux in units of $\frac{h}{2e}$ [58–60]. Most of the physical properties of the CuO_2 have experimentally been established with a high degree of reliability and advances in preparing the materials are such that spurious effects and uncertainties in materials compositions, homogeneities and impurity content may be eliminated as hindrance to the understanding of the phenomenon of high-T_c superconductivity. In spite of substantial efforts in both experimental and theoretical research, there are many open questions regarding mechanism for high-T_c superconductivity.

1.3.2 Pnictide: A New Type Of High-T_c Superconductor

Because of the typically antagonistic relationship between superconductivity and magnetism has led researchers to avoid using magnetic elements (eg. Fe) in particular, as potential building blocks of new superconducting materials. The recent (2008) discovery of superconductivity at T_c's up to 55 K in iron pnictide systems [61–65] has sparked enormous interest in this class of materials. Even more surprising is that pnictide is the only material other than cuprates (CuO_2 layer based superconductors) to have T_c higher than 40 K (∼BCS theoretical maximum). The crystal structure of the parent compound $BaFe_2As_2$ is shown in the figure 1.9 as a Co-doped pnictide ($Ba(Co_{0.074}Fe_{0.926})_2As_2$) is a subject of this work.

Cuprates and pnictides show similar behavior in many aspects, such as (i) both are layered structures, (ii) parent (non-superconducting) compounds are antiferromagnets, although with possibly different electronic correlation strengths, (iii) both materials show superconducting order upon doping. Striking dissimilarities are also abound: (i) parent

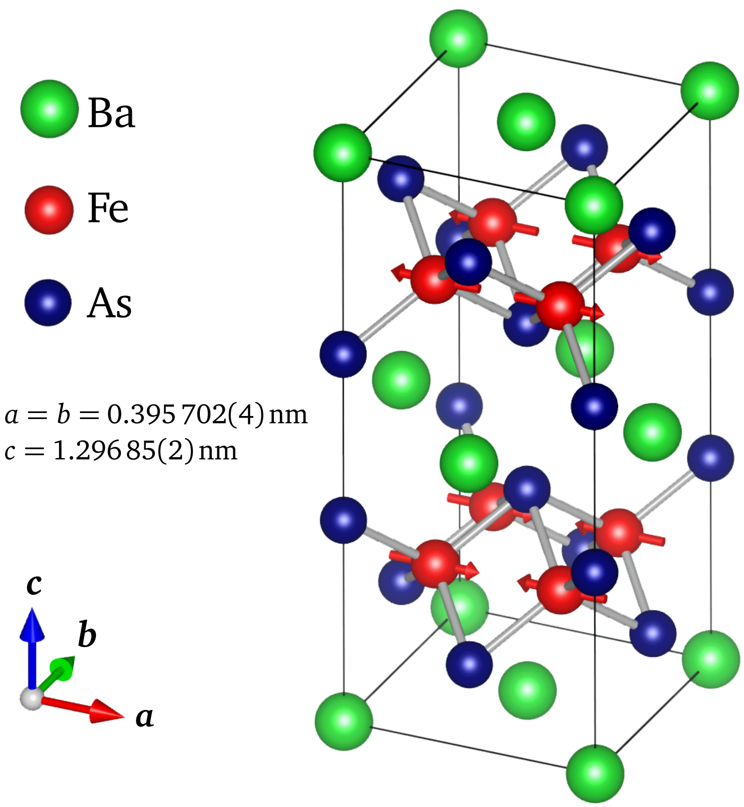

Figure 1.9: Left: Pnictide crystal structure [66] shows the antiferromagnetic alignment and magnetic moment (red arrows) both along the longer a axis in the FeAs plane. The magnetic unit cell is the same as the orthorhombic chemical unit cell.

compound for cuprates are Mott insulators while for pnictides, they are semimetals, (ii) cuprates are essentially one-band while iron pnictides have multibands at the Fermi energy, (iii) superconducting gap function is d-wave in cuprates whereas for pnictides, strong contender is an "extended s-wave", also called $s\pm$.

Two families(parent materials) of pnictides have so far been discovered: originating from RFeAsO [64] (R=rare earth, abbreviated as 1111 for its 1:1:1:1 ratio of the four elements) and AFe_2As_2 [67] (A=alkaline,the 122 compounds) earth metal, which are tetragonal at room temperature but undergo an orthorhombic distortion in the range 100 K to 200 K that is associated with the onset of antiferromagnetic order [66, 68–72]. Tuning the system via element substitution [73, 74] or oxygen deficiency [75, 76] suppresses the magnetic order and structural distortion in favor of superconducting T_c's up to 55 K, with an overall behavior strikingly similar to the high-T_c copper oxide family of superconductors. However, the induction of superconductivity by doping Co or other transition metals into the Fe site indicates that atomic disorder in the superconducting Fe layer ostensibly does not suppress superconductivity, contrary to the behaviors of layered cuprate high-T_c superconductors

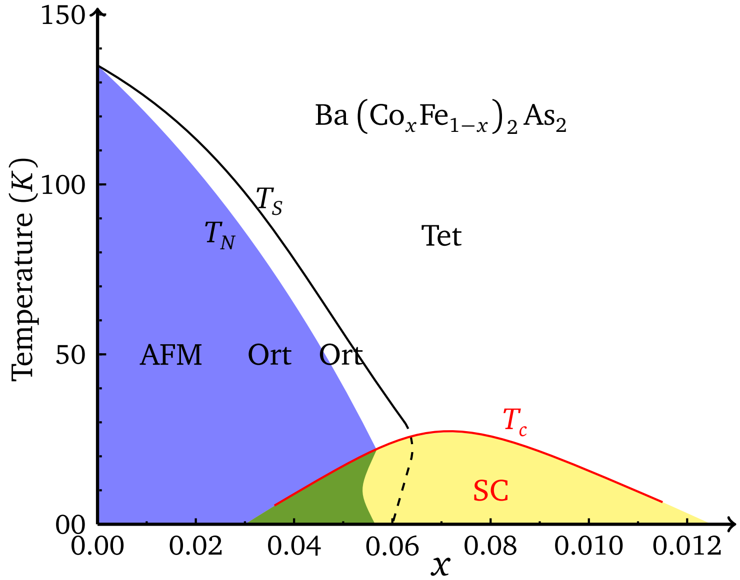

Figure 1.10: Phase diagram [77, 78] for $BaCo_xFe_{2-x}As_2$. Yellow indicates the superconducting phase, which appears below the superconducting transition temperature T_c. A structural transition occurs at T_s from the tetragonal phase (Tet) at higher temperature to the orthorhombic phase (Ort). Blue represents the antiferromagnetic order (AFM), which appears at T_N, slightly below T_s. The stripes of enhanced superfluid density are observed only in the regime $0.04 < x < 0.06$.

where doping onto the Cu sublattice is always detrimental to T_c.

A preliminary phase diagram [77, 78] of pnictide superconductors is shown in the figure 1.10. It may be noted that parent compound of superconducting iron arsenides exhibit spin density wave (SDW)-type long-range magnetic ordering at low temperatures [68, 79] just like the cuprates [32]. As it appears that in high-T_c superconductivity, AF order needs to be suppressed before superconductivity may appear, leads many to the proposition that dynamic rather than static antiferromagnetism (or AF fluctuations) is favorable for high-T_c superconductivity. A recent neutron-scattering experiment found that, in $BaFe_{1.85}Co_{0.15}As_2$, the AF fluctuation is as strong as that of $YBa_2Cu_3O_{6+x}$ [80] and electron-phonon coupling is not the primary driver of superconductivity in pnictides. Origin of antiferromagnetic ordering in the pnictide parent compounds is a hotly debated topic, largely owing to its implications for the pairing mechanism: the electronic structure suggests that the same magnetic interactions that drive the AFM ordering also produce the pairing interaction for superconductivity [81]. Regardless of the exact nature of magnetic order, it is believed that magnetostructural coupling is prevalent throughout the Fe-based superconductors in the form of coupled magnetic and structural transitions [82, 83]. Competeing presence of superconductivity and AF spin fluctuations has led to suggestions that quantum criticality may play an important role [84–86], however, prominency of quantum critical behavior in iron pnictides is disputed elsewhere [87]. Due to the large number of pnictides and the nature of chemical substitution, one limitation so far is that many experiments have been carried out on different systems or different chemical compositions of the same crystalline system, and thus make comparisons difficult. However their generic features enables general conclusions to be drawn from several experiments. For instance, NMR experiments determined from Knight shift measurements that the superconducting state spin symmetry is probably singlet [88–90], suggesting an even order parameter symmetry (eg. s wave, d wave).

1.4 Pairing Symmetry And Magnetic Penetration Depth Measurement

One fundamental quantity in characterization of superconductors is London penetration depth λ, which is closely related to superfluid density ($\rho_s \equiv \frac{1}{\lambda^2} \propto \frac{n_s}{m^*}$). In general, the penetration depth λ is given as a function of n_s, effective mass m^*, Ginzburg-Landau coherence length ξ and the mean free path l as [91]

$$\frac{1}{\lambda^2} = \frac{4\pi n_s e^2}{m^* c^2} \times \frac{1}{1+\xi/l} \tag{1.3}$$

Close to the clean limit, $\frac{\xi}{l} \to 0$ and the second term in (1.3) becomes unity. λ's variation as a function of temperature, doping and orientation are of central importance in testing microscopic theories of exotic superconductors. For example, the linear variation of $1/\lambda^2$ with respect to temperature was a key finding confirming the d-wave nature of the pairing in $YBa_2Cu_3O_{6+x}$ [92, 93]. Also, early μSR studies of the vortex phase in polycrystalline samples found a linear correlation between $1/\lambda^2$ and T_c in the under-doped region [94, 95]. The resulting Uemura plot has played a prominent role in theoretical efforts to understand high T_c superconductivity [96]. Departure from Uemura scaling and the decline of the slope as the $T_c = 0$ quantum critical point is approached can be understood in terms of a 3D-QCP model [97]. Scaling of T_c with $n_s(0)$ in underdoped cuprates may also be due to quantum fluctuations near a 2D quantum critical point [98].

It is widely believed that cuprate high-T_c superconductivity originates in two-dimensional CuO_2 layers [34, 35, 99]. $YBa_2Cu_3O_{6+x}$ also has one dimensional (1D) CuO chains which contribute to superconductivity the mechanism for which is not fully understood [100]. CuO chains are believed to act as quasi-1D system and charge reservoir [19]. Magnetic ordering of Cu moments have been observed to be at different temperatures in plane and chain layers [101]. Penetration depth anisotropy measurements indicate that chains become superconducting at the same temperature as CuO_2 planes [102]. Due to differences in band structures between planes and chains [103], one natural explanation for the same transition temperature is proximity effect [104–106] where by electron hopping between chains and planes contribute to superfluidity along chain direction. The 1D nature of the chains themselves induces, in the filled chain compound, $a-b$ anisotropy which has been observed in dc resistivity [107, 108] and optical conductivity and penetration depth measurements [102, 109] and is expected to affect the vortex core structure [104]. In this simple model of multiband superconductivity in $YBa_2Cu_3O_{7-\delta}$, there is an intrinsic pairing interaction in the plane, but the chains are intrinsically normal, which means that the superconducting order parameter is nonzero in the plane layer only [104]. The pairing mechanism of $YBa_2Cu_3O_{6+x}$ is thought to be predominantly d-wave type. Other possible pairing states involving complicated gap functions, have been suggested [110–113]. Recently discovered $BaFe_2As_2$ family of superconductors has yet to have a definitive pairing symmetry. An accurate determination of $\lambda(T)$ is one way to probe the symmetry of the pairing state. It has been theorized [114] that only low temperature dependence of $\lambda(T)$ is sensitive to pairing state of the superconductor. It is clear that accurate measurements of λ and $a-b$ anisotropy are essential in clarifying central questions in $YBa_2Cu_3O_{6+x}$.

Unfortunately, accurate measurements of λ are difficult due to systematic uncertainties. For example, in any bulk measurement the assumption of an exponential decay of the field in the Meissner state is only valid in the local London limit of a perfect surface [115]. Significant non-local effects are expected if the coherence length is comparable to the penetration depth [116] or if there are nodes in the superconducting gap function [117]. Even within the London limit, there may be a non-exponential decay of the field, arising from any depth dependent change in the magnitude or symmetry of the order parameter. These add uncertainty to all conventional bulk measurements where the field profile is assumed and not measured. Alternatively, one can determine the absolute value of λ from μSR studies in the vortex state where the muon acts as a sensitive probe of the local magnetic field distribution. However, an accurate determination of λ requires there to be a well ordered vortex lattice with known symmetry. Also, there are substantial non-local and non-linear effects associated with vortices which complicate the theory and make it difficult to extract the true λ [117–120]. One approach is to fit the observed field distribution to a simple Ginzburg-Landau model involving an effective λ and then to extrapolate to zero magnetic field (or vortex density) [121]. Until now, the penetration depth has been measured in the vortex state via muon spin rotation [122] and using microwave techniques [92, 123–125]. In vortex state measurement, Sonier *et al.* used a GL model for magnetic field distribution to extract λ as a function of applied magnetic field. However, it was mentioned that λ_{ab} measured is an effective penetration depth which is model dependent. Consequently, one may expect some difference in λ measured in the Meissner state where there are no vortices. The microwave techniques used in [92, 123–125] reported London penetration depth for a number of high-T_c superconductors. Microwave techniques are well-suited to measuring temperature dependence of λ but generally not very sensitive to the absolute value of λ.

In this thesis, a reduction of magnetic field $B(z)$ is measured as it enters the sample, via the reduction of muon spin precession frequency. The precession frequency contains all the information about muons' interaction with the local magnetic environment. Using a modified London model in the Meissner state, absolute value of magnetic penetration depths are obtained for three oxygen dopings of YBCO and a Co doped FE-PNICTIDE.

2

Theory

2.1 BCS Theory

The basic idea for BCS superconductivity is that an attractive interaction between electrons, regardless of their strength, can bind the electrons into pairs [10]. We consider a case for only two electrons added to the Fermi sea. The first electron attracts positive ions and these ions, in turn, attract the second electron giving rise to an effective attractive interaction between electrons. Due to the movement of ion cores, phonon waves are generated and the interaction between electrons is thereby phonon mediated. The total energy of the electron system is minimized when there are Cooper pairs compared to a Fermi gas with no correlation. The center of mass of a Cooper pair is zero since the electrons have opposite momenta and spin $|\hbar\vec{k},\uparrow\rangle$ and $|-\hbar\vec{k},\downarrow\rangle$. Due to this opposite momenta and spin, it is labeled s-wave pairing since the relative angular momenta of the two electrons is zero. The electron-phonon system is described by the single order parameter ψ. An schematic of "in-phase" motion of the system is shown in the figure 2.1

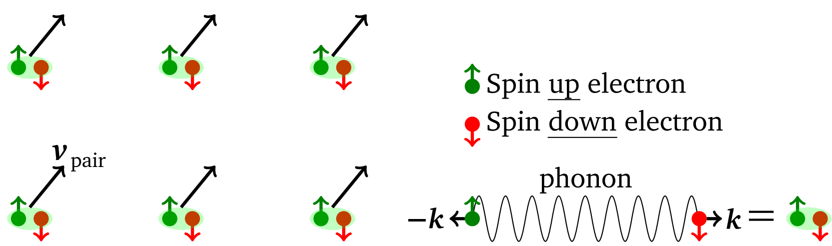

Figure 2.1: In the superconducting state, electrons pair up in zero-spin composites. They all move "in phase" and are said to be "coherent". This is considered to be a ordered state and the whole electron-phonon system may be described by a single wavefunction.

One important consequence of the BCS theory is that the presence of a momentum dependent energy gap $\Delta(k)$ at the Fermi surface so that an amount of $2\Delta(k,T)$ energy is required to break a Cooper pair. The energy gap is schematically shown in the figure 2.3. The gap is opened at the Fermi energy as the temperature is lowered below the critical temperature. A d-wave density of state is also shown in the figure 2.3. Unlike the s-wave superconductors, some carriers are always available at the Fermi surface even at the lowest temperatures. In the weak coupling limit, where the gap Δ is much smaller than the

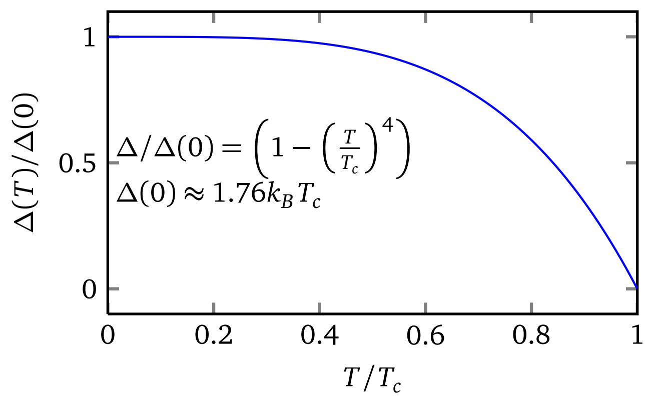

Figure 2.2: Temperature dependence of the superconducting energy gap in the weak coupling limit of BCS interaction. The superfluid density $n_s \propto$ in a two-fluid model [126] implies the (T/T_c) dependence of energy gap. This gap model is also experimentally verified [127].

characteristic phonon energy $\hbar\omega_D$,

$$\frac{2\Delta(0)}{k_B T_c} = 3.52. \tag{2.1}$$

The numerical factor 3.52 is well tested in experiments and found to be reasonable, in purely BCS type interactions. $\Delta(T)$ remains fairly constant until the phonon energy becomes enough to thermally excite the quasiparticles. Near the transition temperature T_c, $\Delta(T)$ varies as

$$\frac{\Delta(T)}{\Delta(0)} \sim 1.74 \left(1 - \frac{T}{T_c}\right)^{\frac{1}{2}}, \qquad T \sim T_c \tag{2.2}$$

and is graphically shown in the figure 2.2.

The most important manifestation of the electron-phonon interaction is the superconducting state itself. According to our present understanding of Cooper pairing, the electron-phonon induced attraction between two electrons would not overcome their direct Coulomb repulsion, except for the fact that the former is retarded whereas the latter is not. This gives rise to the pseudopotential effect; in some sense the pseudopotential effect is the true mechanism of superconductivity, rather than the electron phonon interaction per se.

2.2 London Penetration Depth

We consider the penetration depth in the Meissner state of a type II superconductor. Below H_{c1}, the London equations provide a good description of the electromagnetic properties. The relevant Maxwell's equation is

$$\vec{\nabla} \times \vec{E} = -\frac{1}{c}\frac{\partial \vec{B}}{\partial t}. \tag{2.3}$$

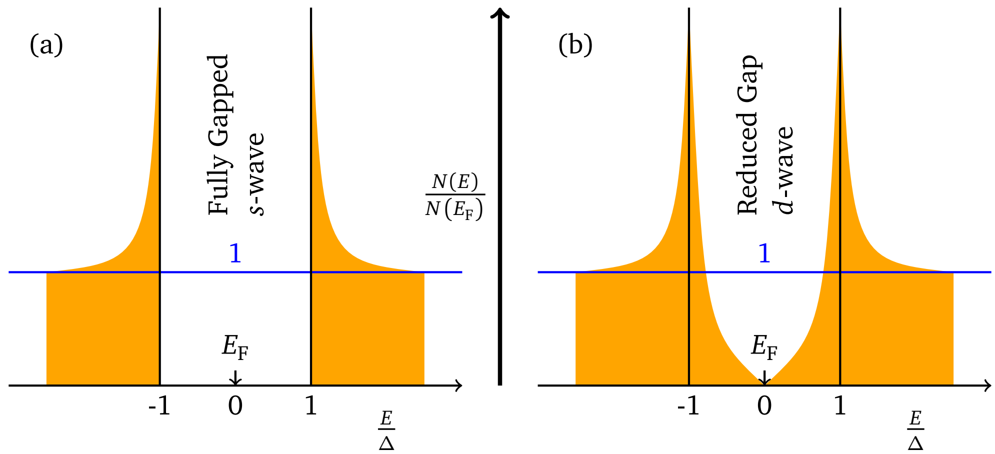

Figure 2.3: Left (s-wave): Density of states in a conventional superconductor such as Nb. The density of states is a measurement of how many electrons can reside at a specific energy level. In the figure, there is a region at the Fermi surface where no electrons can reside. This region comprises the superconducting energy gap. On either sides of this gap there are peaks in the density of states where large numbers of electrons can occupy the energy levels. Right (d-wave): Density of states in a high-T_c superconductor like YBCO. The density of states is reduced at the Fermi surface, however there is no true gap.

In the classical Drude model of electrical conductivity, we have

$$\vec{F} = -m\frac{\vec{v}}{\tau} - e\vec{E} = m\frac{d\vec{v}}{dt}, \tag{2.4}$$

where $\vec{v}$ is the average velocity of the electrons, m is the mass of an electron, $\vec{E}$ is the electric field the electrons are in and τ is the relaxation time, i.e, roughly the time required to bring the drift velocity to zero if electric field was suddenly set to zero. In a normal metal, the competition between the scattering and the acceleration in (2.4) leads to a steady state average velocity

$$\vec{v} = \frac{e\vec{E}\tau}{m}. \tag{2.5}$$

Assuming n conduction electrons per unit volume, we get the electric current density via Ohm's Law,

$$\vec{J} = ne\vec{v} = \left(\frac{ne^2\tau}{m}\right)\vec{E} = \sigma\vec{E}. \tag{2.6}$$

To describe superconductivity, London assumed that a certain fraction of electron density n_s experience no relaxation i.e., letting τ_s in (2.4) go to infinity. This leads to

$$\frac{d\vec{J}_s}{dt} = \left(\frac{n_s e^2}{m}\right)\vec{E}, \tag{2.7}$$

where n_s is density of the superconducting carriers. Taking curl on both side of the (2.7), we get

$$\frac{m}{n_s e^2}\left(\vec{\nabla}\times\frac{d\vec{J}_s}{dt}\right)=\vec{\nabla}\times\vec{E}. \tag{2.8}$$

Substituting Maxwell (2.3) in (2.8), we obtain the second London equation

$$\frac{mc}{n_s e^2}\left(\vec{\nabla}\times\frac{d\vec{J}_s}{dt}\right)+\frac{d\vec{B}}{dt}=0. \tag{2.9}$$

Interchanging the order of differentiation with respect to space and time in (2.9), London postulated

$$\frac{mc}{n_s e^2}\left(\vec{\nabla}\times\vec{J}_s\right)+\vec{B}=0. \tag{2.10}$$

Assuming no time varying electric field, another Maxwell equation connects $\vec{J}_s$ with $\vec{B}$ with the equation

$$\vec{J}_s=\frac{c}{4\pi}\left(\vec{\nabla}\times\vec{B}\right) \tag{2.11}$$

Substituting (2.11) into (2.10), we get

$$\begin{aligned}\lambda^2\left(\vec{\nabla}\times\vec{\nabla}\times\vec{B}\right)+\vec{B}&=0,\\ \lambda^2\nabla^2\vec{B}+\vec{B}&=0,\end{aligned} \tag{2.12}$$

where

$$\frac{1}{\lambda^2}=\frac{4\pi n_s e^2}{mc^2}. \tag{2.13}$$

In a vacuum-superconductor interface (which is also the case in our experiment), the solution of (2.12) is given by

$$B(x)=B_0\exp\left(-\frac{x}{\lambda}\right) \tag{2.14}$$

where B_0 is the magnitude of the external applied field. The quantity λ is known as London penetration depth and $\lambda^{-2}\propto n_s$. The most important success of the London (2.11) and (2.12) is that a static magnetic field is screened from the interior of a bulk superconductor over a characteristic penetration depth λ. A simple estimate shows that this distance is a macroscopical one that is much larger than the mean distance r between electrons in the superconductor. As one approaches the critical temperature T_c, $n_s\to 0$ continuously and as a consequence, $\lambda(T)$ diverges as $T\to T_c$, according to (2.13). While the (2.14) may be valid for a superconductor with an atomically flat surface, a rough surface might give rise to a suppressed order parameter for few tens of nanometers and a modified London model

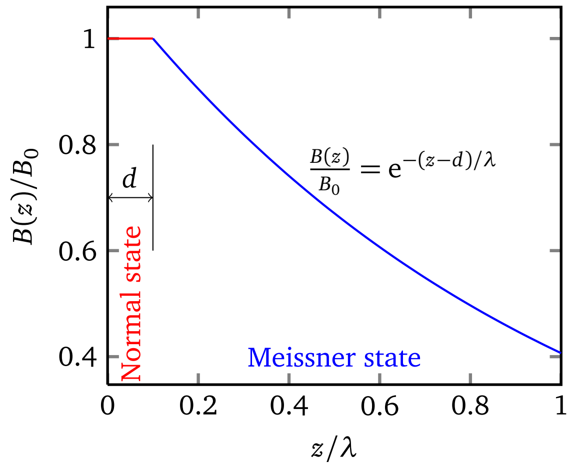

Figure 2.4: External magnetic field drops exponentially ((2.15)) as it enters a superconductor in Meissner state. The characteristic distance λ is called the London penetration depth

(figure 2.4)

$$B(z) = \begin{cases} B_0 \exp\left(-\dfrac{z-d}{\lambda}\right) & \text{if } z \geq d \\ B_0 & \text{if } z < d \end{cases} \tag{2.15}$$

may be more appropriate. Here B_0 is the magnitude of the applied field, $\lambda_{a,b}$ is the magnetic penetration depth in the a or b direction, respectively, z is the depth into the crystal, and d is an effective dead layer inside of which the supercurrent density is suppressed.

2.3 Pairing Mechanism And Order parameter symmetry

The critical temperature T_c is the onset of long-range, macroscopic phase coherence in the Cooper pairs. Long range correlations between pairs are described by off-diagonal long-range order (ODLRO) [128, 129], with no classical analog, which implies non-zero value of the the pair correlation function

$$\begin{aligned}\boldsymbol{\rho}(\vec{r},\vec{r}\,') &= \left\langle \boldsymbol{\psi}_\downarrow^\dagger(\vec{r})\boldsymbol{\psi}_\uparrow^\dagger(\vec{r})\boldsymbol{\psi}_\downarrow(\vec{r}\,')\boldsymbol{\psi}_\uparrow(\vec{r}\,')\right\rangle \\ &= \left\langle \boldsymbol{\psi}_\downarrow^\dagger(\vec{r})\boldsymbol{\psi}_\uparrow^\dagger(\vec{r})\right\rangle \left\langle \boldsymbol{\psi}_\downarrow(\vec{r}\,')\boldsymbol{\psi}_\uparrow(\vec{r}\,')\right\rangle \end{aligned} \tag{2.16}$$

in the limit the pair separation $|\vec{r}-\vec{r}\,'|$ is infinite. Here, $\boldsymbol{\psi}_\uparrow^\dagger(\vec{r})$ and $\boldsymbol{\psi}_\uparrow(\vec{r})$ are the particle field operators [1] for creation and annihilation at a coordinate $\vec{r}$, with spin $\vec{k}\uparrow$ From the finite value of the pair correlation function ((2.16)), the local pair amplitude $\left\langle \boldsymbol{\psi}_\downarrow^\dagger(\vec{r})\boldsymbol{\psi}_\uparrow^\dagger(\vec{r})\right\rangle$ must be non-zero, which is, in essence the amplitude squared of the GL order parameter, $|\psi(\vec{r})|^2 \propto n_s$, the superfluid density. It's important to note that, although n_s is "local pair"

[1] $\psi_\uparrow(\vec{r}) = \left\langle \psi \,\middle|\, \boldsymbol{\psi}_\uparrow(\vec{r}) \,\middle|\, \psi \right\rangle$ is the real space representation, where $|\psi\rangle$ is the ground state wavefunction.

amplitude, pairings are non-local, ie, partners of a single pair are in macroscopic distance. With macroscopic ODLRO in effect, it's possible to derive Meissner effect [128, 130], flux quantization [128]. It has been argued that that ODLRO is a property not only of BCS superconductors but also of high-T_c superconductivity [130, 131] and of recently discovered superconductivity of Pnictide [132].

As in any appearance of order, superconducting order also reduces available symmetry of the system. In case of 2nd order, continuous, superconducting transition, order parameter is a measure of the amount of symmetry breaking in the ordered state. Symmetry group H describing the superconducting state must be a subgroup of the normal state symmetry group G:

$$G = X \times R \times U(1) \times T \quad \text{for } T > T_c \tag{2.17}$$

and

$$H \subset G \quad \text{for } T < T_c \tag{2.18}$$

where X is the symmetry group of the crystal lattice, R the symmetry group of spin rotation, $U(1)$ the one dimensional global gauge symmetry, and T the time reversal symmetry operation. Nearly all group-theoretic classifications of superconducting states are based on point-group symmetry. Point-group symmetry classification of pair states has been extensively studied in cuprate superconductors [133–135].

Order parameter symmetry can give insight into the mechanism/nature of pair condensate and limit the possible interactions that are possible. Crystal structures that have mirror symmetry (eg, CuO_2 layer based superconductors) can be described by parity of the the pair state. It has been argued that the complex phase diagram of high-T_c superconductors can be deduced from a symmetry principle that unifies antiferromagnetism and order parameter symmetry [136].

The superconducting energy gap $\Delta(\vec{k}, T)$ for s-wave superconductors, are believed to symmetric in momentum space (figure 2.5a). One other very important pairing symmetry is of d-wave where the energy gap is thought to be of the form

$$\begin{aligned} \Delta(\vec{k}_F, T) &= \Delta_0(\cos k_x - \cos k_y) \\ &\approxeq \frac{\Delta_0}{2}(k_x^2 - k_y^2), \text{ along the nodes, } k_x, k_y \text{ small} \end{aligned} \tag{2.19}$$

where momentum $\vec{k}_F$ is measured from the Fermi surface. It may be noted that for $|\hat{k}_x| = |\hat{k}_y|$, the gap is zero (figure 2.5b) meaning thermal excitations can easily destroy superconducting carriers. High-T_c superconductor family of YBCO are believed to be primarily of d-wave [137–139]. Establishment of predominantly d-wave order in T_c materials, over a wide range of doping and temperature range, entails the idea that d-wave symmetry is robust. This also suggests that d-wave pairing in cuprates has a common origin. Newly discovered

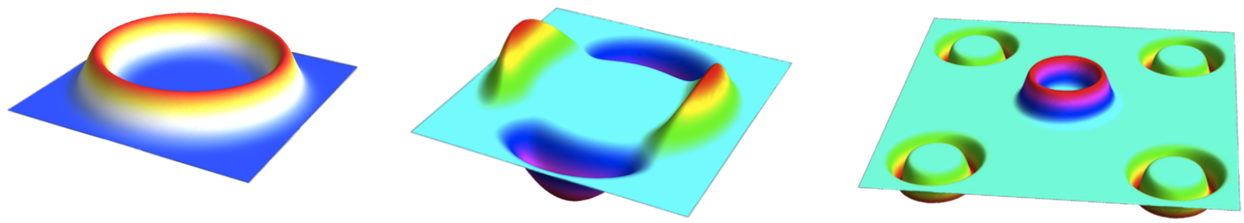

(a) **(b)** **(c)**

Figure 2.5: A schematic representation of the superconducting order parameter in different cases: (a) a conventional, s wave superconductor (eg. Nb); (b) a d wave, as is the case in copper oxides; (c) an $s_{\pm}$ wave, as is thought to be the case in iron-based superconductors. In (a) and (b), the two-dimensional Fermi surface is approximated by one circle. In (c), the Fermi surface is approximated by a small circle in the center (the first band) surrounded by four larger circles (to comply with the tetragonal symmetry [140]; the second band). In all cases, the height of the “rubber sheet” is proportional to the magnitude of the order parameter (including its sign).

family of FE-PNICTIDE superconductors are suggested to have $s_{\pm}$ (figure 2.5c) symmetry of order parameter from band structure calculations [81, 141]. Although a superconducting mechanism isn’t determined by the order parameter, the pairing hamiltonian must obey the point-group symmetry of the gap function $\Delta(\vec{k})$.

3

Experimental Techniques

3.1 Introduction To μSR

Muons were discovered in the 1930's and their properties learned in the 1940's and were used as probes of magnetism in matter [Rasetti, 1944]. μSR/MUSR refers to muon Spin Rotation/Relaxation/Resonance techniques which uses anisotropic decay of almost 100% spin-polarized muons to investigate local magnetic environment of matter, both in bulk and in thin films. This is significant improvement on other magnetic resonance probes such as nuclear magnetic resonance (NMR) and electron spin resonance (ESR) methods that must rely upon thermal equilibrium spin polarization in a magnetic field so that sufficient polarization is often achieved only at low temperatures and/or in strong magnetic fields.

When a muon(μ^+, solely used in our experiments) decays, it emits a fast decay positron preferentially along the direction of its spin due to the parity violation. From a single decay positron one cannot be certain which direction the muon spin is pointing in the sample. However, by measuring the anisotropic distribution of the decay positrons from a large number of muons deposited at the same conditions, the statistical average direction of the spin polarization of the muon ensemble can be determined. The time evolution of the muon spin polarization depends very sensitively on the spatial distribution and dynamical fluctuations of the muons' magnetic environment.

3.1.1 Properties And Production Of Muons

Muons are leptons, 207 times more massive than electrons. Muon properties are briefly mentioned in the following table 3.1. Muons are generated from the decay of charged pions ($\pi^\pm$), produced via collision of high-energy protons with target nuclei, such as carbon or beryllium. The charged pions that are produced live for only about 26 ns and then decay into a muon and muon neutrino (antineutrino), as schematically shown in figure 3.1;

$$\begin{aligned} \pi^+ &\rightarrow \mu^+ + \nu_\mu \\ \pi^- &\rightarrow \mu^- + \overline{\nu}_\mu \end{aligned} \tag{3.1}$$

Negative pions in targets behaves as heavy electrons and are captured by nucleus instead of decaying to negative muons. Positive pions do, however, are repelled by nuclei and take up interstitial positions in target atoms and subsequently decay into positive muon and

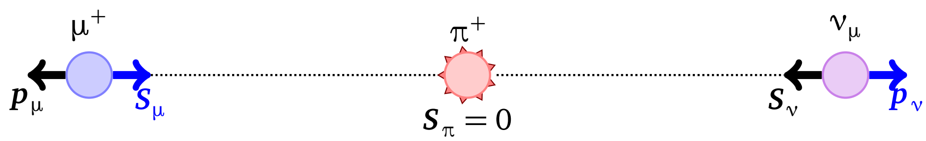

Figure 3.1: Positively charged pion live for about 26 ns and then decay into muon and a neutrino. The muons are almost 100% spin-polarized and their spins are opposite to their momentum. The muons carry a kinetic energy of 4.12 MeV in the rest frame of pion. These muons are referred to as "surface muons" as they originate from pions decaying near the surface of the production target.

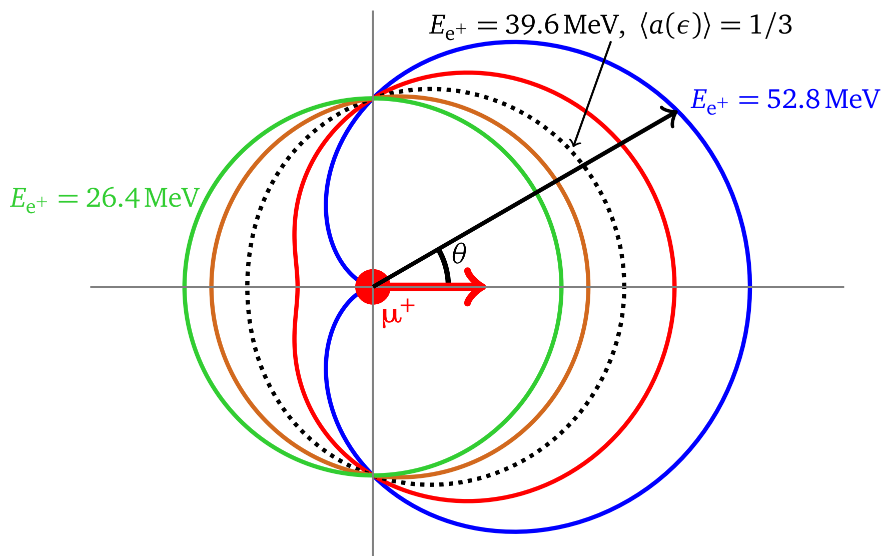

Figure 3.2: Angular probability distribution (K(ϵ, θ), between 26.4 MeV and 52.8 MeV) of positrons emitted from muons with polarization along the red arrow direction is shown. The maximum average asymmetry for such a β-decay process is 1/3 (the dotted curve).

a neutrino. For this reason, only positive muons are used to investigate local magnetic environments in materials. Because of the parity violating nature of weak beta-decay, the positron in a μ^+ decay is correlated with direction of muon spin at that instant. Ensemble average polarization may be determined from the decay asymmetry of emitted positrons. The highly relativistic positron's probability per unit time, in decaying at an angle θ with respect to the μ^+ spin polarization is given by

$$\frac{\mathrm{dW}(\epsilon,\theta)}{\mathrm{d}t} = \frac{e^{-t/\tau_\mu}}{\tau_\mu}\left[1 + \mathrm{a}(\epsilon)\cos(\theta)\right]\mathrm{n}(\epsilon)\,\mathrm{d}\epsilon\,\mathrm{d}(\cos(\theta)) \tag{3.2a}$$

$$\equiv \frac{e^{-t/\tau_\mu}}{\tau_\mu}\mathrm{K}(\epsilon,\theta)\,\mathrm{n}(\epsilon)\,\mathrm{d}\epsilon\,\mathrm{d}(\cos(\theta)) \tag{3.2b}$$

where "reduced energy" $\epsilon = E/E_{\max}$, the **asymmetry** $\mathrm{a}(\epsilon) = (2\epsilon - 1)/(3 - 2\epsilon)$, energy

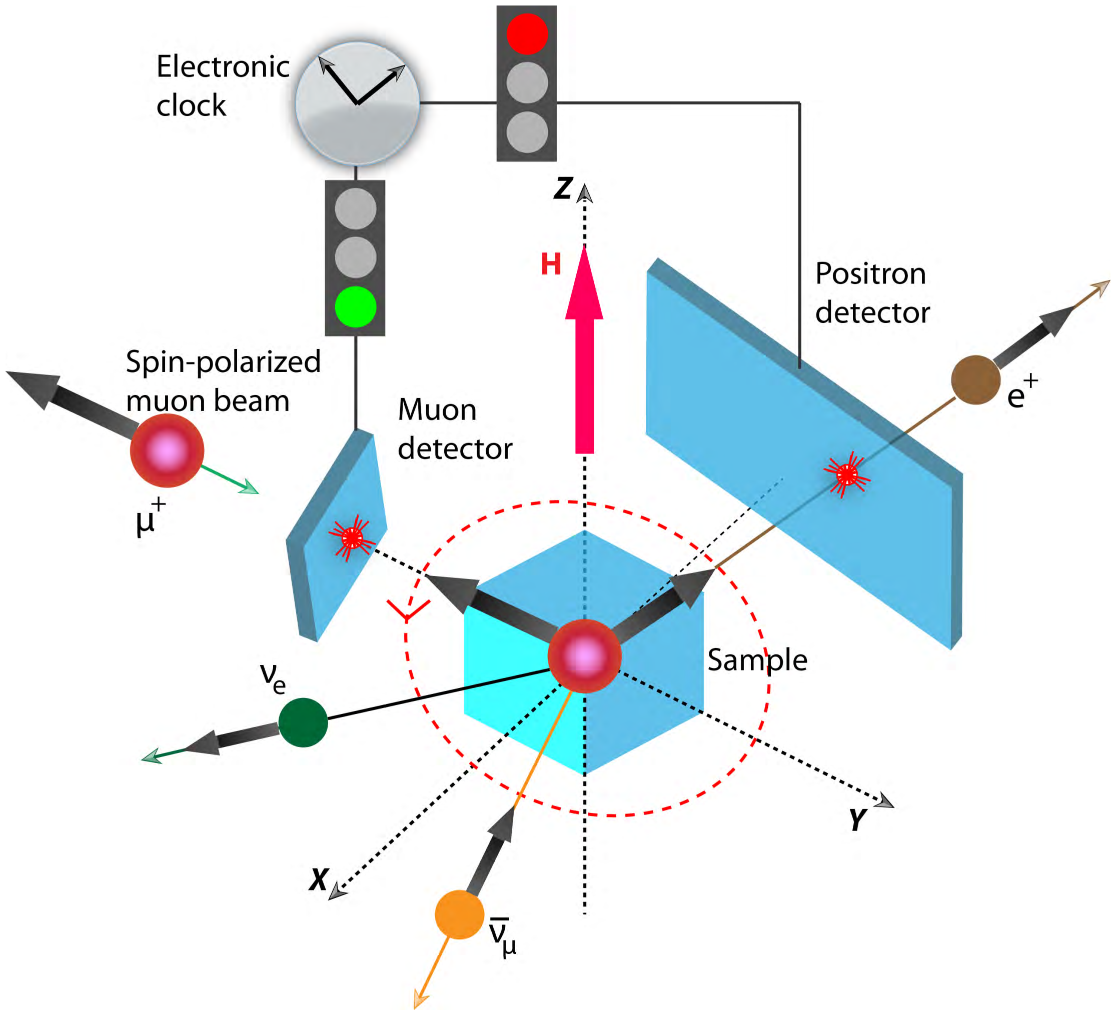

Figure 3.3: Schematic of the arrangement for a TF-μSR experiment. The muon spin Larmor precesses about the local magnetic field $\boldsymbol{B}$ at its stopping site in the sample, and subsequently undergoes the three-body decay $\mu^+ \rightarrow e^+ + \nu_e + \overline{\nu}_\mu$. The time evolution of the muon spin polarization is accurately determined by detection of the decay positrons from $\backsim 10^6$ muons implanted one at a time.

density function $n(\epsilon) = 2\epsilon^2(3-2\epsilon)$. The maximum positron energy $E_{max} \simeq 52.8\,\text{MeV}$, about half of the muon rest energy. Integrating over energy (ϵ), we get

$$dW(\theta) = \frac{e^{-t/\tau_\mu}}{\tau_\mu}\left[1 + \langle a(\epsilon)\rangle \cos(\theta)\right] d(\cos(\theta))dt \tag{3.3}$$

where, the average of the asymmetry function is

$$\langle a(\epsilon)\rangle = \int_0^1 a(\epsilon)\,n(\epsilon)\,d\epsilon = \frac{1}{3} \tag{3.4}$$

Table 3.1: Properties of Muon [144]

Mass, m_μ	105.658389(34) MeV/c^2
Lifetime, τ_μ	2.197034(21) μs
Charge, q	$\pm e$
Spin	$\frac{\hbar}{2}$
Magnetic moment	4.49044786(16)$\times10^{-26}$ J/T
Spin g-factor, g_μ	2.0023318414(12)
Gyromagnetic ratio, $\gamma_\mu = g_\mu \mu_\mu / h$	$2\pi \times 135.696\,82(5)\,\mathrm{MHz\,T^{-1}}$

The probability function $K(\epsilon, \theta)$ as a function of polar angle θ is plotted in figure 3.2 for reduced energy values of ϵ =0.5, 0.625, 0.75, 0.875 and 1.0. For an ensemble of muons, the maximum theoretical β-decay asymmetry is therefore 1/3. The asymmetry is determined in our experiments in a **transverse field (TF-μSR)** arrangement as shown in figure 3.3. **TF-μSR** refers to the case of incoming muon polarization being perpendicular to the external field direction For more details of muon production the reader is referred to these references [142, 143].

3.1.2 General μSR Techniques

Detailed accounts of techniques may be found in the following references: the book of Schenck [145], the review article of Cox [146] & of H. Keller [147]. For general technical and statistical details, readers may consult these theses: Riseman [142], Chow [148] and Luke [149]. While conventional surface muon beams can be used to investigate rather small samples, there is a desire for still lower energy muons that can be stopped near sample surfaces (for example to determine depth dependent magnetic field), in thin films and near multi-layer interfaces (to determine exotic magentic phenomenon). A number of innovative methods have been used in attempts to produce **ultra slow** muon beams. The results in this thesis were obtained using one such method employing ultra slow muons as probe, described in the next section.

3.2 Low Energy μSR

The experiments detailed in this thesis were done in the low energy ($\leq$ 30 keV) **LEM**-μSR beamline (μE4 [150]) in Paul Scherrer Instituit (PSI). LEM group has developed a technique of slowing down a surface muon beam of 4 MeV and 100% polarization to a beam of low energy (0-30 keV), polarized muons. Figure 3.4 shows the schematic low energy beamline μE4. The 4 MeV beam passes through a **moderator** consisting of a thin layer (∽100 nm) of rare gas solid or solid nitrogen deposited on 125 μm silver substrate. A very small fraction of the muons escape the moderator with a mean energy about 15 eV with an energy spread (FWHM) of ∽20 eV. The dominant fraction of the beam exits the moderator target as **fast** (degraded but not moderated) muons with a mean energy of 500 keV and a FWHM of the same order. These fast muons are separated from the slow ones by a 90 degree deflection by an electrostatic mirror. This deflection, of slow muons, necessarily changes momentum direction of muons while keeping the spin direction unaltered. After deflection, muon spin and momentum directions are perpendicular. Fast muons are little affected by the electrostatic mirror and are monitored by multi channel plate[MCP] detector. The **low energy muons** are clearly identified by a time-of-flight (TOF) measurement between the start scintillator and the **trigger detector**. The trigger detector, made of an ultra-thin carbon foil ($2.2\,\mu\mathrm{g\,cm^{-2}}$), is used to set **time-zero,** t_0 for the incoming low energy muons. The muons traversing the foil emit a few electrons, which are deflected by 90 degrees and detected by a MCP to give the start signal for the μSR measurement. Trigger detector causes an energy loss of the muons $\sim 1.6\,\mathrm{keV}$ with a Gaussian energy spread $\sim 500\,\mathrm{eV}$. Detection efficiency of trigger detector is $\sim 80\%$. After passing trigger detector, the μ^+ beam is focused on the sample by an einzel lens (L3) and a conically shaped electrostatic lens.

The sample and it's Ni-coated[1] Al holder are electrically insulated by a thick sapphire crystal and can be biased -12.5 keV to +12.5 keV. Sapphire crystal also provides a good thermal contact between the cold finger and the sample. The bias voltage, coupled with the voltage at trigger detector (between 12 and 20 kV), determines the muon energy at the sample ranging from 0.5 keV to 30 keV. A Helmholtz coil is used to generate external magnetic field applied to the muons. External magnetic field(B_{ext}) can be applied in two directions; either parallel to muon momentum direction or perpendicular to it, i.e, parallel to sample plane (ab). In the first case, muons precess in the sample plane and four scintillator telescopes (Left, Right, Top and Bottom) are used to count emitted positrons. In the other case, muon spins precess out of the plane and only left and right positron counters record positron decays. The experiments detailed in this thesis uses the second scenario where B_{ext} is parallel to sample plane. Extensive details on low energy muon beamline may be found elsewhere [151, 152].

3.2.1 Principles Of LE-μSR

Positron detectors help accumulating histograms of positron detection events having the mathematical form

$$N(t) = N_{\mathrm{bg}} + N_0 e^{-t/\tau_\mu}(1 + \mathcal{A}(t)), \tag{3.5}$$

where N_0 is the normalization, N_{bg} is a time-independent background and $\mathcal{A}(t)$ is the time dependent asymmetry for the detector along $\hat{\boldsymbol{n}}$ direction, defined as

$$\mathcal{A}(t) = A_0 \mathcal{P}(t) = A_0 \hat{\boldsymbol{n}} \cdot \boldsymbol{\mathcal{P}}(t) \tag{3.6}$$

[1]The sample holder is coated with $\sim 1\,\mu\mathrm{m}$ of Ni. Since Ni is ferromagnetic, muons that miss the sample, experience a big hyperfine field and disappears from the frequency window of interest. This very effective background suppression method was the critical step which allows low energy μSR to be applied to crystals much smaller than the beam diameter.

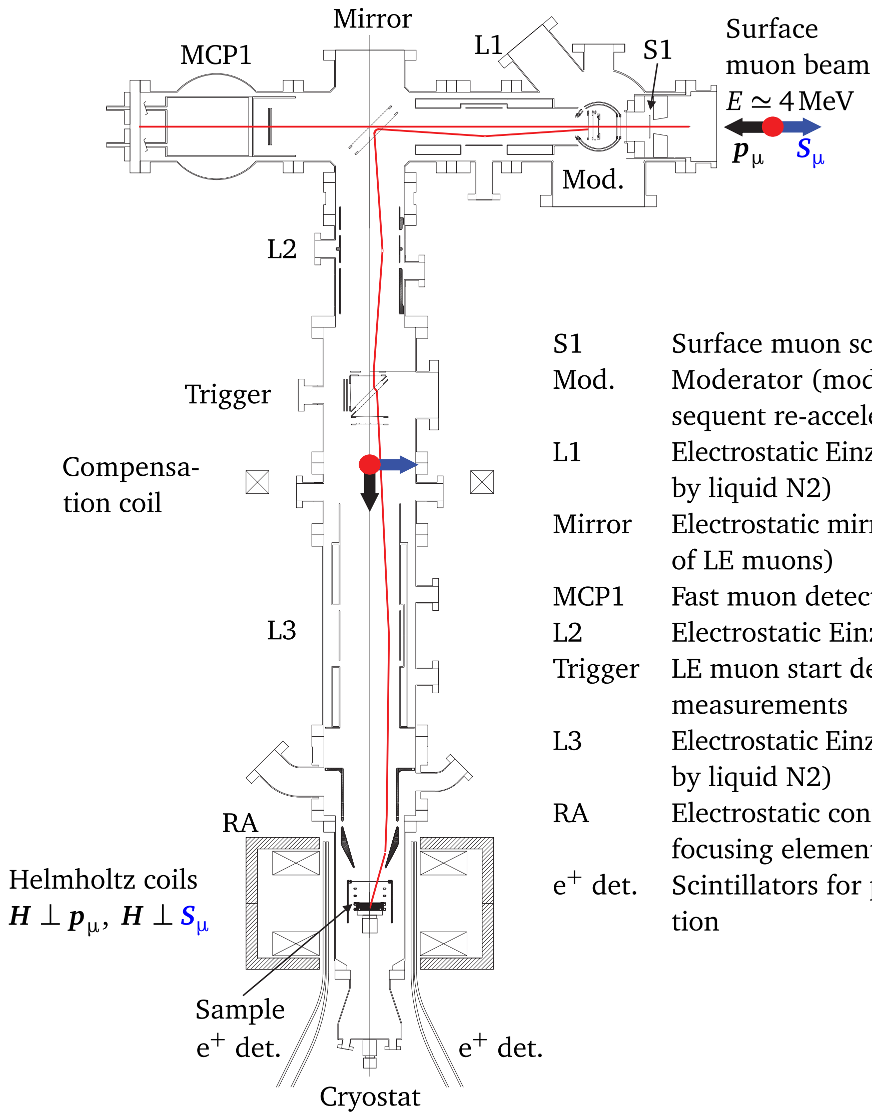

S1	Surface muon scintillator
Mod.	Moderator (moderation & subsequent re-acceleration)
L1	Electrostatic Einzel lens (cooled by liquid N2)
Mirror	Electrostatic mirror (separation of LE muons)
MCP1	Fast muon detector
L2	Electrostatic Einzel lens
Trigger	LE muon start detector for μSR measurements
L3	Electrostatic Einzel lens (cooled by liquid N2)
RA	Electrostatic conical lens (main focusing element)
e^+ det.	Scintillators for positron detection

Figure 3.4: Adapted from [151]: A fraction of incoming muons yields very slow muons with a mean energy of about 15 eV. They are accelerated to energies up to 20 keV. The transverse magnetic field with respect to the muon spin is applied by use of a pair of Helmholtz coils. The positrons from the muons decaying in the sample are detected by four pairs of scintillators surrounding the vacuum tube.

where A_0 is directly related to the theoretical maximum **asymmetry** $a(\epsilon)$ referred in (3.4) Muon polarization $\boldsymbol{\mathcal{P}}(t)$ reflects time-dependent spin-polarization and its modulus defined as

$$\mathcal{P}(t) = \frac{\langle \boldsymbol{S}(t) \cdot \boldsymbol{S}(0) \rangle}{\langle S(0)^2 \rangle} \tag{3.7}$$

where $\boldsymbol{\mathcal{P}}(0) = \pm \hat{\boldsymbol{n}}$. $\hat{\boldsymbol{n}}$ refers to the direction of observation (detector). Experimentally observed asymmetry is lower than the maximum value of $1/3$ as the initial spin polarization is less than 1 and emitted positrons are collected in a limited solid angle. Nevertheless, muon asymmetry (polarization) contains all information about muons interaction with the local magnetic environment. Upon entering the sample, the muon spins interact with local magnetic environment and ensemble average spin changes according to the Bloch equation,

$$\frac{\mathrm{d}\boldsymbol{S}}{dt} = \boldsymbol{\mu} \times \boldsymbol{B} \tag{3.8}$$

where, $\boldsymbol{B} = \boldsymbol{B}_{\text{ext}} + \boldsymbol{B}_{\text{int}}$. $\boldsymbol{B}_{\text{ext}} >> \boldsymbol{B}_{\text{int}}$, for the experiments detailed in this thesis. Without loss of generality, static external magnetic field may be assumed as $\boldsymbol{B}_{\text{ext}} = B\hat{z}$, yielding

$$\frac{\mathrm{d}S_x}{\mathrm{d}t} = \gamma S_y B \tag{3.9a}$$

$$\frac{\mathrm{d}S_y}{\mathrm{d}t} = \gamma S_x B \tag{3.9b}$$

$$\frac{\mathrm{d}S_z}{\mathrm{d}t} = 0 \tag{3.9c}$$

The above equations (3.9a) and (3.9b) are solved by

$$\begin{aligned} S_x(t) &= S(0)\sin(\gamma B t + \varphi) \\ S_y(t) &= S(0)\cos(\gamma B t + \varphi) \end{aligned} \tag{3.10}$$

where $S(0)$ and φ are determined by spin direction at $t = 0$.

So far, a big external field's effect (precession of polarization) has been discussed. Here we discuss the effects of (small) internal fields that are present in any sample due to randomly oriented magnetic moments.

$$\mathcal{P}(t) = \iiint P(\boldsymbol{B}) \mathcal{P}_B(t) \mathrm{d}\boldsymbol{B} \tag{3.11}$$

where $\boldsymbol{B}$ is the local magnetic field muon experiences, $B = |\boldsymbol{B}|$, $P_B(t)$ is the time-dependent (oscillating) muon polarization and $P(B)$ is the normalized probability distribution of magnetic field inside the sample. Inside the sample, randomly oriented magnetic moments can generate a distribution of magnetic field, at any given muon site, and may be approximated by a three-dimensional Gaussian distribution,

$$P(\boldsymbol{B}) = \left(\frac{\gamma_\mu}{\sqrt{2\pi}\sigma}\right)^3 \exp\left(-\frac{\gamma_\mu^2 B^2}{2\sigma^2}\right) \tag{3.12}$$

For an external field perpendicular to muon spin direction, e.g. $\boldsymbol{B}_{\text{ext}} = B_{\text{ext}}\hat{\mathbf{x}}$, the Gaussian probability distribution (3.12) is centered around field $\boldsymbol{B} = (B_{\text{ext}}, 0, 0)$, and has the form

$$P(\boldsymbol{B}) = \left(\frac{\gamma_\mu}{\sqrt{2\pi}\sigma}\right)^3 \exp\left(-\frac{\gamma_\mu^2\left((B_x - B_{\text{ext}})^2 + B_y^2 + B_z^2\right)}{2\sigma^2}\right) \tag{3.13}$$

With $\mathcal{P}(0) \parallel \hat{\mathbf{z}}$, the muon polarization may be written as,

$$\begin{aligned}
\mathcal{P}(t) &= \left(\frac{\gamma_\mu}{\sqrt{2\pi}\sigma}\right)^3 \int\int\int \exp\left(-\frac{\gamma_\mu^2\left((B_x - B_{\text{ext}})^2 + B_y^2 + B_z^2\right)}{2\sigma^2}\right) \cos(\gamma_\mu B t)\mathrm{d}\boldsymbol{B} \\
&\simeq \frac{\gamma_\mu}{\sqrt{2\pi}\sigma} \int_{B_x=-\infty}^{\infty} \exp\left(-\frac{\gamma_\mu^2\left(B_x - B_{\text{ext}}\right)^2}{2\sigma^2}\right) \cos(\gamma_\mu B_x t)\mathrm{d}B_x \\
&= \left(\frac{\gamma_\mu}{\sqrt{2\pi}\sigma}\right)\left(\frac{\sqrt{2}\sigma}{\gamma_\mu}\right) \int_{n=-\infty}^{\infty} \exp\left(-n^2\right) \cos\left(\gamma_\mu\left(\frac{\sqrt{2}\sigma n}{\gamma_\mu} + B_{\text{ext}}\right)t\right) \mathrm{d}n \\
&= \left(\frac{1}{\sqrt{\pi}}\right) \int_{n=-\infty}^{\infty} \exp\left(-n^2\right) \cos\left(\sqrt{2}\sigma t n + \gamma_\mu B_{\text{ext}} t\right) \mathrm{d}n \\
&= \exp\left(-\frac{\sigma^2 t^2}{2}\right) \cos\left(\gamma_\mu B_{\text{ext}} t\right)
\end{aligned} \tag{3.14}$$

As may be seen from (3.14), random moments in a sample give rise to damping in the muon polarization. Additionally, when muons are implanted into a sample with inequivalent magnetic sites (e.g. superconducting state), there will be a distribution ($\rho(B)$), discussed in detail in the following section, of fields $\left(B(z) \equiv B_{\text{ext}}(z)\right)$ inside the sample & the polarization (3.14) takes the form

$$\mathcal{P}(t) = \exp\left(-\frac{\sigma^2 t^2}{2}\right) \int_0^\infty \rho(z) \cos\left(\gamma_\mu B(z) t\right) \mathrm{d}z \tag{3.15}$$

The asymmetry $\mathcal{A}(t) = A_0 \mathcal{P}(t)$ is fitted to the experimentally observed asymmetries to obtain physical parameters A_0, σ and d, λ (in Meissner state).

An example histogram of raw data, from the **forward** counter and asymmetry $\mathcal{A}(t)$ are given in figure 3.5. In this experiment, a transverse external field of 9.47 mT was applied and the resulting sinusoidal oscillations can be taken into account by the theoretical model in

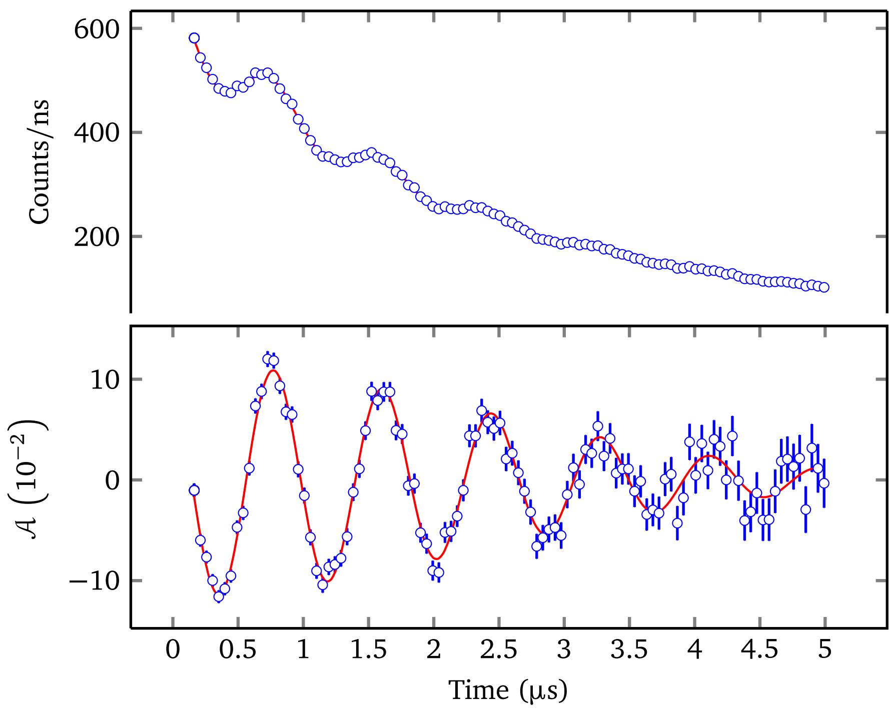

Figure 3.5: Top: A histogram from "forward" positron detector in a time-differential measurement on the sample of $YBa_2Cu_3O_{6.92}$, depicting the exponential decay of the muons and muon precession. Bottom: Larmor precession of muons' spin magnetic moment may be noticed from the time dependence of asymmetry $\mathcal{A}(t)$, in an external applied field of 94.7G with an implantation energy of 22 KeV, with temperature of 90K.

(3.15). Probably the most important characteristic of the muon polarization decay spectrum is the precession frequency which represents average magnetic field, including local magnetic fluctuations, muons experience.

3.2.2 Stopping Distribution

Even at a specific energy, ions bombarded onto a material, end up at different depths due to randomness in the collision process. The energy dependent stopping profiles can be generated using "Transport of Ions in Solids" (TRIM) codes introduced by Ziegler *et al* [153] based on the ideas of Eckstein [154]. The accuracy of TRIM in calculating ion range distributions in various materials is well established, and they are routinely used in similar depth controlled experiments such as Low-Energy μSR. By specifying the energy, charge, and mass of the probe ions (μ^+ in this thesis), and the mass density and atomic numbers of the elements of the probed material, one is able to simulate the implantation profile using TRIM. Generated energy-dependent profiles of YBCO are shown in figure 3.6. Average depth of muons increases with energy and an almost linear relationship ($\langle z_\mu \rangle (E) = 3.26 + 4.37 * E$ nm) is obtained as shown in figure 3.6. For $Ba(Co_{0.074}Fe_{0.926})_2As_2$, a different energy dependent linear relationship ($\langle z_{\mu} \rangle (E) = 4.26 + 4.53 * E$ nm) is obtained. The stopping profiles are only relevant for the μ^+ ions stopping in the probed material. A majority fraction of incoming μ^+ ions stop at Ni coated sample plate where it quickly depolarizes and do not affect the calculation of penetration depth presented in this thesis. A review of depth resolved studies of materials may be found in [152, 155] and references therein.

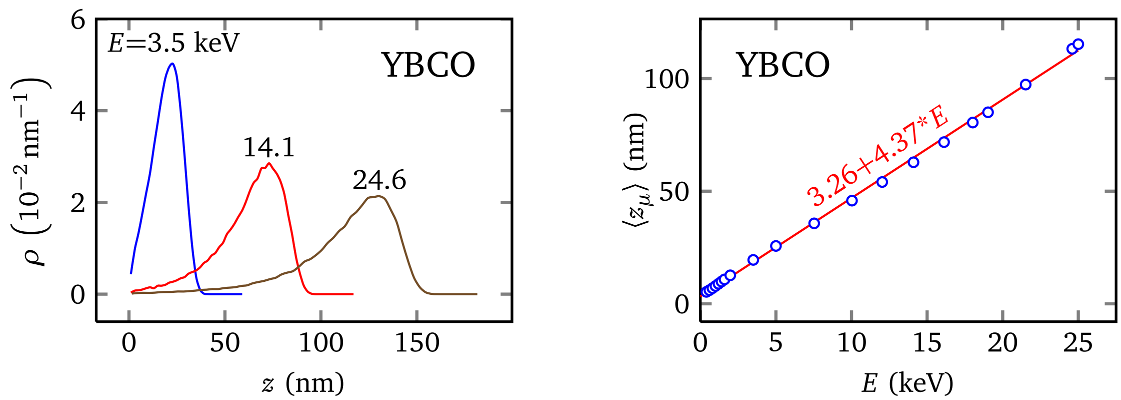

(a) (b)

Figure 3.6: Muon implantion profiles in YBCO: Implanted muons stop at differ depths even if the incoming beam energy is the same. By specifying the energy, charge, and mass of the μ^+ ions, and the mass density and atomic numbers of the elements, profiles are simulated via Monte-Carlo algorithm using TRIM.SP. The accuracy of TRIM.SP in calculating ion range distributions in various materials is well established, and they are routinely used in similar depth controlled experiments.

4

Results and Analysis

In this chapter, measurements of λ and the anisotropies$\left(\equiv \lambda_a/\lambda_b\right)$ are presented for three different oxygen ($x = 6.52, 6.92, 6.998$) contents of $YBa_2Cu_3O_{6+x}$ and for $Ba(Co_{0.07}Fe_{0.93})_2As_2$. The measured values of λ and the anisotropies are considerably different from that of literature, often found with indirect methods.

External magnetic field drops inside a superconductor according to London model, described in section 2.2, on the length scale of λ. Close to the surface, there may be deviations from a purely exponential $B(z)$ as conjectured in (2.15). A reduction in magnetic field can be detected using LE-μSR as muon precession frequency is proportional to the local magnetic field. An schematic representation of the fitting procudure to obtain λ and other parameters are shown in figure 4.1. In the normal state, external field ($\mu_0 H$) penetrates the sample fully yielding an average muon precession frequency of $\left(\gamma_\mu \mu_0 H\right)/2\pi$. A distribution of the local fields, from randomly oriented nuclear moments (see (3.14)), is approximated by the broadening parameter σ. In the superconducting state, muon precession frequency depends on implantation depth (z), for the muons landing between depth z and $z + \mathrm{d}z$ and the time dependent asymmetry may be written as

$$\mathcal{A}(t) = A_0 \exp\left[-\sigma^2 t^2/2\right] \times \int \rho(z) \cos\left[\gamma_\mu B(z, d, \lambda)t + \varphi\right] dz \tag{4.1}$$

A slightly modified form (4.2) of the above equation (4.1) is used to fit **all** superconducting states and to extract parameters $A_\circ, d, \sigma, \lambda, \varphi$. Average magnetic field $\langle B \rangle$ are computed from the above mentioned parameters for various externally applied magnetic fields ranging from 1.5 mT to 10 mT. All measurements in the superconducting state were carried out under **zero-field-cooled** conditions in order to avoid flux trapping at the surface.

The analysis in this chapter are presented chronologically:

(i) $YBa_2Cu_3O_{6.92}$ i.e YBCO-I, section 4.1.1.

(ii) $YBa_2Cu_3O_{6.998}$ i.e YBCO-II, section 4.1.2

(iii) $YBa_2Cu_3O_{6.52}$ i.e YBCO-III, section 4.1.3

(iv) $Ba(Co_{0.07}Fe_{0.93})_2As_2$, section 4.2

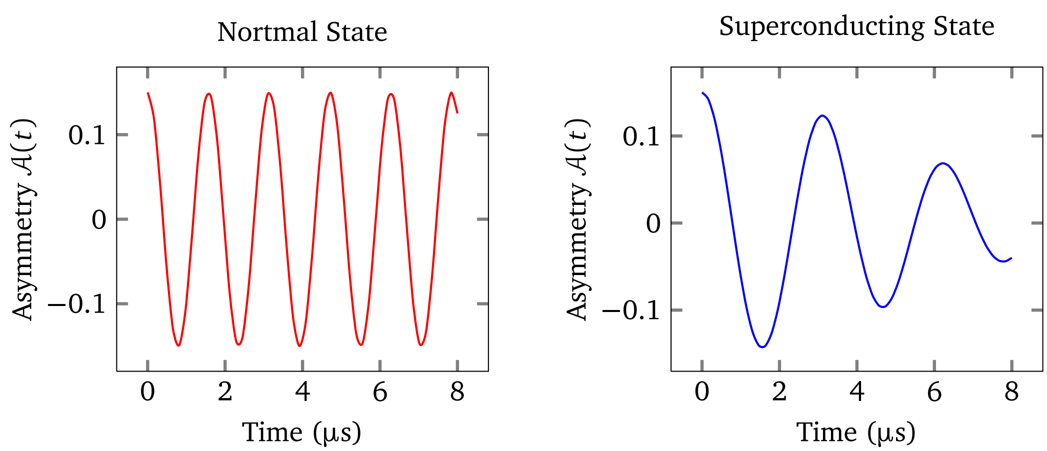

Fit to:
$A_0 \exp\left[-\sigma^2 t^2/2\right] \cos(\gamma_\mu B_0 + \varphi_0)$

Fit to: $A_0 \exp\left[-\sigma^2 t^2/2\right] \times$
$\int \rho(z) \cos\left[\gamma_\mu B(z, d, \lambda) t + \varphi\right] dz$

Figure 4.1: Quick outline of the fitting procedure: Left: In the normal state, oscillatory signal in muon polariztion is fitted to a cosine function with a Gaussian broadening originating from randomly oriented local internal fields. Right: In the superconducting state, polarization is a sum of frequency ($\gamma_\mu B$) dependent oscillation and an additional broadening σ taking into account expelled flux from neighboring crystals or from any other sources of random fields.

4.1 LE-μSR experiments on $YBa_2Cu_3O_{6+x}$ single crystals

The LE-μSR experiments on $YBa_2Cu_3O_{6+x}$ have been conducted on freshly grown single crystals using the self-flux method [156]. The purity of the crystals is the same as for crystals in which quantum oscillations in resistivity have recently been reported [157]. Each of the crystals was approximately rectangular in shape with lateral dimensions in the a-b plane ranging from 1 mm to 3 mm and a thickness in the c-direction ranging from 0.1 mm to 0.3 mm. They were detwinned to a level greater than 95 %. The mounted mosaic of YBCO-II on the coldfinger is shown in the figure 4.2. Two other oxygen doped crystals were mounted in very similar method. The crystal faces were mirror-like in appearance and atomic force microscopy indicates the roughness of the surface to be a few nm (cf. figure 4.3). A UHV compatible Ag epoxy was used to attach each crystal to the sample holder made of high purity Al coated with 1 μm of Ni. Muons that miss the sample stop at the polycrystalline Ni coated sample holder and experience big hyperfine field from Ni moments; thereby quickly depolarizes and disappears from the frequency window of interest. Control experiments on a Ag disc the same size as the sample showed that such a thin layer of Ni has no effect on the precession signal in the sample. The maximum asymmetry A_0 from all these experiments are significantly less than the theoretical maximum 1/3 as decay positrons are collected in a limited solid angle and only $\sim 40\,\%$ muons land on $YBa_2Cu_3O_{6+x}$ crystals.

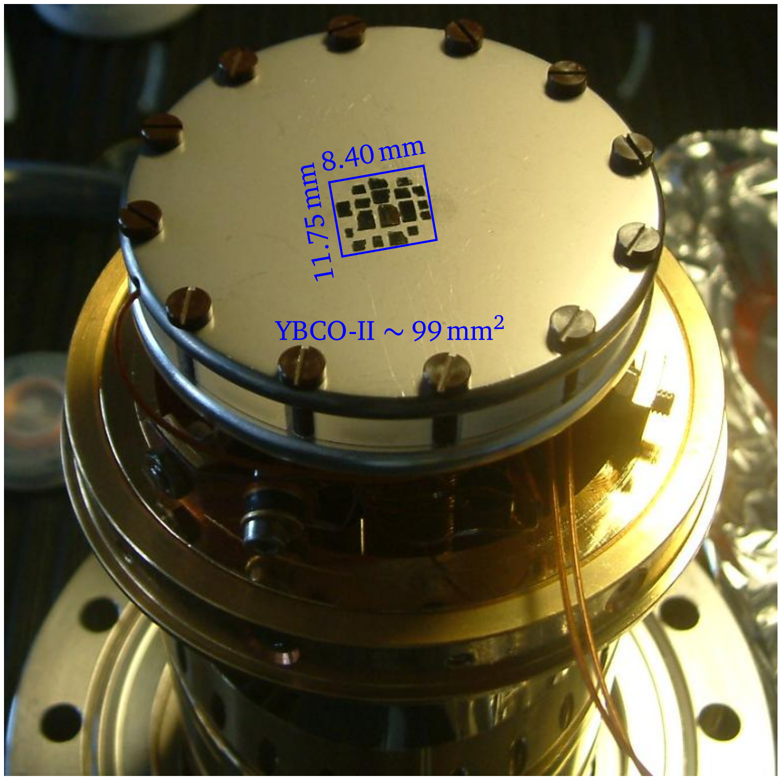

Figure 4.2: YBCO-II Mosaic: The total area of the mosaic is about 99 mm^2. Each of the crystals was approximately 1 mm to 3 mm in the $a-b$ plane and a c-axis thickness of 0.1 mm to 0.3 mm. An ultra high vacuum compatible Ag epoxy was used to attach each crystal to the sample holder of high purity Al coated with 1 µm of Ni.

4.1.1 $YBa_2Cu_3O_{6.92}$

To analyze superconducting state asymmetry $\mathcal{A}(t)$, slightly modified version of (4.1) is used

$$\mathcal{A}(t) = A_0 \exp\left(-\frac{\sigma^2 t^2}{2}\right) \int \rho(B) \cos\left[\gamma_\mu B(z,d,\lambda)t + \varphi\right] \mathrm{d}B, \tag{4.2}$$

where an integration over field distribution $\rho(B)$ is done instead of an integral over $\rho(z)$. $\rho(B)$ is defined as

$$\rho(B) = \rho(z)\left|\frac{dB}{dz}\right|^{-1} \tag{4.3}$$

Although equations (4.1) and (4.2) are mathematically equivalent for the analysis presented in this thesis, the latter offers a more general approach for analyzing data using models where a specific field distribution is believed to be present. To take into account any random

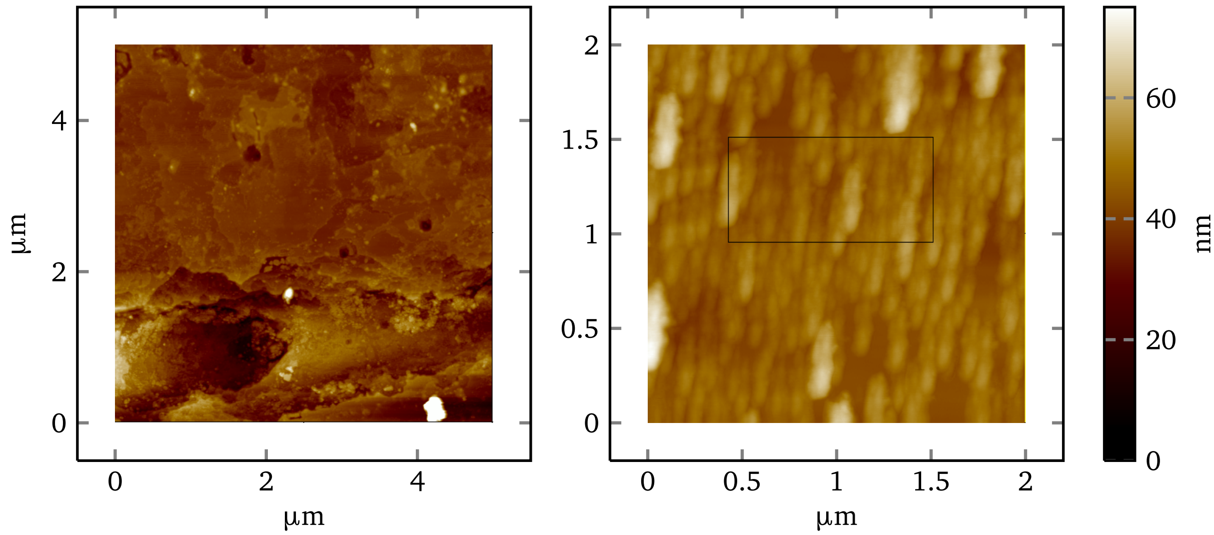

Figure 4.3: YBCO roughness: Left figure shows a 5 µm×5 µm area of a YBCO-I crystal being scanned by tapping AFM. Right figure shows another region of a smaller size and even smaller sized box. A 2 nm to 3 nm of average roughness is found from these measurements.

local field present at a muon site, a Gaussian probability model is assumed as,

$$P\left(B',B\right) = \left(\frac{1}{\sqrt{2\pi}\Delta B}\right) \exp\left(-\frac{1}{2}\left(\frac{B'-B}{\Delta B}\right)^2\right) \tag{4.4}$$

where $P\left(B',B\right)$ is the probability function of the total field B' experienced by muon and ΔB is the width of the proability function. Broadened total probability density is obtained by convoluting (4.4) with the field distribution from the pure London model in the (4.3)

$$\rho'\left(B'\right) \equiv \int_{B=0}^{\infty} P\left(B',B\right) \rho(B)\,\mathrm{d}B \tag{4.5}$$

Since stopping distributions ($\rho(z)$) are obtained as discrete numbers from TRIM.SP simulations, the integral in the (4.5) is replaced by a summation to calculate the total probability density. As may be seen from the figure 4.4a, the field distributions from maximum-entropy (ME) [158–160] are wider than that expected from a pure London model ($\sigma = 0$). For the ME analysis a Gaussian apodization ($\sigma_{\text{apod}} = 2.0\,\mu\text{s}$) is used for all the energy dependent spectra. Apodoziation leads to very small symmetric broadening and smoothing of field distribution but is not expected to change the average magnetic field $\langle B \rangle$. This may be noted that there is considerable weight at higher fields (cf. figure 4.4b) than the applied field $\mu_0 H$ which is out of the scope of the (4.3).

In the equations (4.1) and (4.2), φ should ideally depend on purely geometric parameters

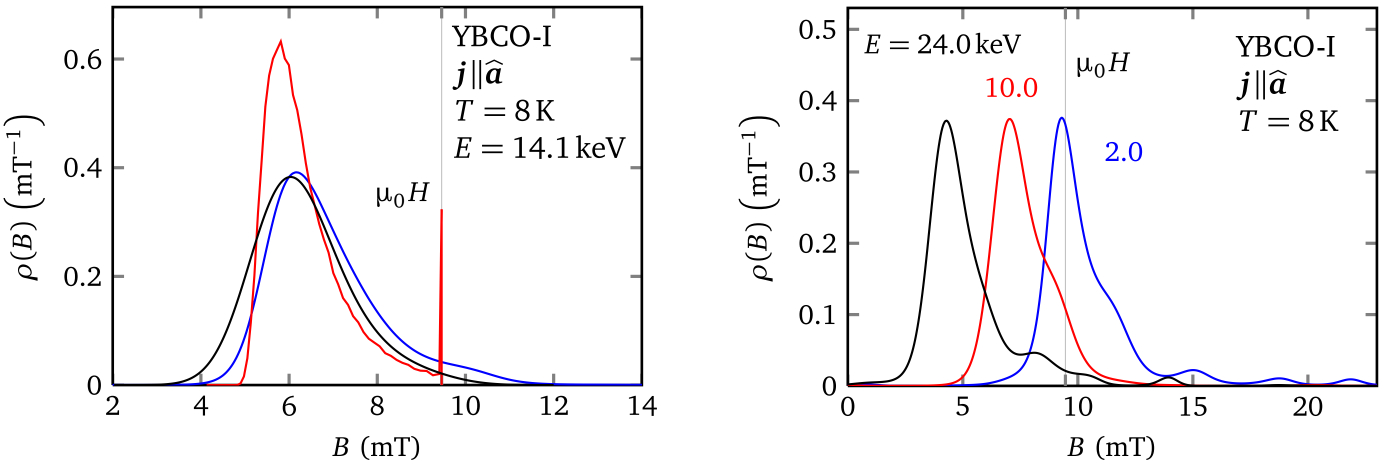

(a) **(b)**

Figure 4.4: (a) Magnetic field distribution as seen by muons at an implantation energy of $E = 14.1\,\mathrm{keV}$ and at $T = 8\,\mathrm{K}$ in an external magnetic field $\mu_0 H = 9.5\,\mathrm{mT}$, applied parallel to the b axis of the crystals. The field distribution corresponds to the asymmetry spectrum (△) in the figure 4.5. The red line (——) is model field from pure London model with $d = 10.3\,\mathrm{nm}$, $\lambda_a = 128.9\,\mathrm{nm}$ and $\sigma = 0$. The spike in $\rho(B)$ at the applied field is from muons stopping in dead layer. The black line (——) is the theoretical distribution convoluted with a Gaussian with a second central moment $\Delta B = 0.72\,\mathrm{mT}$ corresponding to the average $\sigma = 0.61\,\mu\mathrm{s}^{-1}$ from the figure 4.6b). The blue line (——) is obtained from maximum-entropy analysis. The higher weight at high fields in actual field distribution is likely to be from trapped vortices close to the surface and is not taken fully into account by our symmetrically braodened field distribution. (b) Maximum-entropy field distribution are shown at three different energies. At the lowest energy, there is significant contribution from possible demagnetization and trapped vortices.

and muon arrival time on the sample. Thereby, one way to analyze the spectra is to fix φ to values obtained at temperatures above T_c, as has been described in [161]. However, φ may be substantially different in the superconducting state compared to the values for $T > T_c$, as we will see shortly. φ may also depend on muon implantation energy in the following manner[1]: in the normal state ($T > T_c$) the angular part of the asymmetry is given by

$$\mathcal{A}(t) \sim \cos\left(\omega(t - t_0)\right) \tag{4.6}$$

assuming $\varphi = 0$, for simplicity. Here $\omega = \gamma_\mu B$ is the frequency and t_0 being the time muon enters the sample. If an error is made in determining $t_0 \to t_0 - dt$, then (4.6) becomes

$$\mathcal{A}(t) \sim \cos\left(\omega(t - t_0) + \omega dt\right) \tag{4.7}$$

[1]This analysis was inspired by Rob Kiefl

Equation (4.7) implies that the fitted phase will be ωdt However, in superconducting state and in high implantation energy, muons deep inside the sample will see a reduced field and a corresponding reduced frequency $\omega'_E < \omega$, assuming for simplicity that all the muons precess in a single frequency. This implies that, in superconducting state, (4.7) may be written as

$$\mathcal{A}(t) \sim \cos\left(\omega'_E(t - t_0) + \omega'_E dt\right) \tag{4.8}$$

meaning a phase shift of $(\omega'_E - \omega)dt$ will be detected. The possiblity of actual frequency distribution being more asymmetric than our theoretical frequency distribution one can also introduce an apparent phase shift. To summarize, imperfections in fitting function, TOF distribution and detector geometry may all introduce energy dependent phase shift. For the reasons above, phases for individual energies were kept free (**individual phase model**) in the global fit. A shared phase global fit analysis (**shared phase model**) was also done which yields $\lambda_{\{a,b\}}$ values within the systematic errors$\sim$ 3nm. This is also a strong indication that the subtlelities of muon arrival time, detector geometry and thereby the phases (φ) & broadening parameter (σ) do not significantly influence the extraction of the absolute values of London penetration depth.

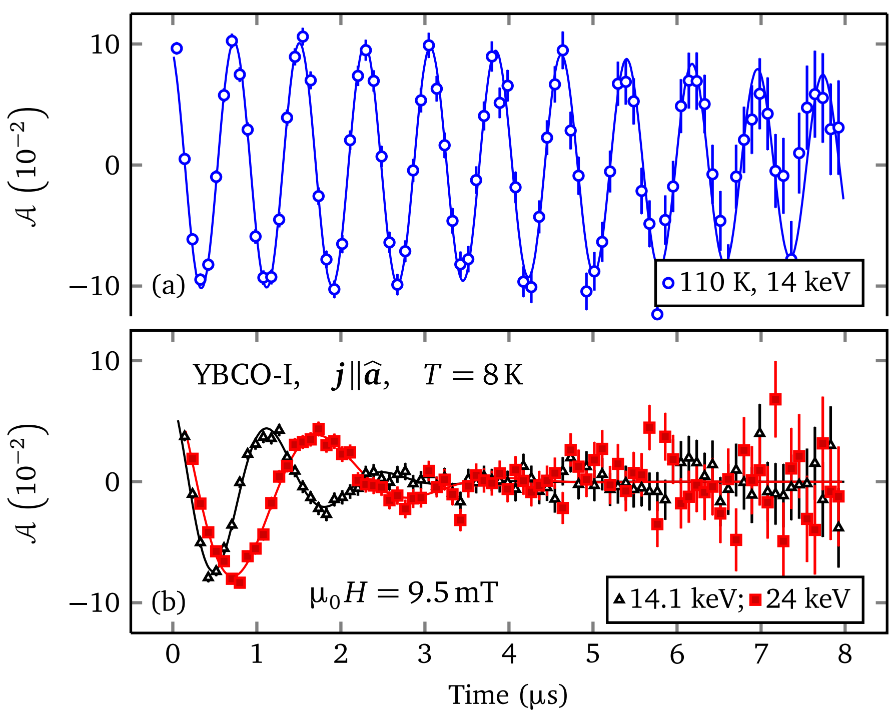

Figure 4.5: Top: The muon spin precession signal in the normal state of $YBa_2Cu_3O_{6.92}$ at 110 K in an external field of 9.46 mT applied parallel to the b direction. The mean implantation energy is $E = 14.1$ keV which corresponds to a mean implantation depth of 65 nm. Bottom: the same conditions as top except in the superconducting state at $T = 8$ K for two energies 14.1 keV and 24 keV.

Figure 4.5a shows the muon precession signal in the normal state at 110 K in a small magnetic field of 9.5 mT applied along the a axis of the crystals with an implantation energy at 14.1 keV. Observed frequency in figure 4.5a also includes a damping rate of 0.086(11) μs^{-1} which is consistent with the damping from randomly oriented Cu nuclear dipole moments. Meissner screening of the external field is apparent by comparing the normal state (figure 4.5a) with the superconducting state (figure 4.5b). As mentioned earlier, the superconducting state data are fitted to (4.2) with shared A_0, d and λ for all the spectra at 8 K in both a and b directions. The depth dependence of the average internal field is evident by comparing the two spectra (▵ and ■) in figure 4.5b which have different implantation profiles. Examplary profiles are shown in figure 3.6a.

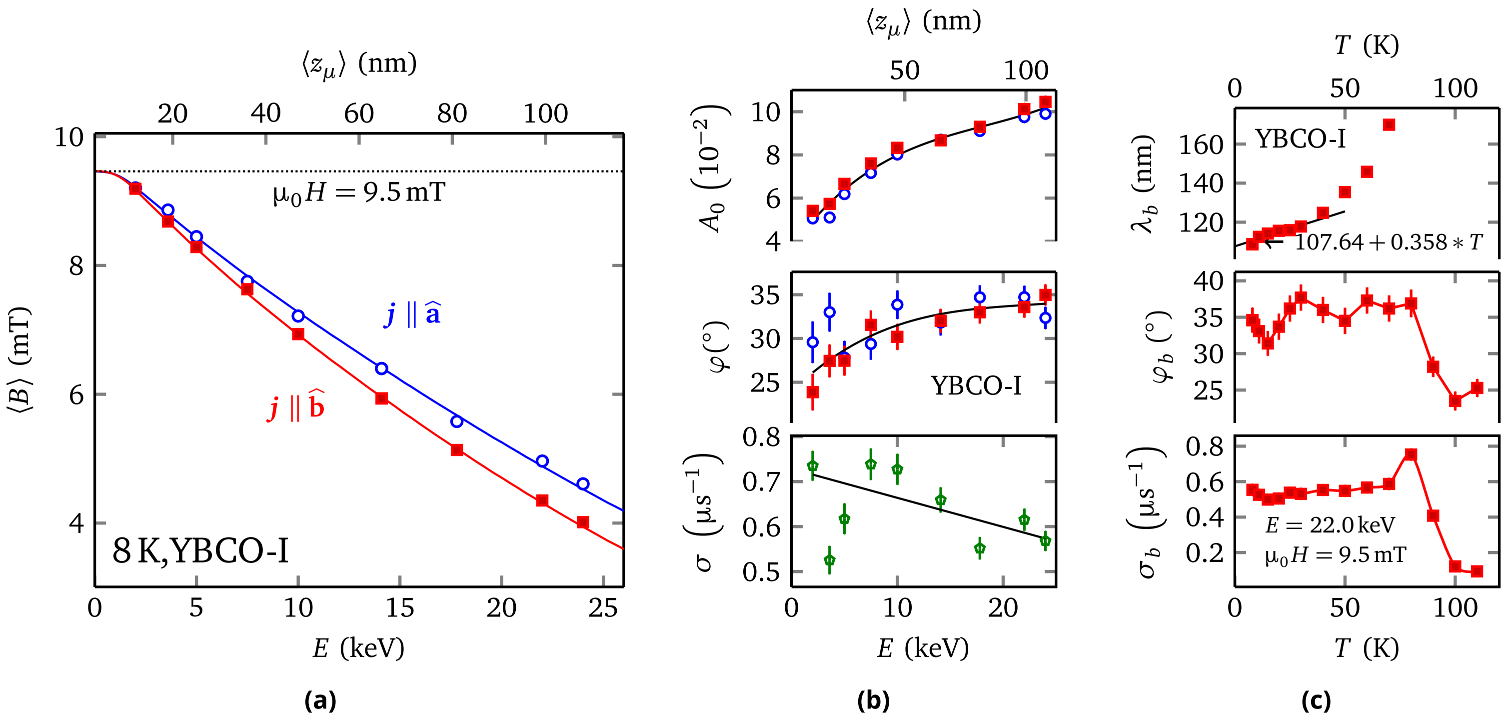

Figure 4.6: (a) The average magnetic field ($\langle B \rangle$) versus mean stopping depth in an applied field of 9.46 mT such that the shielding currents are flowing in the a direction ($\overrightarrow{j} \parallel a$,○) and b direction ($\overrightarrow{j} \parallel b$,■). The curves are the average fields generated from a global fit of all the spectra at 8 K taken at all energies and for both orientations. The common parameters are λ_a, λ_b and d. The individual points are from a fit to the same model but at a single depth. The differences between the data points and curves reflect how close the data at a single energy agrees with the global fit. (b) The phase, asymmetry and broadening parameter versus E. (c) Temperature dependence of λ, φ and σ when $\mu_0 H \| \widehat{\boldsymbol{b}}$. More details are in the text.

Figure 4.6a shows the average local field [$\langle B \rangle = \int \rho(z) B(z) dz$] determined from fits at a single energy as a function of beam energy (bottom scale) and corresponding mean implantation depth (top scale). The filled circles (○) and filled squares (■) are from data taken with the shielding currents flowing along the a and b axes respectively (or equivalently the magnetic field along the b and a axes respectively). The corresponding London model curves are generated from a global fit of runs taken at 8 K for both orientations and all energies using the calculated TRIM.SP implantation profiles. The common parameters are $\lambda_a = 128.9(12)$ nm, $\lambda_b = 108.4(10)$ nm and $d = 10.3(4)$ nm. In the **shared phase model**, d is fixed to 10.3 nm and the obtained $\lambda_{a,b}$ differs by ~ 1 nm as shown in the table 4.1. Statistical uncertainties are determined from the global χ^2 surface and take into account the strong correlation between $\lambda_{a,b}$ and d. Since there is almost no correlation between d and λ_a/λ_b, this ratio is determined more accurately than the absolute values of λ_a and λ_b as may be seen in the table 4.1. As may be evidenced from figure 4.6a, the average field falls exponentially from the surface for higher implantation energies however, close to the surface, deviation from a simple exponential is modelled from the curvature at the lowest energies. This implies that the supercurrent density is suppressed near the surface relative to a London model. This is idealized but the nature of the data does not warrant more complicated models. It is unclear to what extent this suppression of the supercurrent density is intrinsic as a result of the discontinuous nature of electronic properties near a surface. Higher average field from ME analysis is likely due to trapped vortices close to the surface and from fields expelled from neighboring crystals. A suppression of the supercurrent density was reported in a previous low energy μSR study of the field profile in a thin film of $YBa_2Cu_3O_{6.92}$ and attributed to surface roughness [162]. It is difficult to exclude such extrinsic effects which could also lead to a suppression of the supercurrent density near a surface. Measurements on atomically flat cleaved surfaces are needed to resolve the origin of d. There are no other measurements of electromagnetic properties as a function of depth in $YBa_2Cu_3O_{6.92}$ crystals to compare with. Surface sensitive techniques such as STM and ARPES are only sensitive to the top few unit cells where the properties can be very different than in the bulk.

It may also be noted from the figure 4.6b, that the fitted asymmetry goes from 5 %(low energy) to 10 %(high energy). This is expected since at low energies, incoming muons have an angular distribution as they approach the sample surface and at lower energy, many of them are deflected backwards, i.e, backscattering reduces the number of total muons, reducing the signal strength and asymmetry. The average phase from **individual phase model** is close to that from the **shared phase model**, indicating that the latter model determines an “effective average phase”. The broadening parameter σ’s energy dependence reflects the random local fields and is also temperature independent below $0.8\,T_c$, as expected and evidenced from the figure 4.6c. This is due to the bulk magnetization effects, whereby flux expelled from neighboring crystals broadens the magnetic field distribution at the

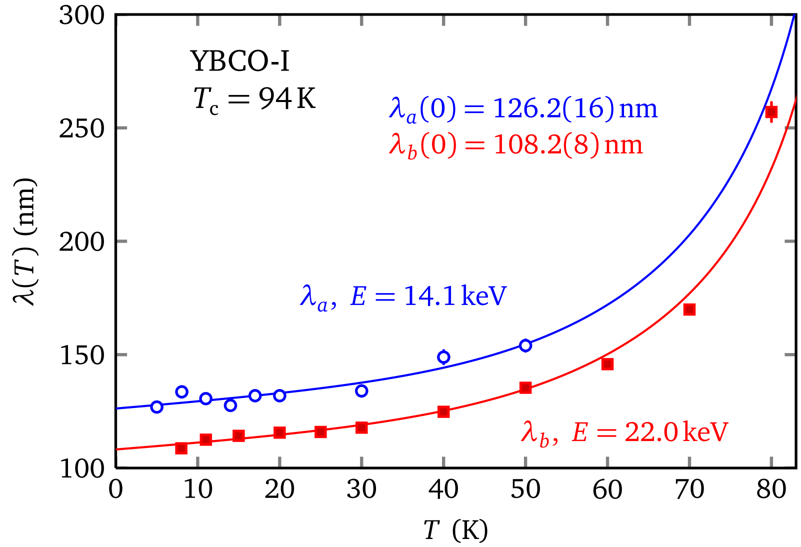

Figure 4.7: Temperature dependence of penetration depths.

surface of any given crystal. Since σ reflects the broadening of an **effective field** at a specific energy, it is always kept as a free parameter both in **individual phase model** and **shared phase model**.

The absolute value of λ_b as a function of temperature is shown in figure 4.6c (top panel). The data points are the fitted values of λ_b determined from a fit to the model at a single implantation energy of 22 keV. Since d is not temperature dependent it was fixed at 10.3 nm. The solid line is a linear fit of our data below 30 K and gives a slope of 0.357(67) nm K^{-1}. This was used to extrapolate our measurement of λ_b at 8 K down to zero temperature. The slope and extrapolated value depend slightly on the fitted temperature range adding an additional systematic error of about 1 nm. To obtain $\lambda_a(0)$, normalized superfluid density in a and b axis directions are taken as approximately equal as in the (4.9)

$$\left(\frac{\lambda_a(0)}{\lambda_a(T)}\right)^2 \simeq \left(\frac{\lambda_b(0)}{\lambda_b(T)}\right)^2$$
$$\Rightarrow \lambda_a(0) = \lambda_b(0)\left(\frac{\lambda_a(T)}{\lambda_b(T)}\right), \tag{4.9}$$

where $\lambda_{a,b}(T)$ are the finite temperature penetration depths measured by our modified London model.

Table 4.1 gives our results for λ_a and λ_b measured at 8 K in $YBa_2Cu_3O_{6.92}$. The errors reported here are just the statistical uncertainty. Systematic errors due to uncertainties in the muon stopping distribution and due to extrapolation to 0 K is $\sim 3\%$. At the moment, the latter dominates the overall uncertainty but should improve with refinements of the stopping distribution calculations. More details about possible slightly different stopping

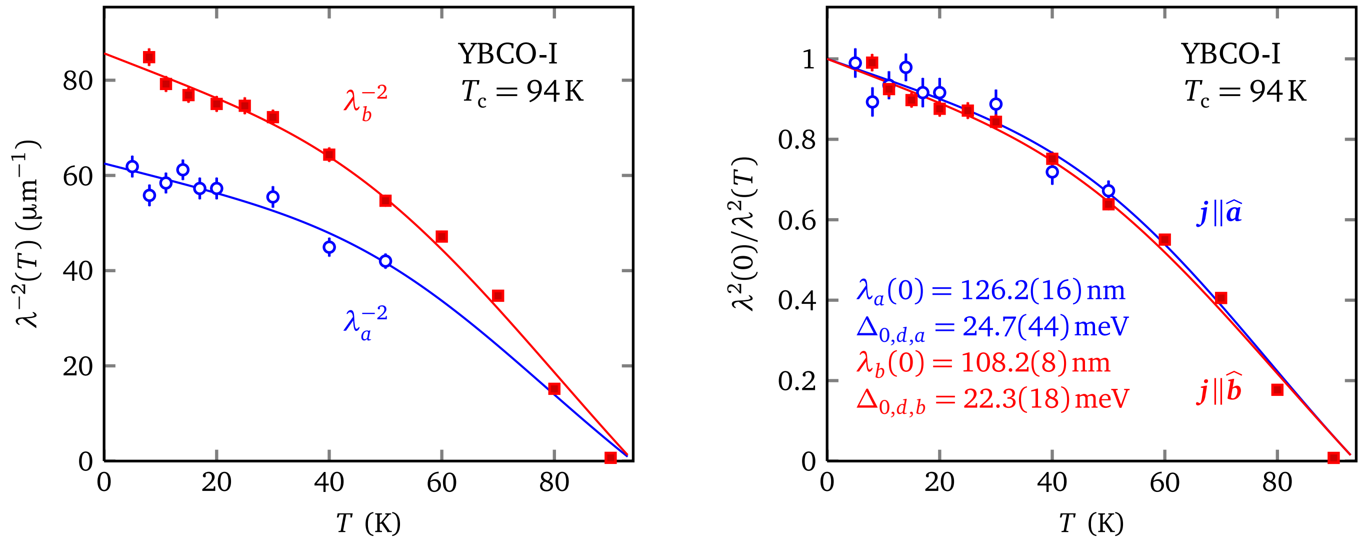

(a) **(b)**

Figure 4.8: Temperature dependence of penetration depths and normalized superfluid density.

Table 4.1: Summary of results in $YBa_2Cu_3O_{6.92}$: Measured London penetration depths at 8 K are shown for two models: "phase individual" and "phase shared", for individual energies. The errors are reported here are just statistical errors. An additional $\sim 2\%$ (~ 2 nm) error is due to uncertainty in stopping distribution. It may be noted that the two phase models yield penetration depths within a nm of each other for both a and b axis, stressing that the determination of phase does not affect the measurement of absolute λ.

B (mT)	d (nm)	φ (°)	$\lambda_a(8\,\text{K})$ (nm)	$\lambda_b(8\,\text{K})$ (nm)	$\mathcal{R} \equiv \lambda_a/\lambda_b$	χ^2/DF
9.46	10.3(5)	32.2(6)[a]	128.9(12)	108.4(10)	1.19(1)	1.058
	10.3 (fixed)	33.0(8)[b]	130.2(14)	109.2(12)	1.19(1)	1.069

[a] Average of energy specific phases from "individual phase" analysis.
[b] Global phase from "shared phase" analysis.

profiles is available in the appendix. In summary we have used low energy μSR to measure the magnetic field profiles in the Meissner state of a mosaic of detwinned single crystals of $YBa_2Cu_3O_{6.92}$. The comparison of $\lambda_{a,b}$ values obtained here with those from different methods is deferred until a later section. Since the data analysis method for the next three sections will be very similar to this one, primarily differences will be mentioned.

4.1.2 $YBa_2Cu_3O_{6.998}$

In this section, total four sets of data are analyzed and presented: (i) in an external field of 4.7 mT at three temperatures 4 K, 5 K and 12 K (ii) in an external field of 9.5 mT at the temperature of 5 K.

Examples of the muon precession signals in the crystal mosaic may be seen in figure 4.9. Figure 4.9a shows the muon precession signal in the normal state at 100 K in a small magnetic field of 4.7 mT applied along the a axis of the crystals with an implantation energy at 23.1 keV. In figure 4.9a, the average frequency corresponds to the applied field with a

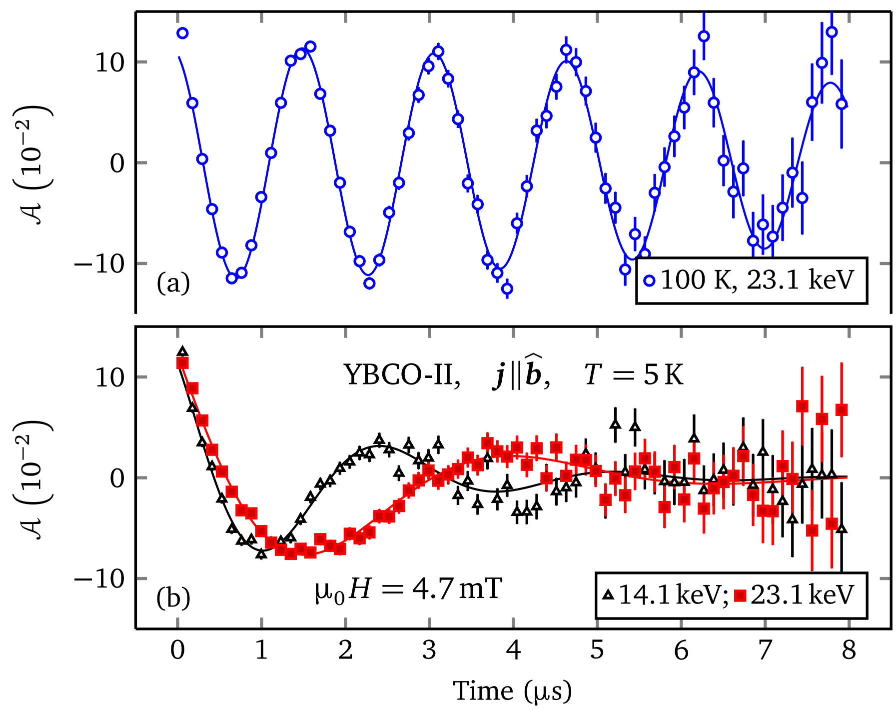

Figure 4.9: (a) The muon spin precession signal in the normal state of $YBa_2Cu_3O_{6.998}$ at 100 K, 23.1 keV in an external field of 4.7 mT applied parallel to the a direction.(b) The same conditions as (a) except in the superconducting state at $T = 5$ K with an two implantation energies 14.1 keV and 23.1 keV. The solid lines are fits to a London model profile described in the previous section.

damping rate of 0.110(10) μs^{-1}, which is slightly bigger than obtained in $YBa_2Cu_3O_{6.92}$ but nonetheless consistent with a random local field distribution. All measurements in the superconducting state were carried out under **zero-field-cooled** conditions in order to avoid flux trapping at the surface. Meissner screening of the external field is apparent by comparing the normal state in figure 4.9a with the superconducting states in figure 4.9b. The depth dependence of the average internal field(ω) is also perceptible by comparing the two spectras in figure 4.9b which have different implantation profiles. The curves in figure 4.9b are generated from fits to a London model profile as described in the previous section. Since, the precession signal spectra bear similar characteristic as figure 4.9, further precession plots are omitted for this sample.

Maximum entropy field distributions corresponding to the two external fields of 4.7 mT

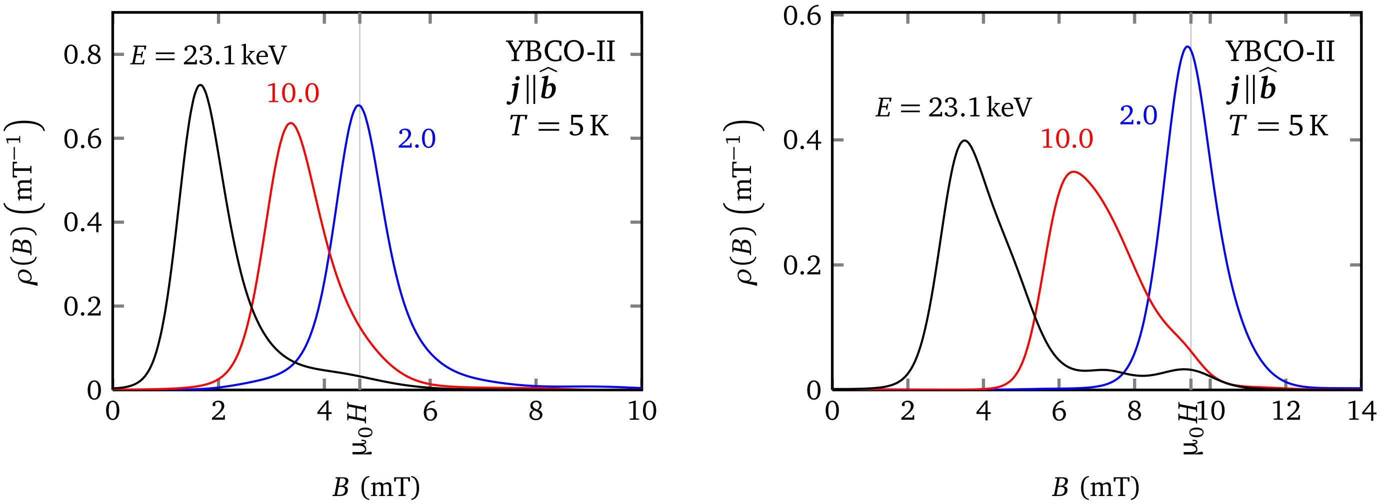

(a) **(b)**

Figure 4.10: Magnetic field distribution as seen by muons at various implantation energies and at $T = 5\,\mathrm{K}$ in an external applied magnetic field $(\mu_0 H)$ of 4.7 mT and 9.5 mT, applied parallel to the a axis.

and 9.5 mT are shown.in the figure 4.10. As may be noticed, $\rho(B)$, corresponding to the higher applied field (9.5 mT), is more asymmetric. However, in both cases, there are long tails, in field distributions, even at higher implantation energies possibly due to trapped vortices close to the surface.

The fitted asymmetry in figure 4.11 varies between 5 % (low energy) to 10 % (high energy). This is consistent with backscattering of muons at low energies. The phases for individual runs varies between $\sim 15° to 40°$. This range is also consistent with phases noticed in the previous section, underlining that the systematic errors in determining a precise phase remains the same. For low temperatures significantly below the critical temperature T_c, the broadening parameter σ is about $0.4\,\mu s^{-1}$ (bottom panel, figure 4.11) which is about half of that observed in $YBa_2Cu_3O_{6.92}$ in 9.5 mT. This is reasonable considering the magnetization effects coming from neighboring crystals will also be reduced with the reduced applied field of 4.8 mT. It may be also noted from figure 4.11 that the average σ at the external field, $B_\circ = 9.5\,\mathrm{mT}$, is about the same as that from $YBa_2Cu_3O_{6.92}$, figure 4.6 indicating that the broadening is due to expelled flux from crystals and is not very sensitive to the geometric arrangement of crystals in the mosaic.

Figure 4.12 shows the average local field $\langle B \rangle = \int \rho(z) B(z) dz$ determined from fits at a single energy as a function of beam energy (bottom scale) and corresponding mean implantation depth (top scale). The open circles and filled squares are from data taken with the shielding currents flowing along the a and b axes respectively (or equivalently the magnetic field along the b and a axes respectively). As may be noticed in figure 4.12, the

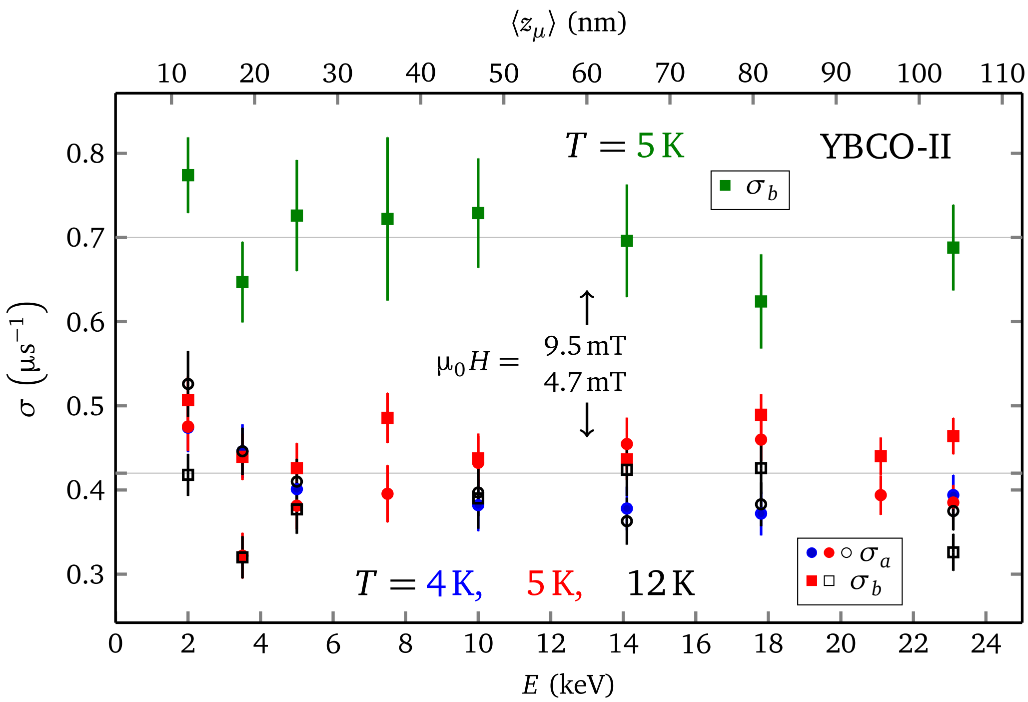

Figure 4.11: Broadening parameter: The three important parameters for individual energy runs in the global fit, with shared λ_a, λ_b and d are shown. The broadening parameter (σ) shows some random variation with an average $\sim$0.42 μs^{-1} at the external field $\mu_0 H = 4.7\,\mathrm{mT}$; the higher values at low energy may be due to vortices entering the samples close to the surface and broadening the field distribution.

theoretical global fit $\langle B \rangle$ line(s) are in excellent agreement with the individually measured $\langle B \rangle$. The common parameters are are all shown in the table 4.2 and $\lambda_{a,b}$ along with chi^2/DF are plotted in the figure 4.16. Since there is almost no correlation between d and λ_a/λ_b, this ratio is determined more accurately than the absolute values of λ_a and λ_b as shown in the seventh column of the table 4.2. Slightly different penetration depths $\lambda_{a,b}$ and other parametes are obtained in the **individual phase model** compared to the **shared phase model**. The differences in averge field from the two models is negligible.

Figure 4.15 shows the temperature dependence of penetration depth λ_a at 4.7 mT and 23.1 keV. The λ_a's are obtained via the method of "individual phase" analysis of measurements with a d fixed to 14.79 nm, obtained from global fit of measurements in both a and b direction. The measured λ_a's are fitted to a line giving λ_a(0 K)=(112.26 $\pm$ 1.46) nm and slope of the line $(\Delta\lambda/\Delta T = 0.495 \pm 0.078$ (nm/K). Since these measurements were done at a single energy, λ_a(0 K) isn't a very good measure of penetration depth at zero temperature; however, note the closeness (λ_a(5 K)$\sim$115 nm) with the absolute λ_a's found from global fits table 4.2. The $\Delta\lambda/\Delta T$ is a good measure of low temperature dependence

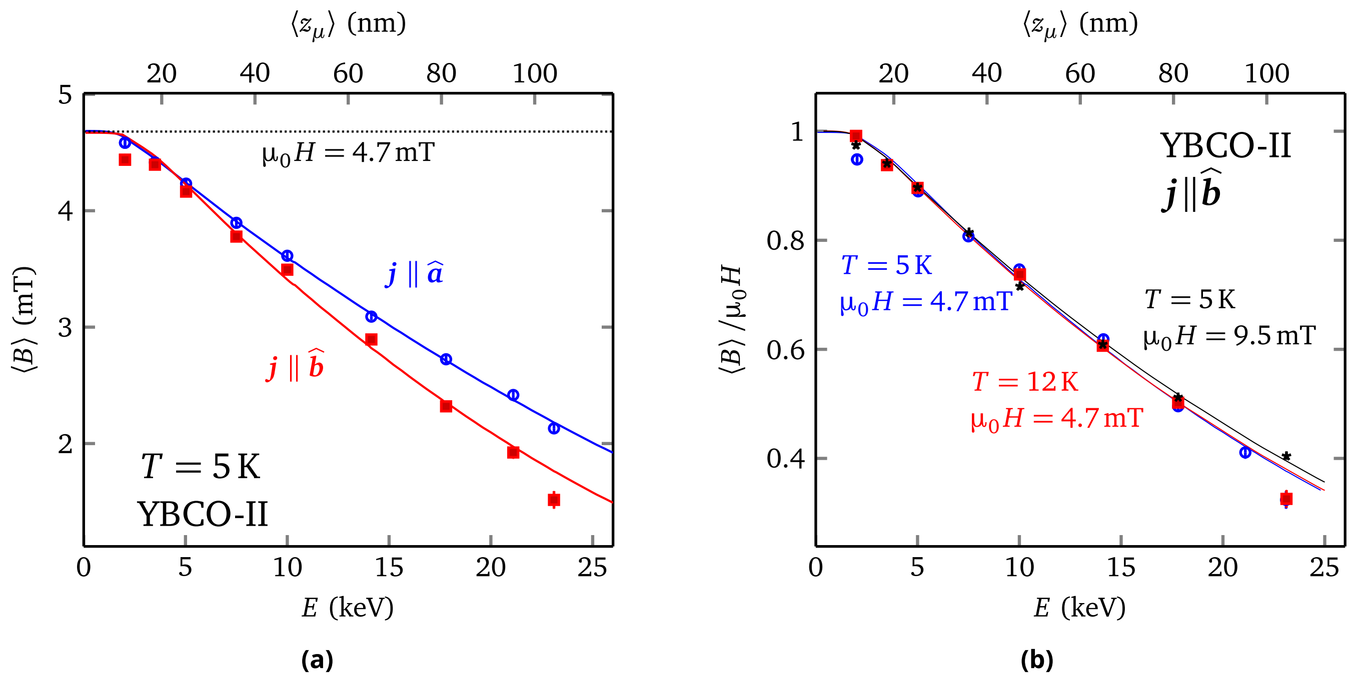

Figure 4.12: (a) The average magnetic field (⟨B⟩) versus mean stopping depth in an applied field of 4.7 mT. The curves are the average fields generated from a global fit of all the spectra at 5 K taken at all energies and for both orientations (cf. figure 4.6). (b) Relative average magnetic fields in this sample for two temperatures and two magnetic fields. It is apparent that the absolute London penetration depths measured here are, differ only slightly.

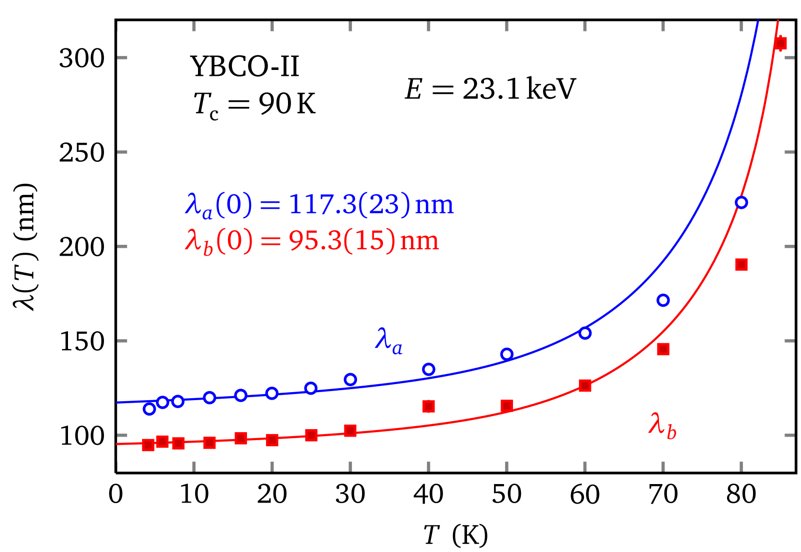

Figure 4.13: Temperature dependence of penetration depths.

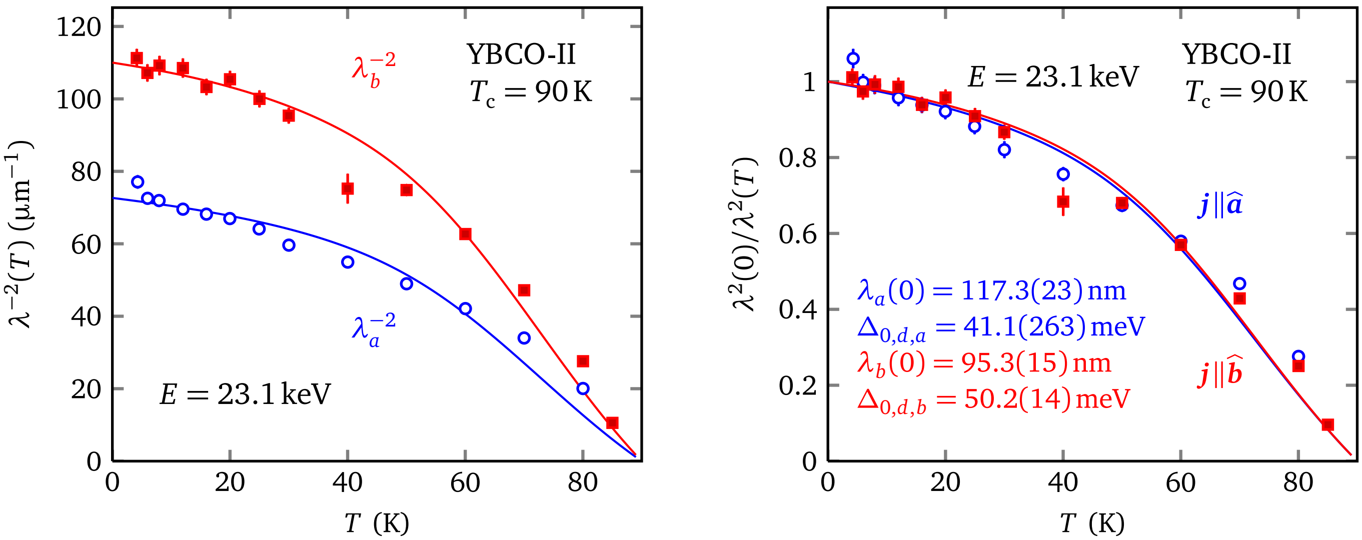

(a) **(b)**

Figure 4.14: Temperature dependence of penetration depths and normalized superfluid density.

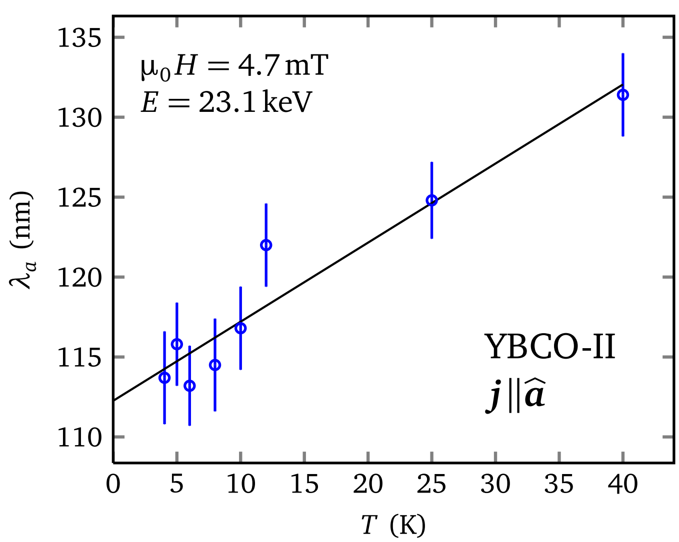

Figure 4.15: Temperature dependence of London penetration depth with in low temperatures are shown. The muon beam energy for this set of runs is E=23.1 keV and an external field of 4.7 mT is applied parallel to b-axis. A linear fit of $\lambda_a(T)$ yields $\lambda_a(0) = 112.26 \pm 1.46$ and $\Delta\lambda/\Delta T = 0.495 \pm 0.078$. The slope was used to extrapolate finite temperature penetration depth to 0 K.

Table 4.2: Summary of results for $YBa_2Cu_3O_{6.998}$: Measured London penetration depth in external fields of 4.7 mT & 9.5 mT are shown, for "phase individual" and "phase shared" models. There is some φ-dependence (of the order of systematic uncertainty) of measured penetration depths. It's interesting to note that the "dead layer" d is within 10 to 20 nm indicating that it is a temperature and magnetic field invariant quantity. The shared phase is for 4.7 mT experiments is $\sim 25°$ and slightly higher for the 9.5 mT set of runs. The χ^2/DF is slighly less for "individual phase" models, which indicates better fits.

B (mT)	T (K)	d (nm)	φ (°)	λ_a (nm)	λ_b (nm)	$\mathcal{R} \equiv \lambda_a/\lambda_b$	χ^2/DF
4.66	4	14.8(9)	27.0(16)[a]	115.6(18)	∅	∅	1.323
			25.9(13)[b]	119.2(24)	∅	∅	1.385
4.67	5	17.2(15)	27.0(16)[a]	107.5(39)	84.0(35)	1.28(2)	1.257
			23.0(13)[b]	114.2(26)	92.7(22)	1.23(1)	1.382
4.66	12	16.8(6)	27.9(15)[a]	117.2(25)	87.7(21)	1.34(3)	1.448
			25.4(6)[b]	120.3(18)	93.9(14)	1.28(1)	1.586
9.49	5	16.5(8)	31.1(20)[a]	∅	91.9(22)	∅	1.105
			30.1(16)[b]	∅	94.4(17)	∅	1.135

[a] Average of energy specific phases from "individual phase" analysis.
[b] Global phase from "shared phase" analysis.

of λ_a and will be used to extrapolate zero temperature penetration depths from the finite temperature ones.

It is may be noted that $\lambda_{a,b}$ increases slightly as temperature is increased (4K to 5K) which is consistent with $\sim 0.5\,\mathrm{nm\,K^{-1}}$ increase, as found from the temperature dependence in the figure 4.15. It may also be noted that the ratio between the two penetration depths, $\mathcal{R}$, slightly ($\sim 4\%$) depend on whether the **individual phase model** or the **shared phase model** was used. However, the difference is within statistical ($\sim 1\% to 2\%$) and systematic uncertainty ($\sim 3\%$) in $\lambda_{a,b}$. The **goodness of fit** χ^2/DF becomes slightly worse ($\sim$ 10%) with **shared phase model**, although, global phase is determined within a statistical error of $\sim 2\%$.

We will now summarize the analysis of this section as found in the table 4.2 and figure 4.16. It is interesting to note that the **dead layer** d, the layer close to the surface of the crystals where supercurrent is suppressed, varies only between $15\,\mathrm{nm} to 17\,\mathrm{nm}$ where in $YBa_2Cu_3O_{6.92}$, it was found to be 10.3 nm. Regardless of the temperature, oxygen doping & applied external magnetic field, there seems to be an thin ($\leq$ 10%) outside layer where the supercurrent is suppressed. Regardless of the **phase models**, the determination of phase is not very sensitive to whether we have data along both axis or just one axis. Determination of phase is important since fitted values of $\lambda_{a,b}$ depends slightly on whether phases are energy specific or a single phase should be assumed for the entire set of runs. To discern between phase and frequency (and thereby average field), more oscillations in siganl is better, which is feasible closer to the surface. Deeper in the sample, field drops by a siginifant fraction and thereby frequency becomes proportionately low which results in phase & average frequency somewhat correlated. Yet, the correlation among φ and ω doesn't produce significant uncertainty in d and $\lambda_{a,b}$ as they are determined from a range of implantation energies (i.e global fit). This may be observed from the plot of phases as function of energy in figure 4.11, that the errors in phases are about the same in both low (closer to surface) energies and high (deeper in the sample) energies. The sharp increase in σ at lower implantation energies (close to surface) is possibly due to pinned vortices at the top layers of the crystals. Broad field distribution close to the surface doesn't, however, influence determination of λ as the latter depends primarily on the field distribution deeper in the sample. The fitted phases are found to be almost temperature independent, however weakly field dependent, as φ increases $\sim 5°$ as the applied field becomes doubled. With the mozaic of $YBa_2Cu_3O_{6.92}$, global φ was found to be 33.0 ± 0.8 at an external magnetic field of 9.5 mT. While the origin of phases' dependence on applied magnetic field remains to be understood, the determination of the London penetration depths $\lambda_{a,b}$ and their ratio $\mathcal{R}$ can be determined with with a few percent uncertainty. With our simple model of London penetration depth, dead layer d and penetration depths $\lambda_{a,b}$ are inversely correlated, as d's increase will decrease $\lambda_{a,b}$ and vice versa. However, the ratio $\mathcal{R}$ is immune to the variations just mentioned and thereby has better accuracy. One important model (**phase**) dependent variation is the biggest uncertainty in determination of $\mathcal{R}$. Although measured at finite temperatures (4 K, 5 K and 12 K), $\mathcal{R}$ is a good measure of the penetration depth anisotropy down to 0 K, assuming the nomalized superfluid density being equal at both directions at any temperature as given in the (4.9).

As may be noticed the from table 4.2 and figure 4.16, that the χ^2/DF("goodness of fit") depends on applied external magnetic field strongly and slightly on the (phase) model. Higher external field induces more oscillations in the spectrum & thereby average magnetic field(frequency) inside the sample can be determined with better accuracy. The χ^2/DF for 9.5 mT set of measurements in $YBa_2Cu_3O_{6.998}$ is very much comparable to that of $YBa_2Cu_3O_{6.92}$. χ^2/DF also is smaller (better fit) for a fit with energy specific phases compared to a global phase. This is expected as more free (fit) parameters mean more degrees of freedom for the model and a better fit, however it introduces correlations among variables φ, σ and asymmetry. Nonetheless, statistical uncertainty in "shared phase" model is better as χ^2/DF is inversely correlated with the number of parameters. Model dependent uncertainties can be avoided if better measurements of phase may be done for a specific set of measurements. In the following section, we have a better determination of phase in a novel way, which avoids the uncertainty from a lack of knowledge of unique phase. However, it should still

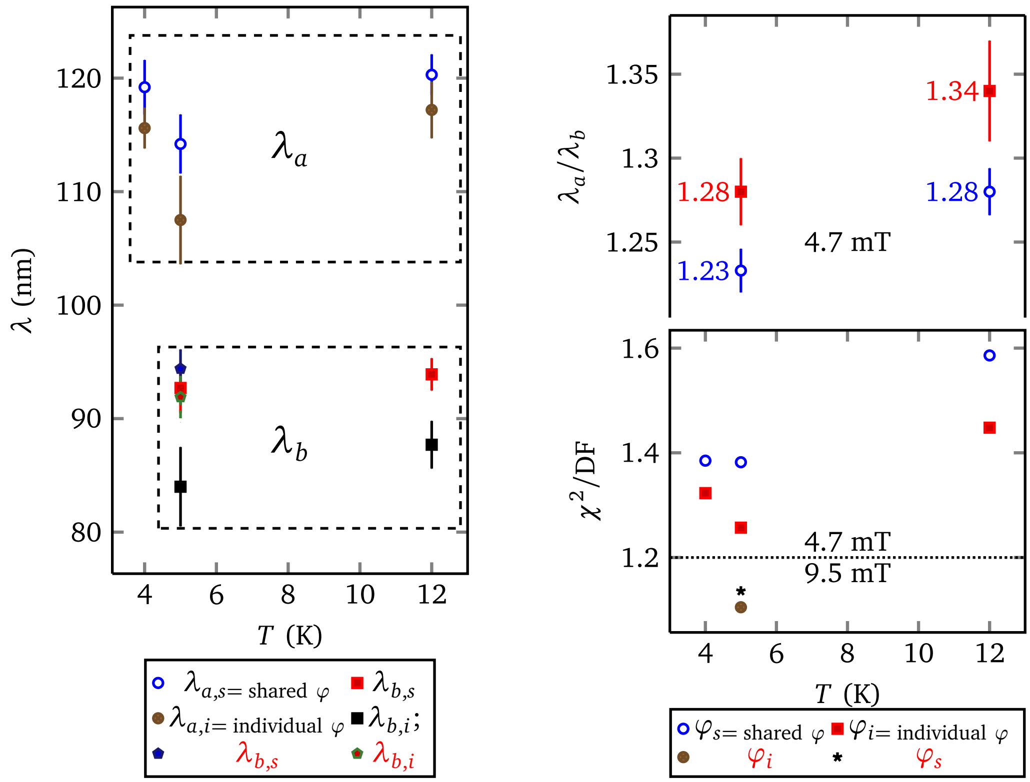

(a) **(b)**

Figure 4.16: Summary of results for $YBa_2Cu_3O_{6.998}$: Measured London penetration depth in external fields of 4.7 mT & 9.5 mT are shown, for **individual(shared) phase** models. There is some φ-dependence (of the order of systematic uncertainty) of measured penetration depths. The λ_a/λ_b and χ^2/DF is slighly less for **individual phase model**, which indicates better fits. More discussion are in the text.

be noted that model dependence of $\lambda_{a,b}$ only introduces an additonal error of the order of statistical uncertainty from a single model.

4.1.3 $YBa_2Cu_3O_{6.52}$

As has been discussed in the sections 4.1.1 and 4.1.2, determination of London penetration depths $\lambda_{a,b}$ although may be done with a few percent statistical uncertainty, the **shared phase** vs **individual phase** models introduces additional systematic uncertainties in obtained $\lambda_{a,b}$. To have a simpler model having one effective phase (depending on when muon enters into sample and partially on other geometric factors), a novel method was used to determine φ. Two normal state runs were taken at a single field (to be determined from fit) but one of them having it's direction reversed. The resulting spectra is plotted in the figure 4.17. These normal states runs were taken, as a standard procedure, *after* the superconducting state runs in zero-field-cooled magnetic field, to avoid any flux trapping and to have an accurate

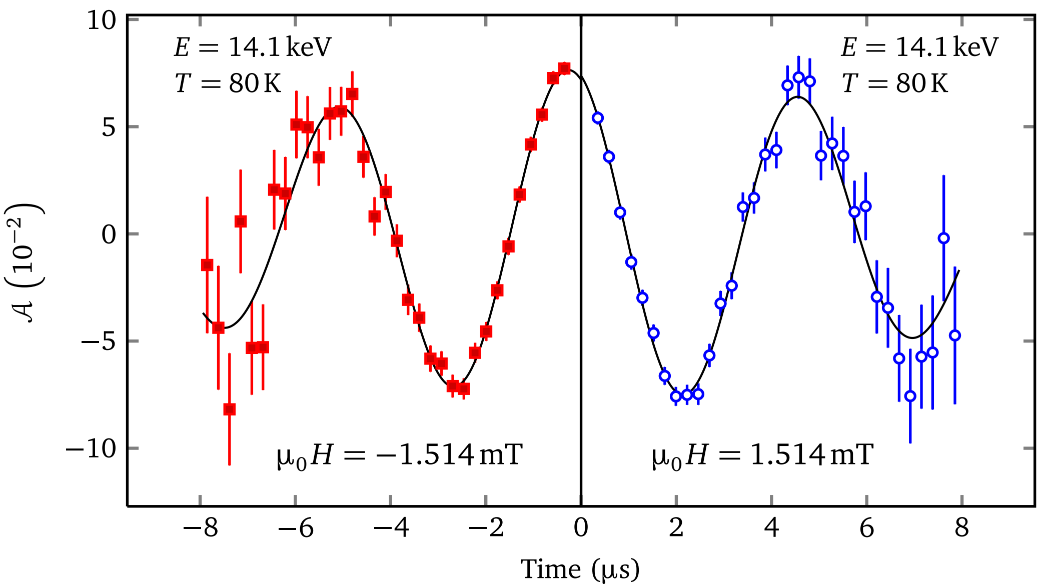

Figure 4.17: YBCO 6.52 in an applied field of 1.45 mT & -1.45 mT at 80K. Field reversing is like taking a measurement in negative time. $\varphi = 20.1 \pm 1.0$ and $\sigma = 0.14(1)$

determination of normal state field. Having a negative magnetic field $-B$ is identical to having a precession in negative time, as

$$\omega t \equiv \gamma_\mu(-B)t = (\gamma_\mu B)(-t).$$

These precessions with B and $-B$ fields essentially double the length of muon precession time and fitting to the entire length with asymmetry sprectrum function

$$\mathcal{A}(t) \equiv A_0 \exp\left[-\sigma^2 t^2/2\right] cos(\gamma_\mu B_\circ t + \varphi_\circ)$$

one can determine $\mu_0 H$, φ and σ (for normal state). The fitted values from figure 4.17 were found to be $\mu_0 H = 1.514(6)\,\mathrm{mT}$, $\varphi = 20.1(10)^\circ$ and $\sigma = 0.14(1)\,\mu\mathrm{s}^{-1}$. This unique determination of phase is specially crucial at low field since, muon oscillation frequencies ($\omega = \gamma_\mu B$) are also lower and fewer full oscillations are available (thereby a large correlation between φ and ω) in the sprectrums as may be viewed in figure 4.18. Note the clear reduction in precession frequency (thereby, interal field) in figure 4.18 from normal state to superconducting states. This should be stressed that treating φ to be a geometric parameter and to be equal to the normal state phase is a deviation from the analyses done so far. However, with the set of runs with 1.5 mT external field, only a fixed phase (20.1, found from normal states) analysis is shown in table 4.3 as a global fit with **shared phase model** results in unrealistic average magnetic fields close to the surface. Fixing φ to the normal state values yields a better estimate of average frequencies, although usually a higher χ^2/DF. However, it may be noticed from table 4.3 that 1.5 mT set of runs yields the lowest χ^2/DF as well. The other two sets of measurements with higher external fields of 4.6 mT and 7.8 mT are analyzed with both a fixed phase (20.1) and with a **shared phase model**.

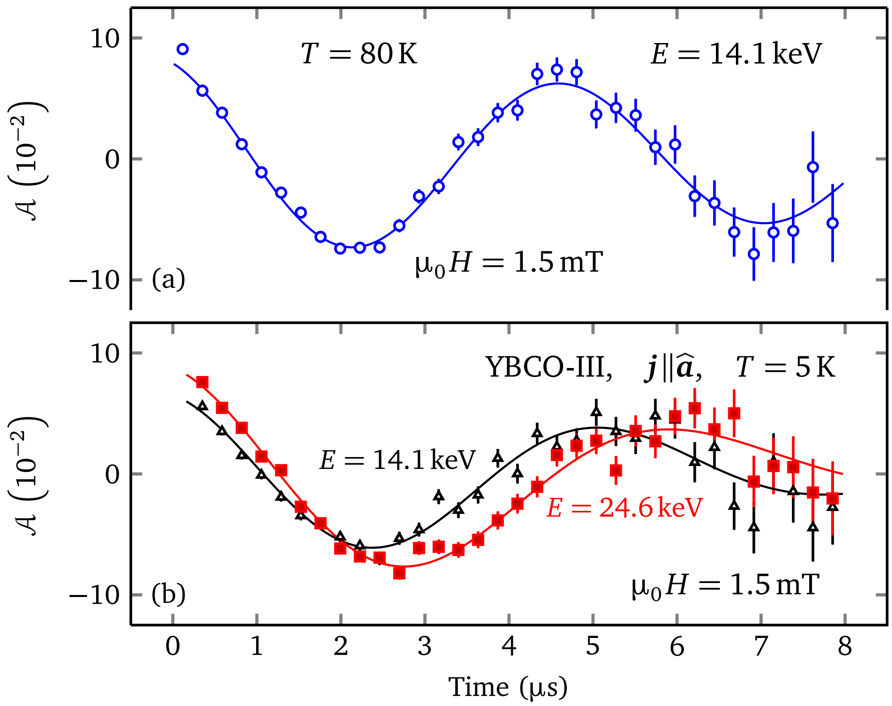

Figure 4.18: Top: The muon spin precession signal in the normal state of $YBa_2Cu_3O_{6.52}$ at 80 K in an external field of 1.5 mT applied parallel to the b-direction. The mean implantation energy is $E = 14.1$ keV which corresponds to a mean implantation depth of 65 nm. Bottom: The same conditions as above except in the superconducting state at $T = 5$ K with energy 14.1 keV & 24.6 keV.

The fitted asymmetry and depolarization rate σ corresponding to the individual energies' in the global fit setup at $\mu_0 H = 1.5\,\mathrm{mT}$ are shown in the figure 4.19. As may be noticed, the asymmetry rises with muon incident energy just like the previous experiments have shown, however, the very linear fashion of rise is interesting. It may also be noted that the range for asymmetry variation is $\sim 4\% - 10\%$, meaning that there is no significant loss of signal strength compared to the experiements done on $YBa_2Cu_3O_{6.92}$ and $YBa_2Cu_3O_{6.998}$. The damping rate σ is about the same as the value obtained in previous sections at higher magnetic fields. This is reasonable damping from host Cu nuclear dipole moments. One other feature is that σ is almost invariant as a function of implantation energy, as is ideally expected, but close to the surface, it rises significantly. This suggests that the actual field distribution is broader than than expected from a purely stopping distribution $\rho(z)$ related one. One possible source of broadening is field expelled from neighboring crystals. However,

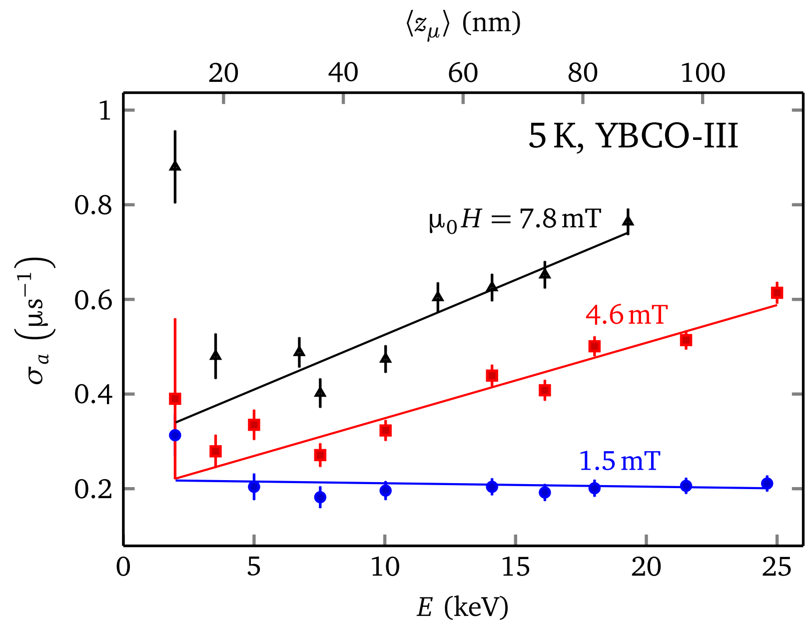

Figure 4.19: YBCO 6.52 broadening parameter are shown for an external applied field of 1.45 mT, 4.6 mT and 7.8 mT such that the shielding currents are flowing in the a direction ($\boldsymbol{j} \parallel \widehat{\boldsymbol{a}}$). The common parameters are λ_a, λ_b and d. The upturn in σ at lower energies are possibly due to vortex entrance close to the surface. The solid lines are guides to the eye.

that would increase (not observed) the average field close to the surface. More feasible is the possible entrance of magnetic vortices close to surface which would introduce broadening in magnetic field while maintaining an average field close to the external applied field. Higher external fields in the figure 4.19, yields $\sigma(E) \propto E$. It may be speculated that vortices enter into significant percentage of area close to the surface and just below $\sim$ nm of the sample surface, very few vortices remain, however the vortex core gets widened in as it gets deeper into the sample, thereby increasing the width of the field distribution.

Figure 4.21 shows the average λ and individually fitted (with d fixed) λ for 1.5 mT and 4.6 mT external fields. It may be noted that the global fits well represent the individual energy specific fits except at low energies, where $\langle B \rangle$ isn't very sensitive (thereby large error bars) to the penetration depths. Although λs' show large error close to the surface, the error produced in $\langle B \rangle$ is considerably smaller as only dead layer d dominates the average magnetic field computation in this region. Fitting the set of superconducting state runs at 1.5 mT with a London model, as described earlier, global $\lambda_{a,b}$ and dead layer d are determined. The corresponding global and individual average magnetic fields are shown in the figure 4.22a. The closeness of the individual average field points to the global fit lines represent how close the data at single energies agree with global fit with shared $\lambda_{a,b}$ and d. A comparison of relative average magnetic field for 1.5 mT, 4.6 mT and 7.8 mT is shown

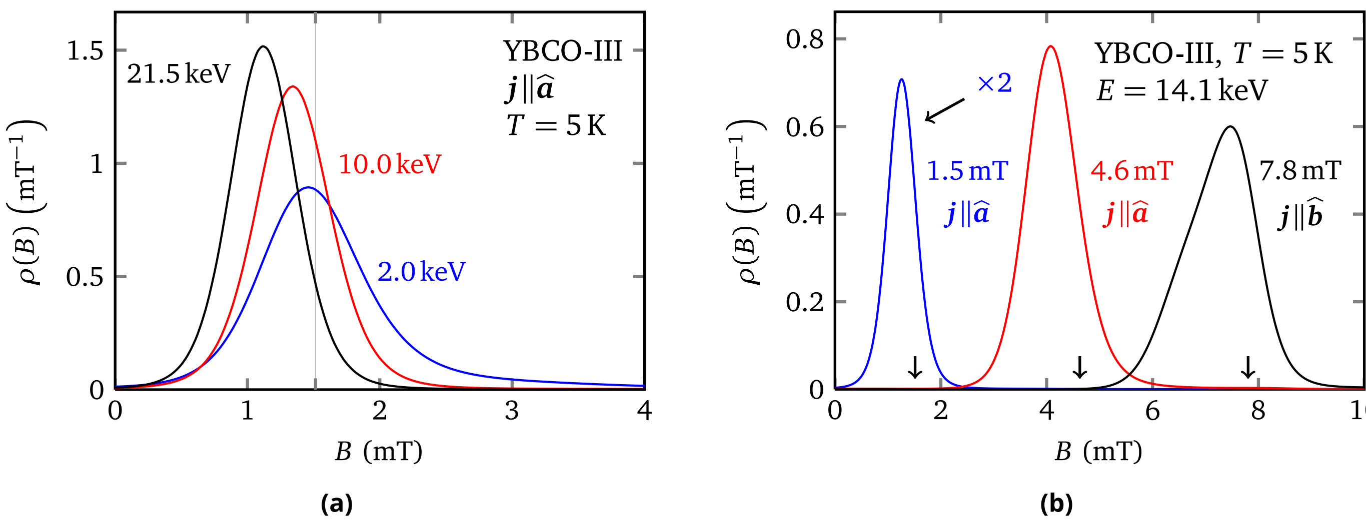

Figure 4.20: Magnetic field distribution as seen by muons at various implantation energies and at $T = 5\,\mathrm{K}$ in an external applied magnetic field $(\mu_0 H)$ of 1.5 mT and 4.6 mT, applied parallel to the b axis.

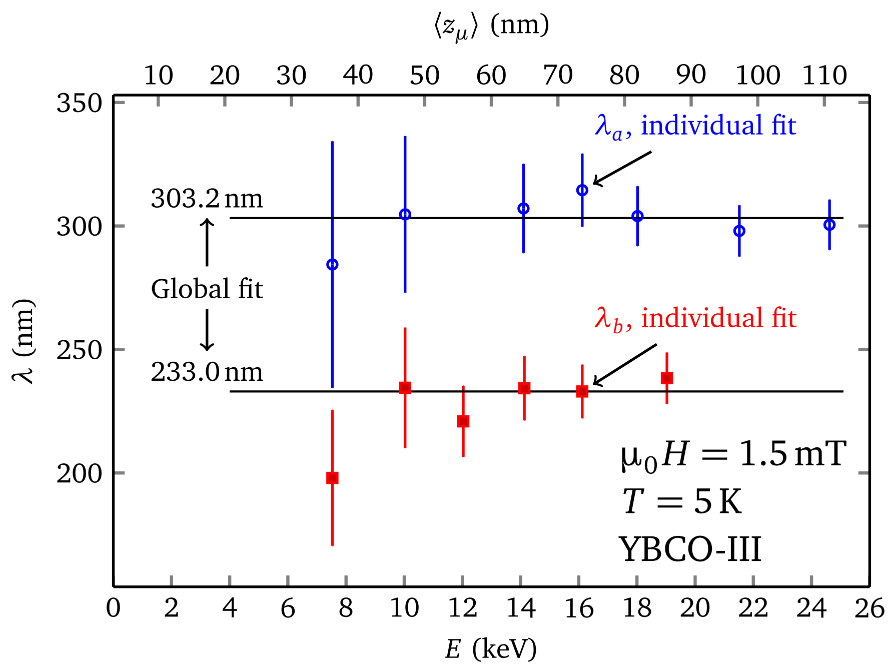

Figure 4.21: Global fit λ and individually fitted λ's are shown for the external field of 1.5 mT. As may be noticed, individual penetration depths scatter around the global fit values except at lowest energies, since at these energies λ is less sensitive measure to the average magnetic field $\langle B \rangle \approx B_0$.

in the figure 4.22b. It is clearly evident that the lowest $\lambda_{a,b}$ for this sample results from the 1.5 mT set of runs. As may be noticed the average field ($\langle B \rangle$) in the figure 4.22 doesn't drop until $\sim$ 5 keV, corresponding to an implantation energy $\sim$ 25 nm which is also reflected in the dead layer d in the table 4.3. One interesting phenomenon consistently seen in all analyses is that the d is between 10 nm to 30 nm, irrespective of the external field magnitude $\mu_0 H$ or orientation, suggesting that some intrinsic mechanism being responsible for the reduced supercurrent close to the surface. To extract $\lambda_{a,b}(0)K$, temperature dependent measurements of penetration depths have been obtained as shown in the figure 4.23. It may be noticed that low temperature dependence of λ is linear only at an external field of 1.5 mT. The higher external field of 4.6 mT yields very nonlinear temperature dependence possibly indicating entrance of vortices in the mosaic, as already argued noting that $\sigma(E)$ increases almost linearly, with higher energy, as shown in the figure 4.19. The unusual temperature dependence of $\lambda_a(T)$ in the 4.6 mT set of measurements prompted the signifincantly lower 1.5 mT set of measurements. The resulting slope from the 1.5 mT temperature dependence has been used to extrapolate $\lambda_b(5\,\mathrm{K})$ to $\lambda_b(0\,\mathrm{K})$. Penetration depth in the other orientation $\lambda_a(0\,\mathrm{K})$ has been obtained using the (4.9).

Figure 4.24a shows effective penetration depth λ_b's dependence on external field. The phase was left fixed at the normal state value at 1.5 mT, for all three analyses. As argued before, the two higher field of 4.6 mT and 7.8 mT have possible vortex penetration and obtained λ_a are just effective penetration depths which can be used to determine average magnetic field at various depths using the stopping distribution $\rho(z)$. Note that the effective λ_as from global fit are more reliable than the single run λ_bs (with a fixed $d = 23.6$ nm) shown in figure 4.24a. Although the individually fitted λ_b values are less reliable, the almost linear field dependence strongly suggests magnetic vortex entrance at higher fields. Also may be noted from the figure 4.24b, normal state phases to be almost independent ($\sim 25°$) of applied external field while the superconducting state phase seems to be slightly dependent on applied field for $\mu_0 H > 6$ mT. The broadening parameter σ in the superconducting state rises almost linearly with the applied external magnetic field due to the expelled flux being proportional to the applied field. Although the single fit λ_bs in the figure 4.24a are not very reliable, it does bring an important point that caution must be taken to measure the London penetration depth in the Meissner state by excluding possibility of vortices getting in the sample.

As may be seen from the table 4.3, a difference of $\sim$ 20 nm exist between the fixed phase and the shared phase models. A single normal state run at 4.6 mT yields a phase of $(23.5 \pm 1.8)°$ & $(0.039 \pm 0.013)°$. This is interesting because shared phase φ seems to suggest a different phase other than the one determined from 1.5 mT set of runs with a reversal of field. From the measured $\lambda_{a,b}$ in table 4.3, it's very likely only minor vortex penetration happened in 4.6 mT set of runs whereas a significant amount of vortices entered in a 7.8 mT

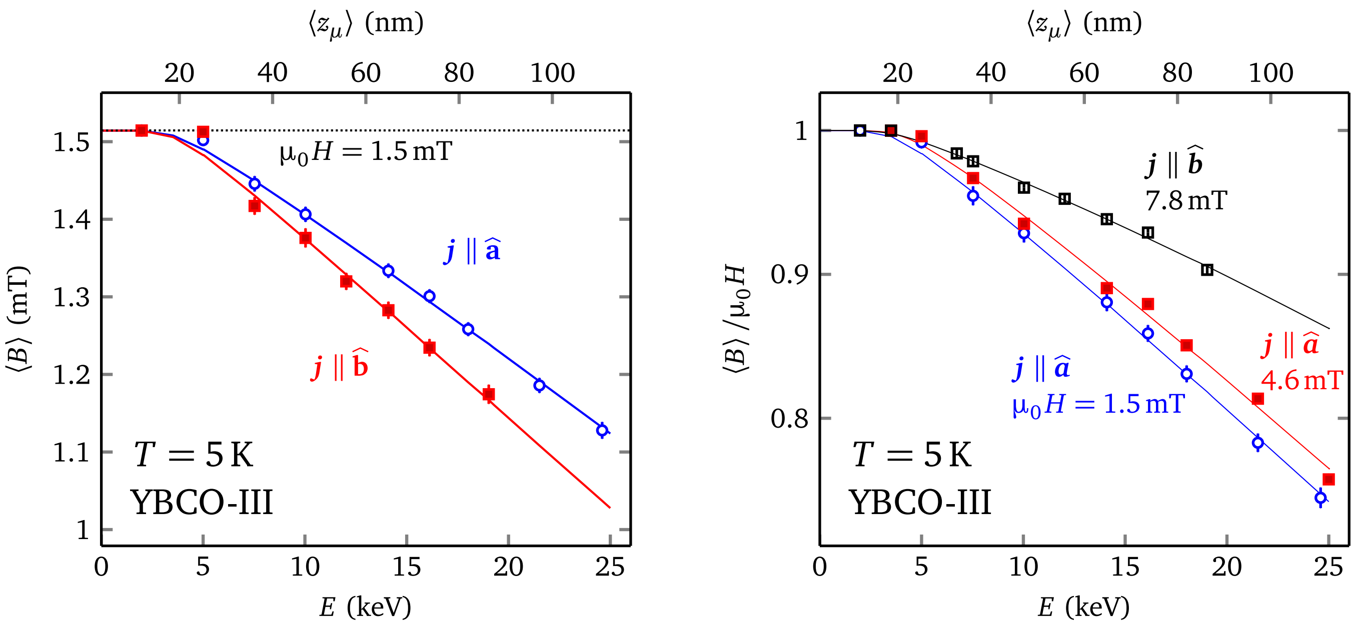

(a) **(b)**

Figure 4.22: YBCO 6.52 average magnetic field $\overrightarrow{B}$ inside the sample. The average magnetic field versus energy (mean stopping depth) in an applied field of 1.45 mT such that the shielding currents are flowing in the a direction ($\overrightarrow{j} \parallel a$, open circles) and b direction ($\overrightarrow{j} \parallel b$, filled squares). Relative average local magnetic field with respect to the applied field as a function of muon implantation energy for the two fields of 4.7 mT, and 9.5 mT applied parallel to the b axis of the YBCO-III. The depicted fields have been calculated in the same way as in Fig. and normalized to the applied fields.

set of runs, making the global λ very long. The "effective magnetic penetration" depth is also very sensitive to the muon phase φ, as may be seen in table 4.3. The phase in a "shared, global phase" analysis in this case $\sim 26.5°$ which is also close to the phase found from a single superconducting state analysis in figure 4.24. It is tempting to suggest that the "shared phase model" estimates the true phase. However, as may be seen from figure 4.24, the normal state phases vary little compared to the superconducting state phases and the latter has distinct field dependence, although with bigger error limits. The phases' dependence of magnetic field at higher applied fields, although an interesting one, doesn't affect the determination of absolute penetration depth at 0 K, extrapolated from measurements at 1.5 mT.

4.2 Pnictide

In this section, measurements of the λ in the Meissner state on a single crystal of $Ba(Co_xFe_{1-x})_2As_2$ are reported, using a combination of LE-μSR and microwave perturbation. The combination

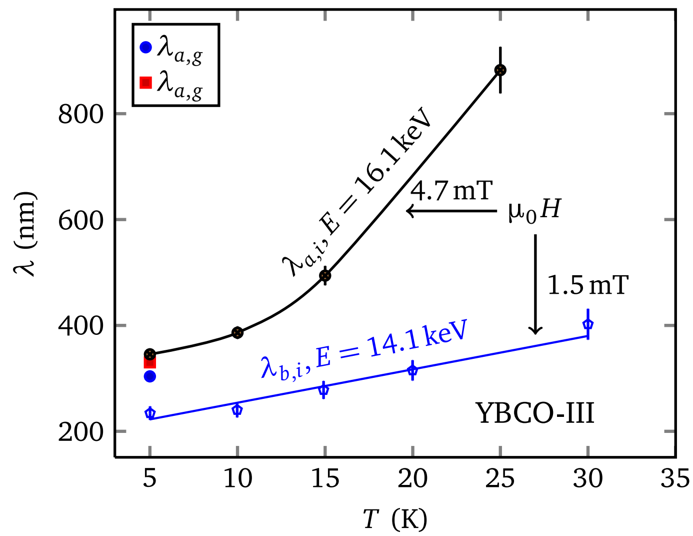

Figure 4.23: As may be noticed that the average field increases, with a corresponding large increase in λ, with temperature. Possible entrance of vortices is likely the reason of increase of "effective λ". This prompted us to take low field (1.6 mT) set of runs. The fit parameters at 1.5 mT external field are, intercept=191 ± 13.38 nm. slope=6.305 ± 0.96 nm/K. The slope is an order of magnitude bigger than that found in other oxygen dopings of YBCO.

Table 4.3: Summary of results in $YBa_2Cu_3O_{6.52}$: Measured London penetration depths at 5 K are shown for two models: "phase individual" and "phase shared", for individual energies. The errors are reported here are just statistical errors. An additional $\sim 2\%$ (~ 2 nm) error is due to uncertainty in stopping distribution. The deadlayer $d \sim 25$ nm, is found from "individual phase" model global fit & is assumed to be the same for "shared phase" model. In the lowest of the fields, 1.5 mT, phase is kept fixed to the measured phase found in the normal state, via field reversing. The lowest penetration depths were obtained for both a and b axis in 1.5 mT external field. The penetration depths at higher fields of 4.6 mT & 7.8 mT include contributions from vortices entering the sample, as may be observed from increasing σ at higher energies.

B (mT)	T (K)	d (nm)	φ (°)	λ_a (nm)	λ_b (nm)	$\mathcal{R} \equiv \lambda_a/\lambda_b$	χ^2/DF
1.51	5	23.6(18)	φ_n [a]	303.2(87)	233.0(92)	1.30(2)	1.027
4.63	5	26.6(12)	φ_n	330.3(90)	∅	∅	1.147
			24.6(10) [b]	310.0(75)	∅	∅	1.078
7.80	5	23.7(21)	φ_n	∅	616.3(428)	∅	1.098
			26.5(13) [b]	∅	536.6(339)	∅	1.069

[a] $\varphi_n = 20.1°$ (fixed)
[b] Global phase from "shared phase" analysis.

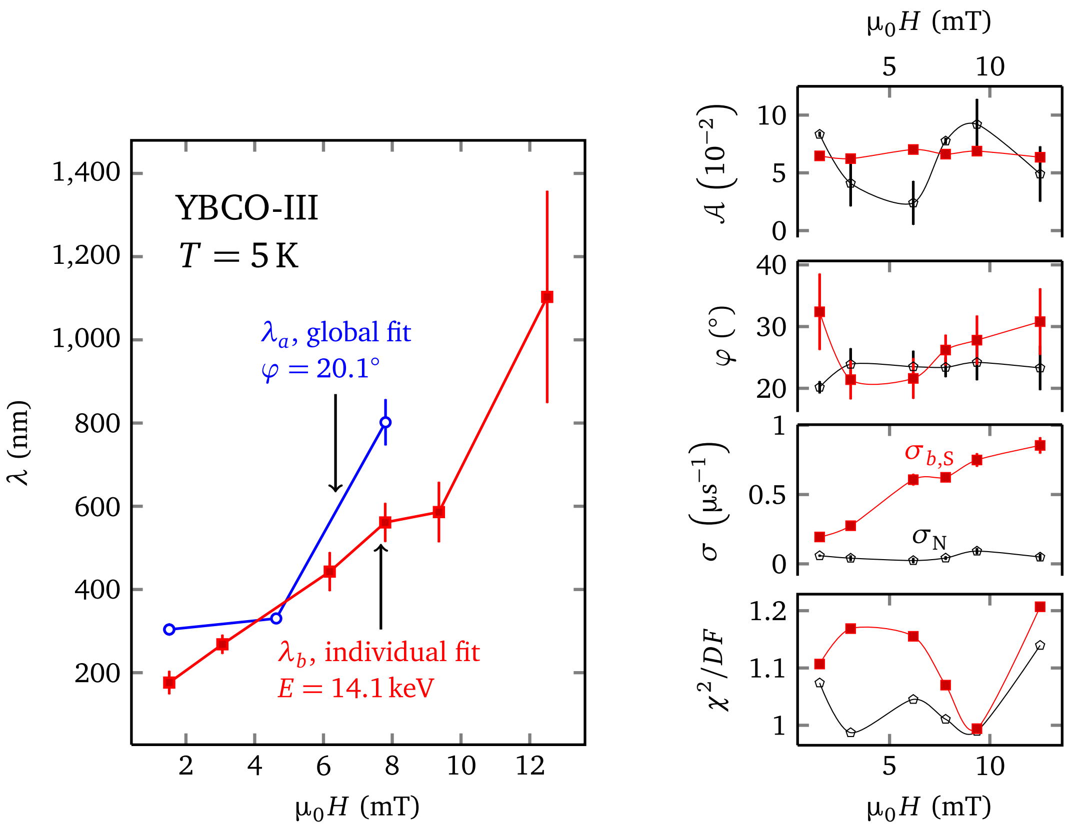

(a) **(b)**

Figure 4.24: (a) Single measurements of effective penetration depths in various external magnetic fields are shown here. The almost linear rise in λ_b with magnetic field stresses that lower external field must be used and also be made sure that the samples are indeed in the Meissner state. (b) The asymmetry in the normal states seem to show some unusual variance (should be constant) with respect to $\mu_0 H$. On the other hand, these single measurements may not accurate reflect the phase from global fits. The rise of σ with muon energy is due to the expelled flux ($\propto \mu_0 H$) from the neighboring crystals.

of the two techniques allows a precise determination of the T dependence of the magnetic penetration depth, which depends on the symmetry of the superconducting gap.

In the current study we measure the field profile directly on a freshly cleaved surface of $Ba(Co_{0.074}Fe_{0.926})_2As_2$ using the modified London model as described in the section 4.1.1. The single crystal of optimally-doped $Ba(Co_{0.074}Fe_{0.926})_2As_2$ was grown using a self-flux method [163]. The crystal was approximately square-shaped with dimensions 5.6 mm × 4.5 mm × 0.3 mm and exhibited a sharp transition at $T_c = 21.7$ K as measured by SQUID magnetometry. The crystal was cleaved to a thickness of about 0.3 mm under flowing N_2 gas just prior to loading it into the ultra-high-vacuum sample chamber.

Figure 4.25 shows typical μSR precession signals obtained with a small transverse

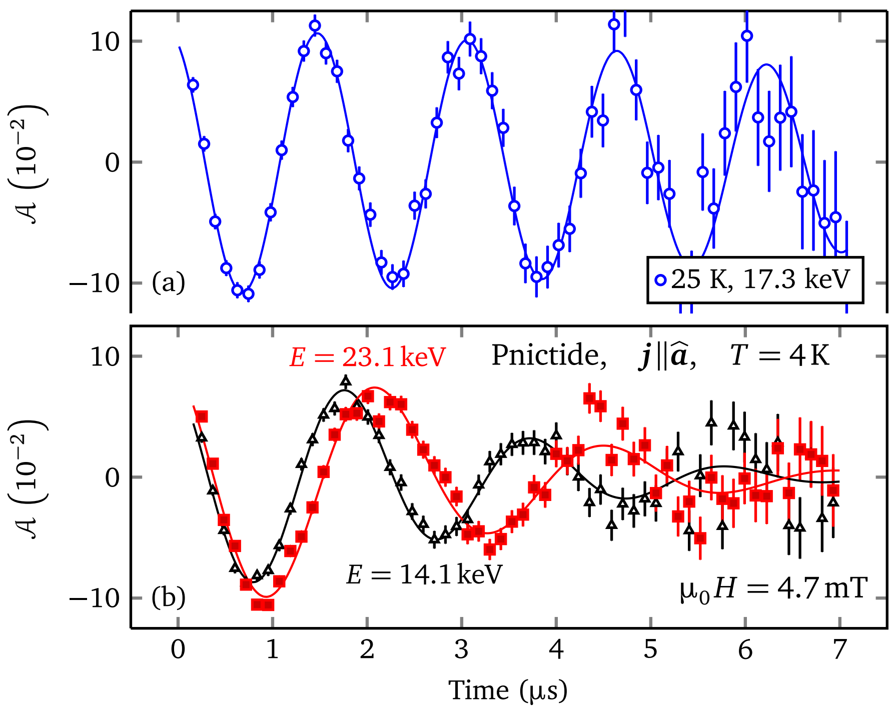

Figure 4.25: Muon precession signals in $Ba(Co_xFe_{1-x})_2As_2$ in an applied field of $\mu_0 H = 4.7$ mT. (a) In the normal state at $T = 25$ K. (b) In the superconducting state at $T = 4$ K with $E = 14$ keV and $E = 23$ keV.

magnetic field applied parallel to the *ab* face of the crystal. The top panel shows the precession signal in the normal state where the mean internal field is equal to the applied field obtained via fitting the spectrum to a Gaussian. The normal state at $\mu_0 H = 4.7\,\mathrm{mT}$ yields a σ of $0.12\,\mu\mathrm{s}^{-1}$. Signals taken below T_c are shown in the bottom panel. All the measurements in the Meissner state were made in **zero field cooled** method as detailed earlier. The reduction of precession frequency, for a higher muon implantation energy, is clearly visible comparing the two spectras (▵ and ■) in the figure 4.25. The asymmetry, phase and broadening parameter are shown in the figure 4.26. The asymmetry shows the usual energy dependent behavior. The $\langle\sigma\rangle$ in the Meissner state of $\mu_0 H = 4.7\,\mathrm{mT}$ is slightly higher ($0.28(1)\,\mu\mathrm{s}^{-1}$) than that ($0.21(1)\,\mu\mathrm{s}^{-1}$) corresponding to the $\mu_0 H = 2.5\,\mathrm{mT}$. The increase of σ with external field were attributed to **bulk magnetization effects**, where flux expelled from neighboring crystals broaden the effective field, in all three dopings of mosaic $YBa_2Cu_3O_{6+x}$. The bulk magnetization effect is linearly dependent to the external field. However, the present Pnictide sample is a single crystal and the average additional (not accounted for by the stopping distribution $\rho(z)$) broadening $\langle\sigma\rangle$ increases by $\sim 25\,\%$ with the approximate doubling of $\mu_0 H$. Also may be noted from the figure 4.26, that σ does not increase sharply close to the surface as has been seen previously in the two YBCO mosaics shown in the figures 4.11 and 4.19. This suggests that there is no vortices close to the surface and yet there is a suppression of superfluid density $\sim 15\,\text{nm}$, close to the sample surface, as may be seen from the curvatures of the global fits in the figure 4.27.

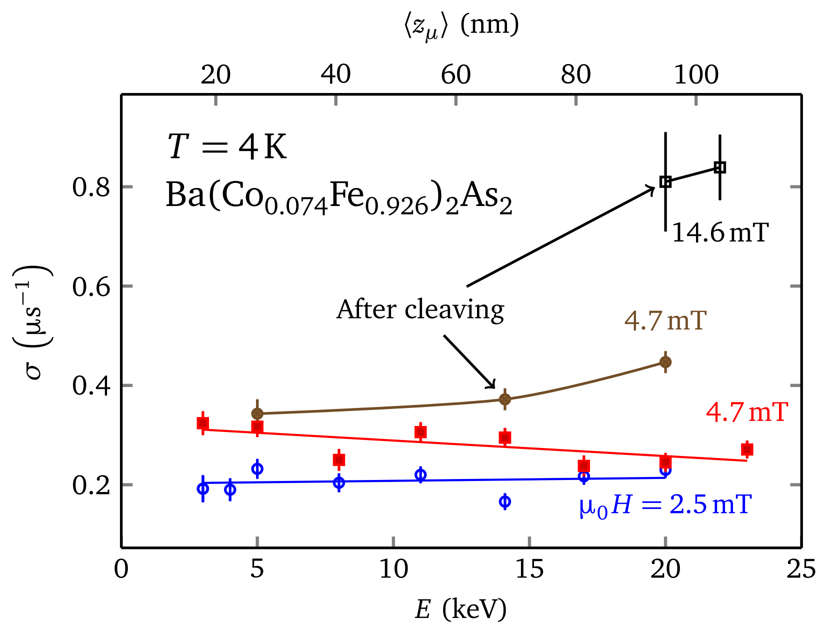

Figure 4.26: Broadening parameter (σ) in $Ba(Co_xFe_{1-x})_2As_2$ in external applied fields of $\mu_0 H = 2.5$ mT and 4.7 mT. The solid lines are guides to the eye.

Figure 4.27 shows the average local field $\langle B \rangle$ as a function of the beam energy at $T = 4$ K. The data are consistent with an exponential decrease as a function of increasing depth or implantation energy, as expected from a London model. Fit are $\lambda(T = 4\text{ K}) = 251.7(19)\,\text{nm}$ and $d = 14.5(9)\,\text{nm}$ where the uncertainties are purely statistical. There is also a 3% systematic uncertainty in λ due to uncertainties in the muon stopping distribution. Similar results were obtained at a magnetic field of 2.5 mT, where $\lambda = 252.2(45)\,\text{nm}$, indicating there is little field dependence in λ, which is also reflected in the $\langle B \rangle$ in the figure 4.27b. Results of analysis done on two phase (**independent and shared**) models are shown in the table 4.4. Notice that the average of phases from **individual phase model** is within $\sim 1°$, while **shared phase model** yields a $\sim 3°$. Yet with all the model dependence of A_0, σ and φ, there is only $\sim 2\,\text{nm}$ difference in the measured λ in the external fields of 2.5 mT and 4.7 mT. This suggests the robustness of our method in obtaining the absolute London penetration depth in Pnictide.

The temperature dependence of λ measured with LE-μSR (■) and with μW (——), MFM (○) and TDR (——) are shown in the figure 4.29. The data points were obtained with a single energy of 21.3 keV with d fixed to the value determined from the global fit at $T = 4$ K (see figure 4.27). Microwave resonance measurements of $\Delta\lambda$ were made on a piece of the

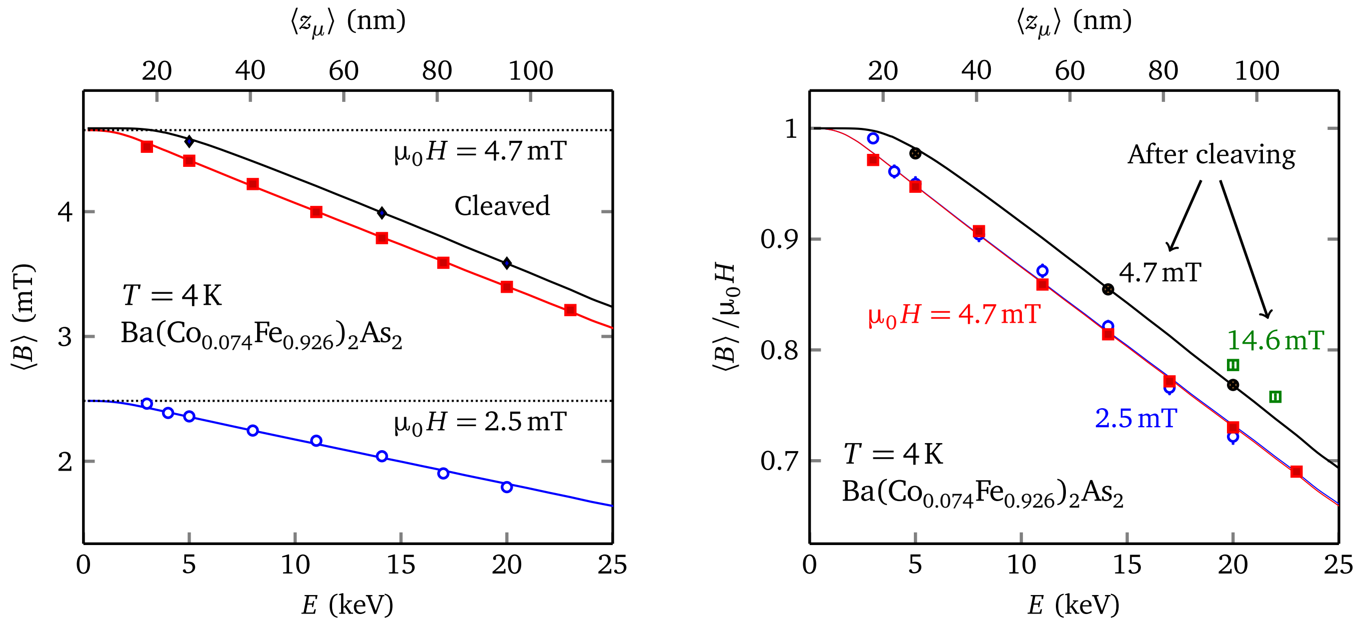

(a) **(b)**

Figure 4.27: The average magnetic field versus the muon energy at $T = 4$ K with a $\mu_0 H = 2.5$ mT applied field. The dotted line indicate the applied field and the solid line indicates a fit to (2.15).

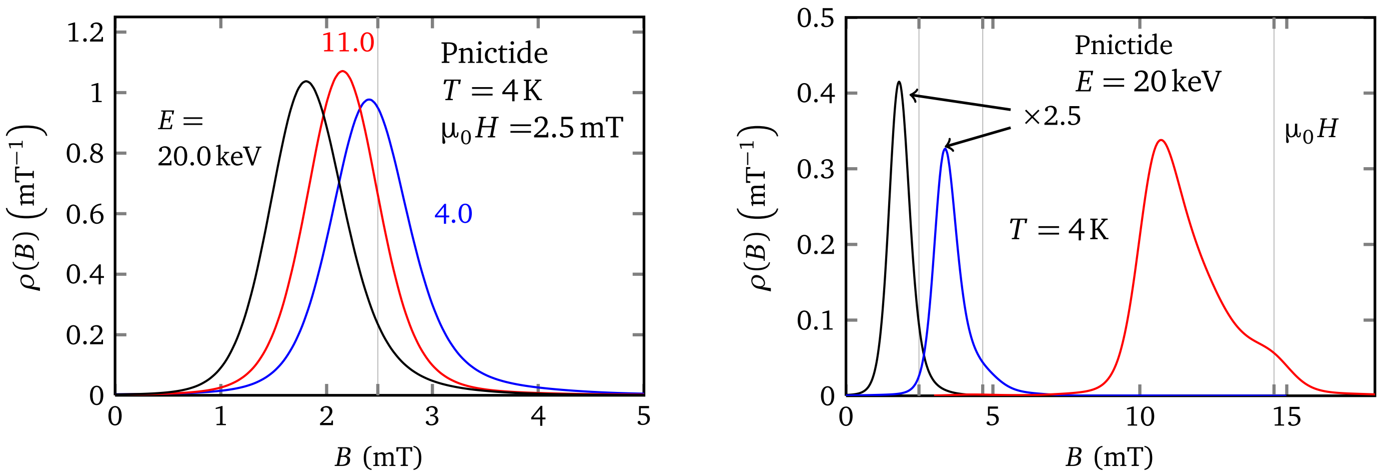

(a) **(b)**

Figure 4.28: Magnetic field distribution as seen by muons at various implantation energies and at $T = 5\,\mathrm{K}$ in an external applied magnetic field $(\mu_0 H)$ of 2.5 mT and 4.7 mT, applied parallel to the ab plane.

same crystal, which was cleaved on both sides. The piece of $Ba(Co_{0.074}Fe_{0.926})_2As_2$ was mounted on a temperature-controlled sapphire plate, and a 942 MHz loop-gap resonator, described in detail elsewhere[92], was used to obtain $\Delta\lambda$. It is clear the two methods are

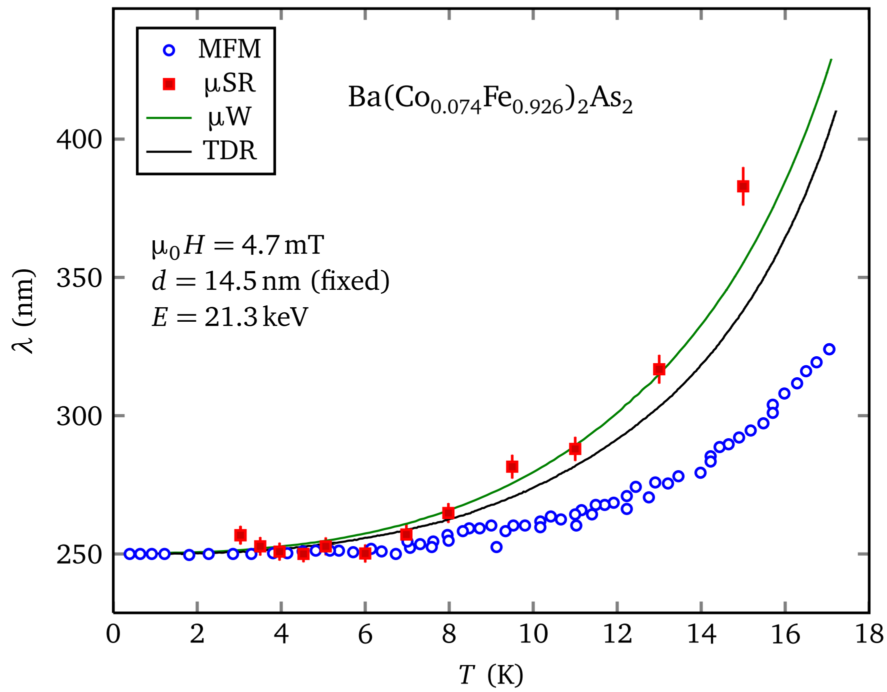

Figure 4.29: The temperature dependence of λ plotted versus $t = T/T_c$. The red squares (■) are measurements of the absolute value of λ from LE-μSR whereas the green line (—) are from microwave cavity perturbation on a piece of the same crystal shifted to overlap with the LE-μSR at low temperature. For comparison, we also show recent TDR (—) and MFM (○) results for $\Delta\lambda$, all shifted to agree at $T = 0$.

in excellent agreement below 13 K. One can use the microwave data to extrapolate the 4 K μSR measurement to obtain $\lambda(0) = 250.2(2.6)$nm. Above 13 K there is some difference between the two methods which we attribute to a small amount of flux penetration in the μSR experiment as one approaches T_c and the applied magnetic field of 4.67 mT exceeds H_{c1}. Note the temperature dependence of λ at low temperatures is similar to recent TDR results [164] on a thin sample but considerably weaker than previous studies on thicker crystals [165]. This suggests early studies may have been affected by an anomalous temperature-dependent field penetration from the c-axis edges. It is interesting to note that all of these results are stronger than found by MFM also shown in figure 4.29 [166]. One difference is that the present measurements, as well as previous TDR results, measure an average over the surface whereas MFM is a point-like probe. Such differences between methods and crystals indicate there are considerable variations in the spectrum of low energy excitations depending on doping and/or surface quality. Combination of μW and LE-μSR reduces allows one to determine the superfluid density and its variation as a function of temperature with a high confidence level. The temperature dependence of the superfluid density normalized to zero temperature is shown in the figure 4.30. Indeed, a similar quality of fit for low temperatures, which also fits the whole T range, can be obtained using a phenomenological two-gap s-wave model ("α model")[167], where

$$\rho = 1 - x\frac{\delta n_s(\Delta_S(T),T)}{n_s(0)} - (1-x)\frac{\delta n_s(\Delta_L(T),T)}{n_s(0)} \tag{4.10}$$

and,

$$\begin{aligned}\frac{\delta n_s(\Delta_i(T),T)}{n_s(0)} &= \frac{2}{k_B T}\int_0^\infty f(\varepsilon,\Delta_i(T),T) \\ &\quad\times [1 - f(\varepsilon,\Delta_i(T),T)]d\varepsilon\end{aligned} \tag{4.11}$$

$$\Delta_{L,S}(T) = \Delta_{L,S}(0)\tanh\left(\frac{\pi k_B T_c}{\Delta_{L,S}(0)}\sqrt{a_{L,S}\left(\frac{T_c}{T} - 1\right)}\right). \tag{4.12}$$

Here, the subscript $i = L$ denotes the larger gap which dominates at $T \sim T_\mathrm{c}$ where the other gap $i = S$ dominates at lower temperatures. $f(\varepsilon,\Delta_i(T),T)$ is the Fermi-Dirac distribution at energy ε and gap Δ. The free parameter $a_\mathrm{L,S}$ describes phenomenologically the shape of the gap, e.g. $a_\mathrm{L,S} \equiv 1$ in the BCS limit; for the small gap we define $a_S = 1$[168] and obtain $a_L = 0.83(3)$. We find the large gap $2\Delta_\mathrm{0,L}/k_B T_\mathrm{c} = 3.46(0.10)$ is close to the BCS weak-coupling limit whereas the small gap $2\Delta_{0,S}/k_B T_c = 1.20(7)$ is much less. These parameters are also close to those derived from vortex-state μSR measurements [168]. This is somewhat surprising given the high degree of vortex lattice disorder and the field induced magnetism[169]. The data were also fit to a self-consistent two-gap model which takes into account the interaction between bands ("γ model")[170]. The quality of the fit is similar to the phenomenological two-gap model over the full temperature range and the fitted gap parameters are about 10% larger. The data fit well to a power law form $\lambda^2(0)/\lambda^2(T) \approx 1 - \alpha(T/T_\mathrm{c})^n$ and are consistent with the superfluid density obtained directly from LE-μSR. A fit from base temperature to 12 K yields $n = 2.51(2)$ and $\alpha = 1.39(3)$ K and is only weakly dependent of the fitting range up to 11 K.

In conclusion, we have investigated the magnetic field penetration in the Meissner state of freshly-cleaved $Ba(Co_{0.074}Fe_{0.926})_2As_2$ using both LE-μSR and microwave cavity perturbation. The absolute value of λ extrapolated to $T = 0$ is 250(8) nm, where most of this uncertainty originates from the muon stopping distribution. There is no evidence of sharp rise in field broadening close to the sample surface. Also weaker field dependence of σ indicates a different origin other than bulk magnetization effect. A two-gap s-wave

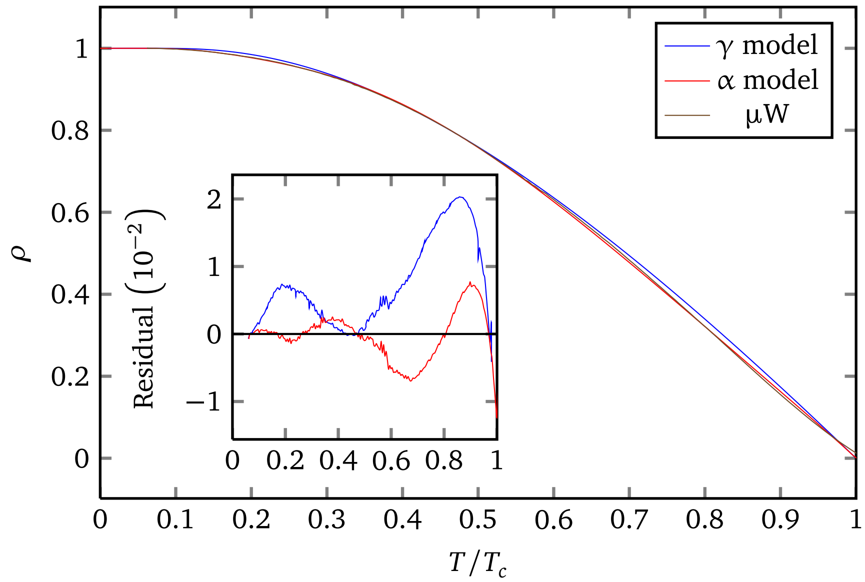

Figure 4.30: The temperature dependence of ρ plotted versus $t = T/T_c$. Solid black (dotted blue) line is a fit to the $\alpha(\gamma)$ model. The dashed curve is the fit to a power law. The inset shows the residuals at low temperature.

Table 4.4: Pnictide Two Fields

	4.7 mT			2.5 mT		
State	λ (nm)	$\varphi(°)$	χ^2/DF	λ (nm)	$\varphi(°)$	χ^2/DF
Normal	–	25.5(18)	0.932	–	21.4(17)	0.972
Superconducting	252.8(19)	30.9(12)[a]	1.118	254.5(41)	27.6(7)[a]	1.030
	251.7(19)	28.3(6)[b]	1.052	252.2(45)	27.8(5)[b]	1.029
Superconducting, cleaved	254.4(52)	27.9(9)[a]	1.198			
	253.9(51)	27.5(2)[b]	1.178			

[a] Global phase from **shared phase model** analysis.
[b] Average of energy specific phases from **individual phase model** analysis.

model and a weak power law model describes the temperature dependence of the superfluid density equally well. The latter model is characteristic of any non s wave gap. There is broad agreement between methods at least at this one Co concentration, except for MFM which probes $\Delta\lambda$ on much smaller length scale.

4.3 Summary Of Results

Table 4.5 shows the summary of London penetration depths measurements for three oxygen dopings of $YBa_2Cu_3O_{6+x}$ and on $Ba(Co_{0.074}Fe_{0.926})_2As_2$. The first number is the measured $\lambda_{a,b}$ extrapolated to $T = 0$ K. The first error is the statistical uncertainty at the temperature $\lambda_{a,b}$ are measured and the second error is the systematic uncertainty. For comparison, $\lambda_{a,b}$

values from other measurements are also mentioned In $YBa_2Cu_3O_{6.92}$, "individual phase" and "shared phase" models yield $\lambda_{a,b}$ within a nm of each other and anisotropy is the same for both models. This suggests that there is little (φ) model dependence and accurate values of $\lambda_{a,b}$ can be obtained by LE-μSR method. The $\lambda_{a,b}$ obtained here is in good agreement with bulk μSR measurement in vortex state. It may be noted that conventional μSR is very different type of measurement. The $\lambda_{a,b}$ in $YBa_2Cu_3O_{6.92}$ obtained here is shorter than that obtained in film. The difference is understandable considering the measurement in film was done at 20 K and the T_c of the film (87.5 K) is less than in crystals possibly indicating a different doping level than in crystals.

Row two of table 4.5 represent our results of $\lambda_{a,b}$ in Ortho-I $YBa_2Cu_3O_{6.998}$, measured at 5 K & 4.7 mT, extrapolated to 0 K by the method described above. In our analysis of "invididual phase" model, slightly different $\lambda_{a,b}$ and anisotropy are obtained. However, the measurement of λ is dependent on our ability to determine phase (φ) and frequency (ω) at the same time, which is difficult in lower fields. The lower external field has one significant advantage of reducing the chance of vortex entrance. It may be noted that in $YBa_2Cu_3O_{6.998}$, both 4.7 mT & 9.5 mT measurements were done and the λ_b is about the same in "shared phase" model for 9.5 mT. However, λ at higher external field may have some contribution from vortices and "individual phase" model hase significantly lower χ^2/DF. Note that, there is very close agreement between our result and ESR Gd-doped Ortho-I $YBa_2Cu_3O_{6.95}$.

Row three of table 4.5 represent our results of $\lambda_{a,b}$ in $YBa_2Cu_3O_{6.52}$, measured at 5 K & 1.5 mT, extrapolated to 0 K. $\lambda_{a,b}$'s were measured in 1.5 mT, 4.7 mT & 7.8 mT, however, there are clear evindences that all external fields excepth the lowest 1.5 mT introduced vortices. In 1.5 mT external field, a unique determination of phase was made by reversing the field, essentially doubling the range of muon polarization's oscillation time. Determination of phase is crucial specially at low field as frequency is low and very few full oscillations are observed in muon polarization. It is also interesting that the low temperature linear dependence of λ in $YBa_2Cu_3O_{6.52}$ is an order of magnitude higher than those found in other two oxygen dopings. Note that $\lambda_{a,b}$ in LE-μSR is significantly longer than that measured in ESR on Gd-doped $YBa_2Cu_3O_{6.52}$. This is surprising considering the other two oxygen dopings have produced very similar results.

On eleventh row (just below the horizontal line) in table 4.5, our measurement of λ_{ab}, extrapolated to 0 K is shown. Measurements were done in external field of 2.5 mT 4.7 mT. The λ_{ab} obtained in for both external field in "shared phase" and "individual phase" models were close to each other within $\sim 4nm$ i.e, introducing $\sim 2\%$ systematic uncertainty. A two-gap s-wave model describes the temperature dependence of the superfluid density but an equally good fit at low temperatures can be obtained with a weak power-law behavior characteristic of point nodes in the gap function. There is broad agreement between methods at least at this one Co concentration, except for MFM which probes $\Delta\lambda$ on much smaller length scale. For comparison some results from other methods, especially MFM are also shown. Among the MFM results, one of the results with the exact same Co-doping as ours, yield the same λ, however with a much larger uncertainty.

Figure 4.31 shows the critical temperature vs effective superfluid density $1/(\lambda_a\lambda_b)^{-1}$. A linear relationship between the two quantities was first suggested by Uemura *et al*. LE-μSR results significantly differ from a linear relationship. The relationship seems to be sublinear dependence of T_c on λ_{ab}^2 since, for large λ_{ab}, superfluid density will be proportionately smaller and T_c will also be smaller. The linear relationship has been widely regarded as an evidence of order parameter's phase fluctuation is the parameter responsible for setting T_c. The probable sublinear relationship of T_c on λ_{ab}^2 is an indication of other mechanisms being influential in determining T_c. One of the interesting aspect from figure 4.31 is that optimally doped cuprate & Co-doped pnictide almost falls on a line. Measurements on a range of dopings will be needed to determine the exact relationship of T_c on λ_{ab}^2.

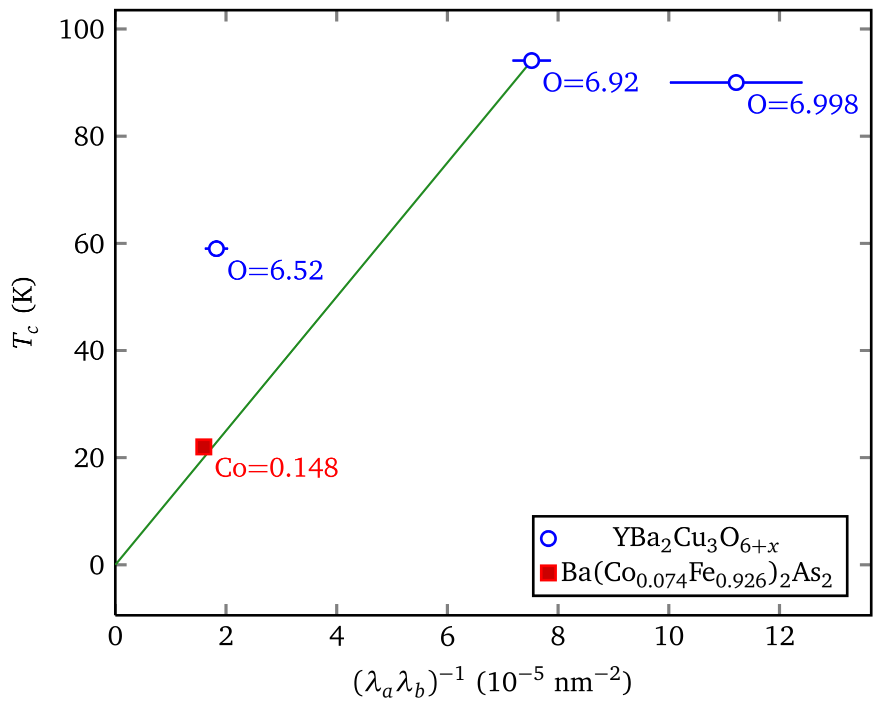

Figure 4.31: Tc vs Lambda-ab.

4.4 Discussion On "Deadlayer"

As mentioned in earlier section, a superconductor carries no bulk magnetic field and applied external field decays exponentially inside the sample as it penetrates the surface, according to the London equations. However, as will be shown in a later chapter that, very close to surface, there is a distance over which magnetic field essentially remains constant, an effective dead layer. One possible explanation is surface roughness: small perturbations

Table 4.5: Measurements of the absolute value of the magnetic penetration depth ($\lambda_{a,b}$) in $YBa_2Cu_3O_{6.52}$, $YBa_2Cu_3O_{6.92}$ and $YBa_2Cu_3O_{6.998}$. Average magnetic penetration depth $\lambda_{ab} = \sqrt{\lambda_a \lambda_b}$. Vortex state measurements are quoted without systematic errors.

λ_a (nm)	λ_b (nm)	λ_{ab} (nm)	λ_a/λ_b	Comment
$125.6(17) \pm 3$	$105.5(11) \pm 3$	$115.1(10) \pm 3$	1.19(1)	$YBa_2Cu_3O_{6.92}$ [a]
$105.0(39) \pm 3$	$82.0(33) \pm 3$	$92.8(26) \pm 3$	1.28(2)	$YBa_2Cu_3O_{6.998}$ [a]
$261.9(141) \pm 3$	$201.5(104) \pm 3$	$229.7(86) \pm 3$	1.30(2)	$YBa_2Cu_3O_{6.52}$ [a]
		118.0(4)		μSR in vortex state[b] [121]
		146(3)		LE-μSR in thin film at 20 K [162]
160	100	126.5	1.6	IR reflectivity at 10 K [109]
103(8)	80(5)	91(7)	1.29(7)	ESR on $YBa_2Cu_3O_{6.995}$ [171]
202(22)	140(28)	168(19)	1.4(3)	ESR on $YBa_2Cu_3O_{6.52}$ [171]
		150(10)	1.16(2)	μSR at 10 K [172]
		138(5)	1.18(2)	SANS at 10 K [173]
$250.0(26) \pm 5$	$250.0(26) \pm 5$	$250.0(26) \pm 5$	-	$Ba(Co_{0.074}Fe_{0.926})_2As_2$ [a]
		325(50)	-	MFM [166] in $Ba(Co_{0.05}Fe_{0.95})_2As_2$
		190(10)	-	Estimated for a range of dopings in $BaCo_xFe_{2-x}As_2$ [174]
		250(36)	-	MFM [175] on $Ba(Co_{0.074}Fe_{0.926})_2As_2$

[a] This work
[b] Conventional μSR

from a perfect flat geometry. A set of mathematical analysis have been done [176] assuming uneven surface geometry

$$z = \epsilon \cos(\omega_x x)\cos(\omega_y y). \tag{4.13}$$

In these set of analysis, a length of 1 corresponds to a distance of λ in physical units; a frequency ω corresponds to a physical frequency $\tilde{\omega} = \frac{2\pi}{\omega\lambda}$; a field strength of 1 corresponds to the applied external field $|\mathbf{B}_{\text{applied}}|$; roughness amplitude ϵ is believed to be no bigger than (1/10) of λ. A definition of an effective dead layer δ, in dimensionless units, may be adopted as

$$\delta = \int_0^\infty |\mathbf{b}|_{\text{avg}}(s)ds - 1, \tag{4.14}$$

where $\mathbf{b}(s)$ is the depth dependent magnetic field & with the interpretation that for a true dead layer of size δ, the area under $|\mathbf{b}|_{\text{avg}}$ from $s = 0$ to ∞ is precisely $\delta + 1$.

Without loss of generality, sample surface may be modelled as sinusoidal, as more complicated surface may always be Fourier-transformed. For a surface like this, external magnetic field will also be sinusoidal, close to the surface, as depicted in figure 4.32(a).

With an asymptotic expansion of magnetic field $\mathbf{b}$ $\mathbf{b}_0 + \epsilon\mathbf{b}_1 + \epsilon^2\mathbf{b}_2 + \cdots$, where $\mathbf{b}_0$ is the known solution for a flat surface & $\mathbf{b}_i$'s are the i-th smaller components M. Lindstrom et al. [176] has found via linear analysis, that average magnetic field $|\mathbf{b}|_{\text{avg}}$ may differ from the London solution by as much as 1%.(figure 4.32). As may be noted from the figure the external field starts decaying before entering the sample, a contrasting scenario with the experimental observation of local fields is possible only inside the surface. Our results suggest that for surfaces with roughness amplitudes in the ballpark of $\lambda/10$ whose spatial frequencies aren't too high, the dead layer is no bigger than $\lambda/20$.

One way the supercurrent at the surface may be suppressed is via vortex penetration which can be facilitated by suppression of d-wave order, i.e a reduction of energy gap near twin or grain boundaries [177, 178]. Also, surface roughness has been attributed to as the cause of vortex neculeation at fields $H \leq H_{c1}$ [179]. Surface vortices have been observed in YBCO in fields as minute as 4G applied parallel to $a - b$ plane [180]. It may be speculated that full-strength external field near the vacuum-surface boundary may be a harbinger of vortices. Also vortex-vortex interaction may be an additional element in the apparent supercurrent suppression. Field inhomogeneities may result from local variations of current close to surface due to surface roughness and twin and grain boundaries [181]. Further experiments on atomically flat surfaces may help elucidate the origin of the reduction of supercurrent in the surface vicinity.

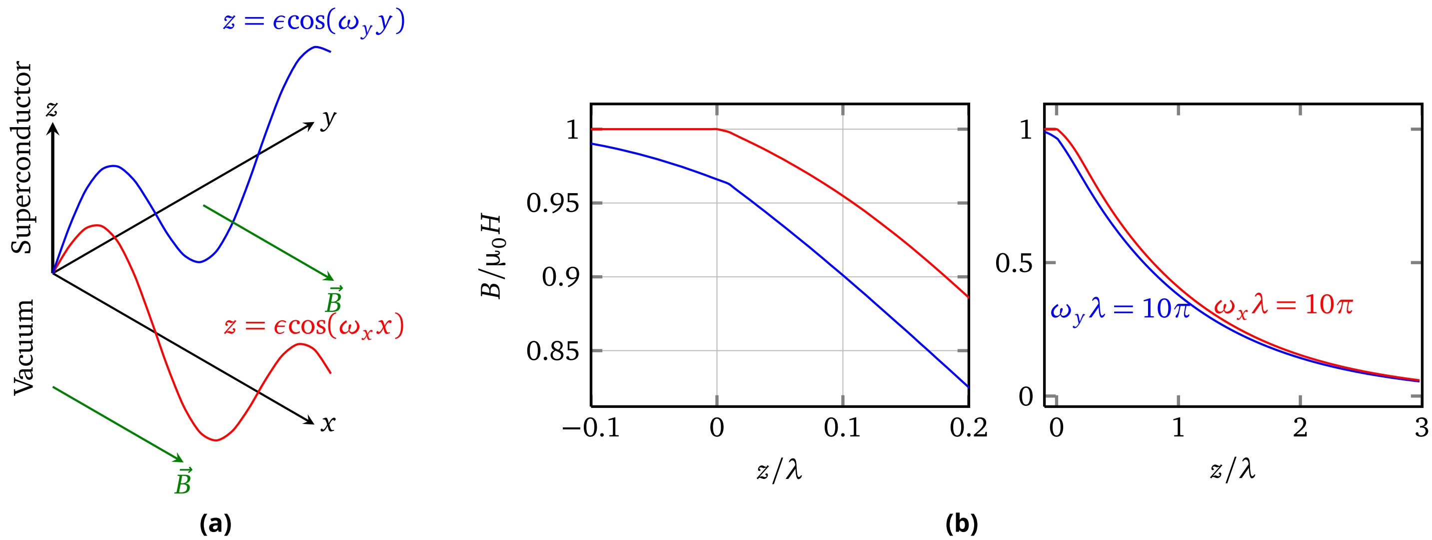

Figure 4.32: (a) A rough surface geometry may be modelled as sinusoidal as any complex surface structure can be Fourier-transformed. External field direction is taken to be along a axis of the crystal. (b) Simulated relative field as it enters the sample.

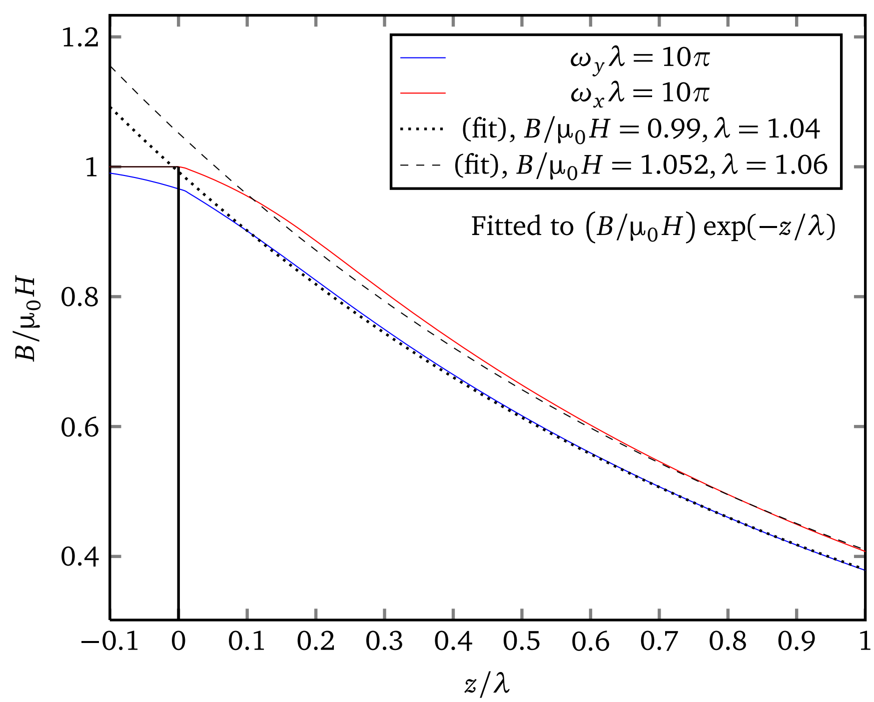

Figure 4.33: Simulated external field fitted to the London model function for the depth range 0 to 10λ. Only the region of 0-λ is shown.

5

Conclusions & Outlook

In this thesis, recent measurements of λ_{a_b} and the anisotropies$\left(\equiv \lambda_a/\lambda_b\right)$ have been done for three different oxygen ($x = 6.52, 6.92, 6.998$) dopings of $YBa_2Cu_3O_{6+x}$ and one on $Ba(Co_{0.07}Fe_{0.93})_2As_2$. The measured values of λ and the anisotropies are considerably different from that of literature, often found with bulk methods. An exponential decay of the magnetic field and corresponding supercurrent density $\backsim$ 100 nm inside the crystals. Small deviations from the London model are observed which indicate there is a suppression of the supercurrent density close to the surface. The measured (λ) values are also found to depart substantially from the widely reported Uemura relation $\left(T_c \propto 1/\lambda_a^2\right)$. Low energy μSR is a very sensitive depth-dependent probe close to the surface of the crystals. Using London model and simulated stopping profiles, one is able to extract a very precise measure of London penetration depth as a function of observable parameters such doping, temperature, impurity. The measured penetration depths slightly depend on the exact phase models used, as is the case with any model. However the uncertainties due to an exact determination of phase are included as systematic errors in the final results. In fields on the order of ~ 10 mT, measured London depths have little model dependence compared to lower fields such as 5 mT or 1.5 mT. This is easily understood as we note that there are fewer full oscillations in asymmetry spectrum for lower fields and phase & frequency ($\gamma_\mu B$) becomes correlated. However lower fields were required for one oxygen doping in $YBa_2Cu_3O_{6+x}$ due to vortex entrance at external fields $\backsim$ 4.6 mT. The measured $\lambda_{a,b}$ have been found in YBCO good agreement with ESR and conventional μSR, with the exception of considerable difference oxygen doping 6.52. Low temperature linear dependence of $\lambda_{a,b}$ have also been observed in all the oxygen dopings in $YBa_2Cu_3O_{6+x}$, which is an important signature for a d-wave superconducting gap. One important parameter, penetration depth anisotropy $\mathcal{R}$, is also determined for all the dopings of YBCO. The anisotropy, being the ratio of λ in both directions, are determined with more accuracy than the penetration depths.

Pnictide penetration depth is also in very good agreement with a recent MFM (with a larger error) determination of λ and is somewhere between the earlier estimates. The temperature dependence of the superfluid density is obtained by combining low energy μSR and microwave resonance and a weak power law behavior for the superfluid density is found at low temperature while a two-gap model fits the whole temperature range.

Bibliography

1 Kiefl, R. F., et al. Direct measurement of the London penetration depth in $YBa_2Cu_3O_{6.92}$ using low-energy μSR. Phys. Rev. B, **81**, 180502 (2010). ◇ Cited on page iii.

2 Ofer, O., et al. Absolute value and temperature dependence of the magnetic penetration depth in $Ba(Co_{0.074}Fe_{0.926})_2As_2$. Phys. Rev. B, **85**, 060506 (2012). ◇ Cited on page iii.

3 Onnes, H. K. Commun. Phys. Lab. Univ. Leiden, **120b,122b,124c** (1911). ◇ Cited on page 1.

4 Onnes, H. K. The resistance of pure mercury at helium temperatures. Comm. Leiden., **120 b** (1911). ◇ Cited on page 1.

5 Meissner, W. and Oschenfel, R. Naturwiss., **21** (1933). ◇ Cited on page 1.

6 London, F. and London, H. Proc. R. Soc. London, **A149** (1935). ◇ Cited on page 1.

7 Ginzburg, V. L. and Landau, L. D. On the Theory of superconductivity. Zh. Eksp. Teor. Fiz., **20**, 1064–1082 (1950). ◇ Cited on page 1.

8 Bardeen, J., Cooper, L. N., and Schrieffer, J. R. Theory of Superconductivity. Phys. Rev., **108**, 1175–1204 (1957). ◇ Cited on page 3.

9 Bardeen, J., Cooper, L. N., and Schrieffer, J. R. Microscopic Theory of Superconductivity. Phys. Rev., **106**, 162–164 (1957). ◇ Cited on page 3.

10 Cooper, L. N. Bound Electron Pairs in a Degenerate Fermi Gas. Phys. Rev., **104**, 1189–1190 (1956). ◇ Cited on pages 3 & 16.

11 Bednorz, J. G. and Müller, K. A. Possible high T_c superconductivity in the Ba-La-Cu-O system. Zeitschrift für Physik B Condensed Matter, **64**, 189–193 (1986). ◇ Cited on page 3.

12 Wu, M. K., Ashburn, J. R., Torng, C. J., Hor, P. H., Meng, R. L., Gao, L., Huang, Z. J., Wang, Y. Q., and Chu, C. W. Superconductivity at 93 K in a new mixed-phase Y-Ba-Cu-O compound system at ambient pressure. Phys. Rev. Lett., **58**, 908–910 (1987). ◇ Cited on page 3.

13 Elert, G. (2002), Highest critical temperature superconductor. [Online; accessed 5-February-2012]. ◇ Cited on page 4.

14 Blatter, G., Feigel'man, M. V., Geshkenbein, V. B., Larkin, A. I., and Vinokur, V. M. Vortices in high-temperature superconductors. Rev. Mod. Phys., **66**, 1125–1388 (1994). ◇ Cited on page 3.

15 Sachdev, S. and Zhang, S.-C. Tuning Order in Cuprate Superconductors. Science, **295**, 452–454 (2002). ◇ Cited on page 5.

16 Hill, R. W., Proust, C., Taillefer, L., Fournier, P., and Greene, R. L. Breakdown of Fermi-liquid theory in a copper-oxide superconductor. Nature, **414**, 711–715 (2001). ◇ Cited on page 6.

17 Capponi, J. J., Chaillout, C., Hewat, A. W., Lejay, P., Marezio, M., Nguyen, N., Raveau, B., Soubeyroux, J. L., Tholence, J. L., and Tournier, R. Structure of the 100 K Superconductor $YBa_2Cu_3O_7$ between (5 - 300) K by Neutron Powder Diffraction. EPL (Europhysics Letters), **3**, 1301 (1987). ◇ Cited on page 7.

18 Momma, K. and Izumi, F. *VESTA*: a three-dimensional visualization system for electronic and structural analysis. Journal of Applied Crystallography, **41**, 653–658 (2008). ◇ Cited on page 7.

19 Keren, A., Le, L. P., Luke, G. M., Sternlieb, B. J., Wu, W. D., Uemura, Y. J., Tajima, S., and Uchida, S. Muon-spin-rotation measurements in infinite-layer and infinite-chain cuprate antiferromagnets: $Ca_{0.86}Sr_{0.14}CuO_2$ and Sr_2CuO_3. Phys. Rev. B, **48**, 12926–12935 (1993). ◇ Cited on pages 6 & 13.

20 Tallon, J. L., Bernhard, C., Shaked, H., Hitterman, R. L., and Jorgensen, J. D. Generic superconducting phase behavior in high-T_c cuprates: T_c variation with hole concentration in $YBa_2Cu_3O_{7-\delta}$. Phys. Rev. B, **51**, 12911–12914 (1995). ◇ Cited on page 8.

21 Lanzara, A., et al. Evidence for ubiquitous strong electron-phonon coupling in high-temperature superconductors. Nature, **412**, 510–514 (2001). ◇ Cited on page 8.

22 Devereaux, T. P., Cuk, T., Shen, Z.-X., and Nagaosa, N. Anisotropic electron-phonon interaction in the cuprates. Phys. Rev. Lett., **93**, 117004 (2004). ◇ Cited on page 8.

23 Bohnen, K.-P., Heid, R., and Krauss, M. Phonon dispersion and electron-phonon interaction for $YBa_2Cu_3O_7$ from first-principles calculations. EPL (Europhysics Letters), **64**, 104 (2003). ◇ Cited on page 8.

24 Falter, C. and Hoffmann, G. A. Nonlocal electron-phonon coupling of ionic charge-fluctuation type and phonon anomalies in high-temperature superconductors. Phys. Rev. B, **64**, 054516 (2001). ◇ Cited on page 8.

25 Chung, J.-H., et al. In-plane anisotropy and temperature dependence of oxygen phonon modes in $YBa_2Cu_3O_{6.95}$. Phys. Rev. B, **67**, 014517 (2003). ◇ Cited on page 8.

26 Reznik, D., Pintschovius, L., Ito, M., Iikubo, S., Sato, M., Goka, H., Fujita, M., Yamada, K., Gu, G. D., and Tranquada, J. M. Electron-phonon coupling reflecting dynamic charge inhomogeneity in copper oxide superconductors. Nature, **440**, 1170–1173 (2006). ◇ Cited on page 8.

27 Giustino, F., Cohen, M. L., and Louie, S. G. Small phonon contribution to the photoemission kink in the copper oxide superconductors. Nature, **452**, 975–978 (2008). ◇ Cited on page 8.

28 Anderson, P. W. The Resonating Valence Bond State in La_2CuO_4 and Superconductivity. Science, **235**, 1196–1198 (1987). ◇ Cited on page 8.

29 Anderson, P. W. Resonating valence bonds: A new kind of insulator? Materials Research Bulletin, **8**, 153 – 160 (1973). ◇ Cited on page 9.

30 Anderson, P. W., Lee, P. A., Randeria, M., Rice, T. M., Trivedi, N., and Zhang, F. C. The physics behind high-temperature superconducting cuprates: the 'plain vanilla' version of RVB. Journal of Physics: Condensed Matter, **16**, R755 (2004). ◇ Cited on page 9.

31 Baskaran, G., Zou, Z., and Anderson, P. W. The resonating valence bond state and high-T_c superconductivity – A mean field theory. Solid State Communications, **63**, 973 – 976 (1987). ◇ Cited on page 9.

32 Vaknin, D., Sinha, S. K., Moncton, D. E., Johnston, D. C., Newsam, J. M., Safinya, C. R., and King, H. E. Antiferromagnetism in La_2CuO_{4-y}. Phys. Rev. Lett., **58**, 2802–2805 (1987). ◇ Cited on pages 9 & 12.

33 Tranquada, J. M., et al. Neutron-Diffraction Determination of Antiferromagnetic Structure of Cu Ions in $YBa_2Cu_3O_{6+x}$ with $x = 0.0$ and 0.15. Phys. Rev. Lett., **60**, 156–159 (1988). ◇ Cited on page 9.

34 Moudden, A. H., Shirane, G., Tranquada, J. M., Birgeneau, R. J., Endoh, Y., Yamada, K., Hidaka, Y., and Murakami, T. Antiferromagnetic ordering of Cu ions in $NdBa_2Cu_3O_{6.1}$. Phys. Rev. B, **38**, 8720–8723 (1988). ◇ Cited on pages 9 & 13.

35 Shirane, G., Endoh, Y., Birgeneau, R. J., Kastner, M. A., Hidaka, Y., Oda, M., Suzuki, M., and Murakami, T. Two-dimensional antiferromagnetic quantum spin-fluid state in La_2CuO_4. Phys. Rev. Lett., **59**, 1613–1616 (1987). ◇ Cited on pages 9 & 13.

36 Endoh, Y., et al. Static and dynamic spin correlations in pure and doped La_2CuO_4. Phys. Rev. B, **37**, 7443–7453 (1988). ◇ Cited on page 9.

37 Niedermayer, C., Bernhard, C., Blasius, T., Golnik, A., Moodenbaugh, A., and Budnick, J. I. Common Phase Diagram for Antiferromagnetism in $La_{2-x}Sr_xCuO_4$ and $Y_{1-x}Ca_xBa_2Cu_3O_6$ as Seen by Muon Spin Rotation. Phys. Rev. Lett., **80**, 3843–3846 (1998). ◇ Cited on page 9.

38 Hussey, N. E. Low-energy quasiparticles in high-T_c cuprates. Advances in Physics, **51**, 1685–1771 (2002). ◇ Cited on page 9.

39 Hussey, N. E., Abdel-Jawad, M., Carrington, A., Mackenzie, A. P., and Balicas, L. A coherent three-dimensional Fermi surface in a high-transition-temperature superconductor. Nature, **425**, 814–817 (2003). ◇ Cited on page 9.

40 Yamaji, K. On the Angle Dependence of the Magnetoresistance in Quasi-Two-Dimensional Organic Superconductors. Journal of the Physical Society of Japan, **58**, 1520–1523 (1989). ◇ Cited on page 9.

41 Tanaka, K., et al. Distinct Fermi-Momentum-Dependent Energy Gaps in Deeply Underdoped Bi2212. Science, **314**, 1910–1913 (2006). ◇ Cited on pages 9 & 10.

42 Audouard, A., Jaudet, C., Vignolles, D., Liang, R., Bonn, D. A., Hardy, W. N., Taillefer, L., and Proust, C. Multiple Quantum Oscillations in the de Haas-van Alphen Spectra of the Underdoped High-Temperature Superconductor $YBa_2Cu_3O_{6.5}$. Phys. Rev. Lett., **103**, 157003 (2009). ◇ Cited on page 10.

43 Ding, H., Yokoya, T., Campuzano, J. C., Takahashi, T., Randeria, M., Norman, M. R., Mochiku, T., Kadowaki, K., and Giapintzakis, J. Spectroscopic evidence for a pseudogap in the normal state of underdoped high-T_c superconductors. Nature, **382**, 51–54 (1996). ◇ Cited on page 10.

44 Daou, R., et al. Broken rotational symmetry in the pseudogap phase of a high-T_c superconductor. Nature, **463**, 519–522 (2010). ◇ Cited on page 10.

45 Timusk, T. and Statt, B. The pseudogap in high-temperature superconductors: an experimental survey. Reports on Progress in Physics, **62**, 61 (1999). ◇ Cited on page 10.

46 Loeser, A. G., Shen, Z.-X., Dessau, D. S., Marshall, D. S., Park, C. H., Fournier, P., and Kapitulnik, A. Excitation Gap in the Normal State of Underdoped $Bi_2Sr_2CaCu_2O_{8+\delta}$. Science, **273**, 325–329 (1996). ◇ Cited on page 10.

47 Laughlin, R. B. PERSPECTIVES A critique of two metals. Advances in Physics, **47**, 943 – 958 (1998). ◇ Cited on page 10.

48 Sachdev, S. Quantum Criticality: Competing Ground States in Low Dimensions. Science, **288**, 475–480 (2000). ◇ Cited on page 10.

49 Tallon, J. and Loram, J. The doping dependence of T^* - what is the real high-T_c phase diagram? PHYSICA C, **349**, 53–68 (2001). ◇ Cited on page 10.

50 Li, Y., Baledent, V., Barisic, N., Cho, Y., Fauque, B., Sidis, Y., Yu, G., Zhao, X., Bourges, P., and Greven, M. Unusual magnetic order in the pseudogap region of the superconductor $HgBa_2CuO_{4+\delta}$. Nature, **455**, 372–375 (2008). ◇ Cited on page 10.

51 Varma, C. M. Non-Fermi-liquid states and pairing instability of a general model of copper oxide metals . Phys. Rev. B, **55**, 14554–14580 (1997). ◇ Cited on page 10.

52 Varma, C. M. Pseudogap Phase and the Quantum-Critical Point in Copper-Oxide Metals. Phys. Rev. Lett., **83**, 3538–3541 (1999). ◇ Cited on page 10.

53 Gurvitch, M. and Fiory, A. T. Resistivity of $La_{1.825}Sr_{0.175}CuO_4$ and $YBa_2Cu_3O_7$ to 1100 K: Absence of saturation and its implications. Phys. Rev. Lett., **59**, 1337–1340 (1987). ◇ Cited on page 10.

54 Thomas, G. A., Orenstein, J., Rapkine, D. H., Capizzi, M., Millis, A. J., Bhatt, R. N., Schneemeyer, L. F., and Waszczak, J. V. $Ba_2YCu_3O_{7-\delta}$: Electrodynamics of Crystals with High Reflectivity. Phys. Rev. Lett., **61**, 1313–1316 (1988). ◇ Cited on page 10.

55 Gurvitch, M., Valles, J. M., Cucolo, A. M., Dynes, R. C., Garno, J. P., Schneemeyer, L. F., and Waszczak, J. V. Reproducible tunneling data on chemically etched single crystals of $YBa_2Cu_3O_7$. Phys. Rev. Lett., **63**, 1008–1011 (1989). ◇ Cited on page 10.

56 Anderson, P. W. The 'strange metal' is a projected Fermi liquid with edge singularities. Nat Phys, **2**, 626–630 (2006). ◇ Cited on page 10.

57 Varma, C. M., Littlewood, P. B., Schmitt-Rink, S., Abrahams, E., and Ruckenstein, A. E. Phenomenology of the normal state of Cu-O high-temperature superconductors. Phys. Rev. Lett., **63**, 1996–1999 (1989). ◇ Cited on page 10.

58 Gough, C. E., Colclough, M. S., Forgan, E. M., Jordan, R. G., Keene, M., Muirhead, C. M., Rae, A. I. M., Thomas, N., Abell, J. S., and Sutton, S. Flux quantization in a high-T_c superconductor. Nature, **326**, 855–855 (1987). ◇ Cited on page 10.

59 Tsuei, C. C., Kirtley, J. R., Chi, C. C., Yu-Jahnes, L. S., Gupta, A., Shaw, T., Sun, J. Z., and Ketchen, M. B. Pairing Symmetry and Flux Quantization in a Tricrystal Superconducting Ring of $YBa_2Cu_3O_{7-\delta}$. Phys. Rev. Lett., **73**, 593–596 (1994). ◇ Cited on page 10.

60 Gammel, P. L., Bishop, D. J., Dolan, G. J., Kwo, J. R., Murray, C. A., Schneemeyer, L. F., and Waszczak, J. V. Observation of Hexagonally Correlated Flux Quanta In $YBa_2Cu_3O_7$. Phys. Rev. Lett., **59**, 2592–2595 (1987). ◇ Cited on page 10.

61 Ren, Z. A., Yang, J., Lu, W., Yi, W., Che, G. C., Dong, X. L., Sun, L. L., and Zhao, Z. X. Superconductivity at 52 K in iron based F doped layered quaternary compound $Pr[O_{1-x}F_x]FeAs$. Materials Research Innovations, **12**, 105–106 (2008). ◇ Cited on page 10.

62 Chen, G. F., Li, Z., Wu, D., Li, G., Hu, W. Z., Dong, J., Zheng, P., Luo, J. L., and Wang, N. L. Superconductivity at 41 K and Its Competition with Spin-Density-Wave Instability in Layered $CeO_{1-x}F_xFeAs$. Phys. Rev. Lett., **100**, 247002 (2008). ◇ Cited on page 10.

63 Chen, X. H., Wu, T., Wu, G., Liu, R. H., Chen, H., and Fang, D. F. Superconductivity at 43 K in $SmFeAsO_{1-x}F_x$. Nature, **453**, 761–762 (2008). ◇ Cited on page 10.

64 Kamihara, Y., Watanabe, T., Hirano, M., and Hosono, H. Iron-Based Layered Superconductor $La[O_{1-x}F_x]FeAs$ ($x = 0.05$-0.12) with $T_c = 26$ K. Journal of the American Chemical Society, **130**, 3296–3297 (2008). ◇ Cited on pages 10 & 11.

65 Kreyssig, A., et al. Pressure-induced volume-collapsed tetragonal phase of $CaFe_2As_2$ as seen via neutron scattering. Phys. Rev. B, **78**, 184517 (2008). ◇ Cited on page 10.

66 Huang, Q., Qiu, Y., Bao, W., Green, M. A., Lynn, J. W., Gasparovic, Y. C., Wu, T., Wu, G., and Chen, X. H. Neutron-Diffraction Measurements of Magnetic Order and a Structural Transition in the Parent $BaFe_2As_2$ Compound of FeAs-Based High-Temperature Superconductors. Phys. Rev. Lett., **101**, 257003 (2008). ◇ Cited on page 11.

67 Rotter, M., Tegel, M., and Johrendt, D. Superconductivity at 38 K in the Iron Arsenide $(Ba_{1-x}K_x)Fe_2As_2$. Phys. Rev. Lett., **101**, 107006 (2008). ◇ Cited on page 11.

68 de la Cruz, C., et al. Magnetic order close to superconductivity in the iron-based layered $LaO_{1-x}F_xFeAs$ systems. Nature, **453**, 899–902 (2008). ◇ Cited on pages 11 & 12.

69 Klauss, H.-H., et al. Commensurate Spin Density Wave in LaFeAsO: A Local Probe Study. Phys. Rev. Lett., **101**, 077005 (2008). ◇ Cited on page 11.

70 Krellner, C., Caroca-Canales, N., Jesche, A., Rosner, H., Ormeci, A., and Geibel, C. Magnetic and structural transitions in layered iron arsenide systems: $A\mathrm{Fe_2As_2}$ versus $R\mathrm{FeAsO}$. Phys. Rev. B, **78**, 100504 (2008). ◇ Cited on page 11.

71 Jesche, A., et al. Strong coupling between magnetic and structural order parameters in $SrFe_2As_2$. Phys. Rev. B, **78**, 180504 (2008). ◇ Cited on page 11.

72 Goldman, A. I., Argyriou, D. N., Ouladdiaf, B., Chatterji, T., Kreyssig, A., Nandi, S., Ni, N., Bud'ko, S. L., Canfield, P. C., and McQueeney, R. J. Lattice and magnetic instabilities in $CaFe_2As_2$: A single-crystal neutron diffraction study. Phys. Rev. B, **78**, 100506 (2008). ◇ Cited on page 11.

73 Gen-Fu, C., Zheng, L., Gang, L., Wan-Zheng, H., Jing, D., Jun, Z., Xiao-Dong, Z., Ping, Z., Nan-Lin, W., and Jian-Lin, L. Superconductivity in Hole-Doped $(\mathrm{Sr}_{1-x}\mathrm{K}_x)\mathrm{Fe_2As_2}$. Chinese Physics Letters, **25**, 3403 (2008). ◇ Cited on page 11.

74 Sasmal, K., Lv, B., Lorenz, B., Guloy, A. M., Chen, F., Xue, Y.-Y., and Chu, C.-W. Superconducting Fe-Based Compounds $(A_{1-x}\mathrm{Sr}_x)\mathrm{Fe_2As_2}$ with $A = \mathrm{K}$ and Cs with Transition Temperatures up to 37 K. Phys. Rev. Lett., **101**, 107007 (2008). ◇ Cited on page 11.

75 Ren, Z.-A., et al. Superconductivity and phase diagram in iron-based arsenic-oxides $\mathrm{ReFeAsO}_{1-\delta}$ (Re = rare-earth metal) without fluorine doping. EPL (Europhysics Letters), **83**, 17002 (2008). ◇ Cited on page 11.

76 Kito, H., Eisaki, H., and Iyo, A. Superconductivity at 54 K in F-Free $\mathrm{NdFeAsO}_{1-y}$. Journal of the Physical Society of Japan, **77**, 063707 (2008). ◇ Cited on page 11.

77 Tranquada, J. M. Modulated superfluid density in an iron-pnictide superconductor. Physics, **3**, 41 (2010). ◇ Cited on page 12.

78 Nandi, S., et al. Anomalous Suppression of the Orthorhombic Lattice Distortion in Superconducting $\mathrm{Ba(Fe_{1-x}Co_x)_2As_2}$ Single Crystals. Phys. Rev. Lett., **104**, 057006 (2010). ◇ Cited on page 12.

79 Dong, J., et al. Competing orders and spin-density-wave instability in $\mathrm{La(O_{1-x}F_x)FeAs}$. EPL (Europhysics Letters), **83**, 27006 (2008). ◇ Cited on page 12.

80 Boeri, L., Dolgov, O. V., and Golubov, A. A. Is $\mathrm{LaFeAsO_{1-x}F_x}$ an Electron-Phonon Superconductor? Phys. Rev. Lett., **101**, 026403 (2008). ◇ Cited on page 12.

81 Mazin, I. and Schmalian, J. Pairing symmetry and pairing state in ferropnictides: Theoretical overview. Physica C: Superconductivity, **469**, 614 – 627 (2009). ◇ Cited on pages 12 & 22.

82 D.J. and Singh Electronic structure of Fe-based superconductors. Physica C: Superconductivity, **469**, 418–424 (2009). ◇ Cited on page 12.

83 Yildirim, T. Origin of the 150-K Anomaly in LaFeAsO: Competing Antiferromagnetic Interactions, Frustration, and a Structural Phase Transition. Phys. Rev. Lett., **101**, 057010 (2008). ◇ Cited on page 12.

84 Dai, J., Si, Q., Zhu, J.-X., and Abrahams, E. Iron pnictides as a new setting for quantum criticality. Proceedings of the National Academy of Sciences, **106**, 4118–4121 (2009). ◇ Cited on page 13.

85 Sefat, A. S., Singh, D. J., Jin, R., McGuire, M. A., Sales, B. C., and Mandrus, D. Renormalized behavior and proximity of $BaCo_2As_2$ to a magnetic quantum critical point. Phys. Rev. B, **79**, 024512 (2009). ◇ Cited on page 13.

86 Liu, R. H., et al. Anomalous Transport Properties and Phase Diagram of the FeAs-Based $SmFeAsO_{1-x}F_x$ Superconductors. Phys. Rev. Lett., **101**, 087001 (2008). ◇ Cited on page 13.

87 Luetkens, H., et al. The electronic phase diagram of the $LaO_{1-x}F_xFeAs$ superconductor. Nat Mater, **8**, 305–309 (2009). ◇ Cited on page 13.

88 Grafe, H.-J., et al. ^{75}As NMR Studies of Superconducting $LaFeAsO_{0.9}F_{0.1}$. Phys. Rev. Lett., **101**, 047003 (2008). ◇ Cited on page 13.

89 Matano, K., Ren, Z. A., Dong, X. L., Sun, L. L., Zhao, Z. X., and qing Zheng, G. Spin-singlet superconductivity with multiple gaps in $PrFeAsO_{0.89}F_{0.11}$. EPL (Europhysics Letters), **83**, 57001 (2008). ◇ Cited on page 13.

90 Ning, F., Ahilan, K., Imai, T., Sefat, A. S., Jin, R., McGuire, M. A., Sales, B. C., and Mandrus, D. ^{59}Co and ^{75}As NMR Investigation of Electron-Doped High T_c Superconductor $BaFe_{1.8}Co_{0.2}As_2$ ($T_c = 22\,K$). Journal of the Physical Society of Japan, **77**, 103705 (2008). ◇ Cited on page 13.

91 Uemura, Y. J., et al. Magnetic-field penetration depth in K_3C_{60} measured by muon spin relaxation. Nature, **352**, 605–607 (1991). ◇ Cited on page 13.

92 Hardy, W. N., Bonn, D. A., Morgan, D. C., Liang, R., and Zhang, K. Precision measurements of the temperature dependence of λ in $YBa_2Cu_3O_{6.95}$: Strong evidence for nodes in the gap function. Phys. Rev. Lett., **70**, 3999–4002 (1993). ◇ Cited on pages 13, 14 & 62.

93 Sonier, J. E., et al. New muon-spin-rotation measurement of the temperature dependence of the magnetic penetration depth in $YBa_2Cu_3O_{6.95}$. Phys. Rev. Lett., **72**, 744–747 (1994). ◇ Cited on page 13.

94 Uemura, Y. J., et al. Universal Correlations between T_c and $\frac{n_s}{m^*}$ (Carrier Density over Effective Mass) in High-T_c Cuprate Superconductors. Phys. Rev. Lett., **62**, 2317–2320 (1989). ◇ Cited on page 13.

95 Uemura, Y. J., et al. Basic similarities among cuprate, bismuthate, organic, Chevrel-phase, and heavy-fermion superconductors shown by penetration-depth measurements. Phys. Rev. Lett., **66**, 2665–2668 (1991). ◇ Cited on page 13.

96 Drew, A. J., et al. Coexistence of Magnetic Fluctuations and Superconductivity in the Pnictide High Temperature Superconductor $SmFeAsO_{1-x}F_x$ Measured by Muon Spin Rotation. Physical Review Letters, **101**, 097010 (2008). ◇ Cited on page 13.

97 Franz, M. and Iyengar, A. P. Superfluid Density of Strongly Underdoped Cuprate Superconductors from a Four-Dimensional XY Model. Phys. Rev. Lett., **96**, 047007 (2006). ◇ Cited on page 13.

98 Iulian Hetel, M. R., Thomas R. Lemberger Quantum critical behaviour in the superfluid density of strongly underdoped ultrathin copper oxide films. Nature Physics, **3** (2007). ◇ Cited on page 13.

99 Schrieffer, J. R., Wen, X.-G., and Zhang, S.-C. Spin-bag mechanism of high-temperature superconductivity. Phys. Rev. Lett., **60**, 944–947 (1988). ◇ Cited on page 13.

100 Basov, D. N. and Timusk, T. Electrodynamics of high- T_c superconductors. Rev. Mod. Phys., **77**, 721–779 (2005). ◇ Cited on page 13.

101 Li, W.-H., Lynn, J. W., and Fisk, Z. Magnetic order of the Cu planes and chains in $R\mathrm{Ba_2Cu_3O}_{6+x}$. Phys. Rev. B, **41**, 4098–4111 (1990). ◇ Cited on page 13.

102 Zhang, K., Bonn, D. A., Kamal, S., Liang, R., Baar, D. J., Hardy, W. N., Basov, D., and Timusk, T. Measurement of the ab Plane Anisotropy of Microwave Surface Impedance of Untwinned $YBa_2Cu_3O_{6.95}$ Single Crystals. Phys. Rev. Lett., **73**, 2484–2487 (1994). ◇ Cited on pages 13 & 14.

103 Grabowski, S., Schmalian, J., and Bennemann, K. H. Electronic theory for bilayer-effects in high-t_c superconductors. Physica C: Superconductivity, **282-287**, 1681 – 1682 (1997). ◇ Cited on page 13.

104 Atkinson, W. A. and Sonier, J. E. Role of CuO chains in vortex core structure in $YBa_2Cu_3O_{7-\delta}$. Phys. Rev. B, **77**, 024514 (2008). ◇ Cited on pages 13 & 14.

105 Morr, D. K. and Balatsky, A. V. Proximity Effects and Quantum Dissipation in the Chains of $\mathrm{YBa_2Cu_3}O_{6+x}$. Phys. Rev. Lett., **87**, 247002 (2001). ◇ Cited on page 13.

106 Nunner, T. S. and Hirschfeld, P. J. Microwave conductivity of d-wave superconductors with extended impurities. Phys. Rev. B, **72**, 014514 (2005). ◇ Cited on page 13.

107 Friedmann, T. A., Rabin, M. W., Giapintzakis, J., Rice, J. P., and Ginsberg, D. M. Direct measurement of the anisotropy of the resistivity in the a-b plane of twin-free, single-crystal, superconducting $YBa_2Cu_3O_{7-\delta}$. Phys. Rev. B, **42**, 6217–6221 (1990). ◇ Cited on page 14.

108 Gagnon, R., Lupien, C., and Taillefer, L. T^2 dependence of the resistivity in the Cu-O chains of $YBa_2Cu_3O_{6.9}$. Phys. Rev. B, **50**, 3458–3461 (1994). ◇ Cited on page 14.

109 Basov, D. N., Liang, R., Bonn, D. A., Hardy, W. N., Dabrowski, B., Quijada, M., Tanner, D. B., Rice, J. P., Ginsberg, D. M., and Timusk, T. In-Plane Anisotropy of the Penetration Depth in $YBa_2Cu_3O_{7-\delta}$ and $YBa_2Cu_4O_8$ Superconductors. Phys. Rev. Lett., **74**, 598–601 (1995). ◇ Cited on pages 14 & 67.

110 Gros, C., Joynt, R., and Rice, T. M. Superconducting instability in the large-U limit of the two-dimensional Hubbard model. Zeitschrift für Physik B Condensed Matter, **68**, 425–432 (1987). ◇ Cited on page 14.

111 Weng, Z. Y., Lee, T. K., and Ting, C. S. d-wave superconducting condensation in the spin-density-wave background. Phys. Rev. B, **38**, 6561–6567 (1988). ◇ Cited on page 14.

112 Monthoux, P., Balatsky, A. V., and Pines, D. Toward a theory of high-temperature superconductivity in the antiferromagnetically correlated cuprate oxides. Phys. Rev. Lett., **67**, 3448–3451 (1991). ◇ Cited on page 14.

113 Annett, J., Goldenfeld, N., and Renn, S. R. Interpretation of the temperature dependence of the electromagnetic penetration depth in $YBa_2Cu_3O_{7-\delta}$. Phys. Rev. B, **43**, 2778–2782 (1991). ◇ Cited on page 14.

114 Annet, J. F., Goldenfeld, N., and Renn, S. R. Physical properties of high temperature superconductors II, edited by D. M. Ginsberg. World Scientific (1989). ◇ Cited on page 14.

115 C. P. Poole, H. A. F. and Creswick, R. J. Superconductivity. Academic press, 2nd ed. edn. (1995). ◇ Cited on page 14.

116 Suter, A., Morenzoni, E., Khasanov, R., Luetkens, H., Prokscha, T., and Garifianov, N. Direct Observation of Nonlocal Effects in a Superconductor. Phys. Rev. Lett., **92**, 087001 (2004). ◇ Cited on page 14.

117 Amin, M. H. S., Affleck, I., and Franz, M. Low-temperature behavior of the vortex lattice in unconventional superconductors. Phys. Rev. B, **58**, 5848–5855 (1998). ◇ Cited on page 14.

118 Sonier, J. E., Hundley, M. F., Thompson, J. D., and Brill, J. W. Low Field Anomaly in the Specific Heat of s-Wave Superconductors due to the Expansion of the Vortex Cores. Phys. Rev. Lett., **82**, 4914–4917 (1999). ◇ Cited on page 14.

119 Sonier, J. E., Brewer, J. H., and Kiefl, R. F. μSR studies of the vortex state in type-II superconductors. Rev. Mod. Phys., **72**, 769–811 (2000). ◇ Cited on page 14.

120 Maisuradze, A., Khasanov, R., Shengelaya, A., and Keller, H. Comparison of different methods for analyzing μSR line shapes in the vortex state of type-II superconductors. Journal of Physics: Condensed Matter, **21**, 075701 (15pp) (2009). ◇ Cited on page 14.

121 Sonier, J. E., et al. Hole-doping dependence of the magnetic penetration depth and vortex core size in $YBa_2Cu_3O_{6+x}$: Evidence for stripe correlations near (1/8) hole doping. Physical Review B (Condensed Matter and Materials Physics), **76**, 134518 (2007). ◇ Cited on pages 14 & 67.

122 Sonier, J. E., Kiefl, R. F., Brewer, J. H., Chakhalian, J., Dunsiger, S. R., MacFarlane, W. A., Miller, R. I., Wong, A., Luke, G. M., and Brill, J. W. Muon-Spin Rotation Measurements of the Magnetic Field Dependence of the Vortex-Core Radius and Magnetic Penetration Depth in $NbSe_2$. Phys. Rev. Lett., **79**, 1742–1745 (1997). ◇ Cited on page 14.

123 Fiory, A. T., Hebard, A. F., Mankiewich, P. M., and Howard, R. E. Renormalization of the Mean-Field Superconducting Penetration Depth in Epitaxial $YBa_2Cu_3O_7$ Films. Phys. Rev. Lett., **61**, 1419–1422 (1988). ◇ Cited on page 14.

124 Ma, Z., Taber, R. C., Lombardo, L. W., Kapitulnik, A., Beasley, M. R., Merchant, P., Eom, C. B., Hou, S. Y., and Phillips, J. M. Microwave penetration depth measurements on $Bi_2Sr_2CaCu_2O_8$ single crystals and $YBa_2Cu_3O_{7-\delta}$ thin films . Phys. Rev. Lett., **71**, 781–784 (1993). ◇ Cited on page 14.

125 Klein, N., Tellmann, N., Schulz, H., Urban, K., Wolf, S. A., and Kresin, V. Z. Evidence of two-gap *s*-wave superconductivity in $YBa_2Cu_3O_{7-\delta}$ from microwave surface impedance measurements. Phys. Rev. Lett., **71**, 3355–3358 (1993). ◇ Cited on page 14.

126 Gorter, C. *Paramagnetic Relaxation*, vol. 1 of Course of Theoretical Physics. Elsevier, second edn. (1947). ◇ Cited on page 17.

127 Blatt, F. Modern physics. Physics series, McGraw-Hill (1992). ◇ Cited on page 17.

128 Yang, C. N. Concept of Off-Diagonal Long-Range Order and the Quantum Phases of Liquid He and of Superconductors. Rev. Mod. Phys., **34**, 694–704 (1962). ◇ Cited on pages 20 & 21.

129 Nieh, H. T., Su, G., and Zhao, B.-H. Off-diagonal long-range order: Meissner effect and flux quantization. Phys. Rev. B, **51**, 3760–3764 (1995). ◇ Cited on page 20.

130 Sewell, G. L. Off-diagonal long-range order and the Meissner effect. Journal of Statistical Physics, **61**, 415–422 (1990). ◇ Cited on page 21.

131 Fisher, M. P. A. Vortex-glass superconductivity: A possible new phase in bulk high-T_c oxides. Phys. Rev. Lett., **62**, 1415–1418 (1989). ◇ Cited on page 21.

132 Kuroki, K., Onari, S., Arita, R., Usui, H., Tanaka, Y., Kontani, H., and Aoki, H. Unconventional Pairing Originating from the Disconnected Fermi Surfaces of Superconducting $LaFeAsO_{1-x}F_x$. Phys. Rev. Lett., **101**, 087004 (2008). ◇ Cited on page 21.

133 Sigrist, M. and Rice, T. M. Symmetry classification of states in high temperature superconductors. Zeitschrift für Physik B Condensed Matter, **68**, 9–14 (1987). ◇ Cited on page 21.

134 Wenger, F. and Östlund, S. *d*-wave pairing in tetragonal superconductors. Phys. Rev. B, **47**, 5977–5983 (1993). ◇ Cited on page 21.

135 Li, Q. P., Koltenbah, B. E. C., and Joynt, R. Mixed *s*-wave and *d*-wave superconductivity in high-T_c systems. Phys. Rev. B, **48**, 437–455 (1993). ◇ Cited on page 21.

136 Zhang, S.-C. A Unified Theory Based on SO(5) Symmetry of Superconductivity and Antiferromagnetism. Science, **275**, 1089–1096 (1997). ◇ Cited on page 21.

137 Kirtley, J. R., Tsuei, C. C., Ariando, Verwijs, C. J. M., Harkema, S., and Hilgenkamp, H. Angle-resolved phase-sensitive determination of the in-plane gap symmetry in $YBa_2Cu_3O_{7-\delta}$. Nat Phys, **2**, 190–194 (2006). ◇ Cited on page 21.

138 Kirtley, J. R., Tsuei, C. C., Sun, J. Z., Chi, C. C., Yu-Jahnes, L. S., Gupta, A., Rupp, M., and Ketchen, M. B. Symmetry of the order parameter in the high-T_c superconductor $YBa_2Cu_3O_{7-\delta}$. Nature, **373**, 225–228 (1995). ◇ Cited on page 21.

139 Tsuei, C. C., Kirtley, J. R., Hammerl, G., Mannhart, J., Raffy, H., and Li, Z. Z. Robust $d_{x^2-y^2}$ Pairing Symmetry in Hole-Doped Cuprate Superconductors. Phys. Rev. Lett., **93**, 187004 (2004). ◇ Cited on page 21.

140 Mazin, I. I. Superconductivity gets an iron boost. Nature, **464**, 183–186 (2010). ◇ Cited on page 22.

141 Mazin, I. I., Singh, D. J., Johannes, M. D., and Du, M. H. Unconventional Superconductivity with a Sign Reversal in the Order Parameter of $LaFeAsO_{1-x}F_x$. Phys. Rev. Lett., **101**, 057003 (2008). ◇ Cited on page 22.

142 Riseman, T. Ph.D. Thesis: μSR MEASUREMENT OF THE MAGNETIC PENETRATION DEPTH AND COHERENCE LENGTH IN THE HIGH-T_C SUPERCONDUCTOR $YBa_2Cu_3O_{6.95}$. University Of British Columbia (1993). ◇ Cited on page 26.

143 Morris, G. Ph.D. Thesis: Muonium Formation and Diffusion in Cryocrystals. University Of British Columbia (1997). ◇ Cited on page 26.

144 Nakamura, K. and Group, P. D. Review of Particle Physics. Journal of Physics G: Nuclear and Particle Physics, **37**, 075021 (2010). ◇ Cited on page 26.

145 Schenck, A. Muon Spin Spectroscopy. Hilger, Bristol (1985). ◇ Cited on page 26.

146 Cox, S. F. J. Implanted muon studies in condensed matter science. Journal of Physics C: Solid State Physics, **20**, 3187 (1987). ◇ Cited on page 26.

147 Keller, H. Muon-spin rotation experiments in high-T_c superconductors and related materials. IBM Journal of Research and Development, **33**, 314 –323 (1989). ◇ Cited on page 26.

148 Chow, K. Ph.D. Thesis: Spin dynamics and electronic structure of muonium and its charged states in silicon and gallium arsenide. University Of British Columbia (1994). ◇ Cited on page 26.

149 Luke, G. Ph.D. Thesis: Quantum diffusion and spin dynamics of muons in copper. University Of British Columbia (1988). ◇ Cited on page 26.

150 Prokscha, T., Morenzoni, E., Deiters, K., Foroughi, F., George, D., Kobler, R., Suter, A., and Vrankovic, V. The new μE4 beam at PSI: A hybrid-type large acceptance channel for the generation of a high intensity surface-muon beam. Nuclear Instruments and Methods in Physics Research Section A: Accelerators, Spectrometers, Detectors and Associated Equipment, **595**, 317 – 331 (2008). ◇ Cited on page 26.

151 Luetkens, K. Ph.D. Thesis. Gemeinsamen Naturwissenschaftlichen Fakultt der Technischen Universitat Carolo-Wilhelmina zu Braunschweig (2004). ◇ Cited on pages 27 & 28.

152 Morenzoni, E., Glückler, H., Prokscha, T., Khasanov, R., Luetkens, H., Birke, M., Forgan, E. M., Niedermayer, C., and Pleines, M. Implantation studies of kev positive muons in thin metallic layers. Nuclear Instruments and Methods in Physics Research Section B: Beam Interactions with Materials and Atoms, **192**, 254 – 266 (2002). ◇ Cited on pages 27 & 32.

153 Ziegler, J. F. (2011), The stopping and range of ions in matter. ◇ Cited on page 31.

154 Eckstein, W. Computer Simulation of Ion-Solid Interactions. Springer, Berlin (1991). ◇ Cited on page 31.

155 Morenzoni, E., Prokscha, T., Suter, A., Luetkens, H., and Khasanov, R. Nano-scale thin film investigations with slow polarized muons. Journal of Physics: Condensed Matter, **16**, S4583 (2004). ◇ Cited on page 32.

156 Liang, R., Bonn, D. A., and Hardy, W. N. Growth of high quality YBCO single crystals using BaZrO3 crucibles. Physica C: Superconductivity, **304**, 105 – 111 (1998). ◇ Cited on page 34.

157 Doiron-Leyraud, N., Proust, C., LeBoeuf, D., Levallois, J., Bonnemaison, J.-B., Liang, R., Bonn, D. A., Hardy, W. N., and Taillefer, L. Quantum oscillations and the Fermi surface in an underdoped high-T_c superconductor. Nature Publishing Group, **447**, 565–568 (2007). ◇ Cited on page 34.

158 Riseman, T. and Forgan, E. Maximum entropy μSR analysis i: planting the kernel. Physica B: Condensed Matter, **326**, 226 – 229 (2003). ◇ Cited on page 36.

159 Riseman, T. and Forgan, E. Maximum entropy μSR analysis ii: the search for truthful errors. Physica B: Condensed Matter, **326**, 230 – 233 (2003). ◇ Cited on page 36.

160 Riseman, T. and Forgan, E. Maximum entropy μSR analysis iii: automatic selection of the default level and looseness factor. Physica B: Condensed Matter, **326**, 234 – 237 (2003). ◇ Cited on page 36.

161 Wojek, B. M. Superconductivity and magnetism in cuprate single crystals and thin-film heterostructures. Ph.D. thesis, University of Zurich (2011). ◇ Cited on page 37.

162 Jackson, T. J., et al. Depth-Resolved Profile of the Magnetic Field beneath the Surface of a Superconductor with a Few nm Resolution. Phys. Rev. Lett., **84**, 4958–4961 (2000). ◇ Cited on pages 40 & 67.

163 Ni, N., Tillman, M. E., Yan, J.-Q., Kracher, A., Hannahs, S. T., Bud'ko, S. L., and Canfield, P. C. Effects of Co substitution on thermodynamic and transport properties and anisotropic H_{c2} in $BaCo_xFe_{2-x}As_2$ single crystals. Phys. Rev. B, **78**, 214515 (2008). ◇ Cited on page 58.

164 Kim, H., et al. London penetration depth in $Ba(T_xFe_{1-x})_2As_2$(T=Co, Ni) superconductors irradiated with heavy ions. Phys. Rev. B, **82**, 060518 (2010). ◇ Cited on page 62.

165 Gordon, R. T., et al. Unconventional London Penetration Depth in Single-Crystal $Ba(Co_{0.07}Fe_{0.93})_2As_2$ Superconductors. Phys. Rev. Lett., **102**, 127004 (2009). ◇ Cited on page 62.

166 Luan, L., Auslaender, O. M., Lippman, T. M., Hicks, C. W., Kalisky, B., Chu, J.-H., Analytis, J. G., Fisher, I. R., Kirtley, J. R., and Moler, K. A. Local measurement of the penetration depth in the pnictide superconductor $Ba(Co_{0.05}Fe_{0.95})_2As_2$. Phys. Rev. B, **81**, 100501 (2010). ◇ Cited on pages 62 & 67.

167 Gross, F., Chandrasekhar, B. S., Einzel, D., Andres, K., Hirschfeld, P. J., Ott, H. R., Beuers, J., Fisk, Z., and Smith, J. L. Anomalous temperature dependence of the magnetic field penetration depth in superconducting UBe_{13}. Zeitschrift für Physik B Condensed Matter, **64**, 175–188 (1986). ◇ Cited on page 63.

168 Williams, T. J., et al. Muon spin rotation measurement of the magnetic field penetration depth in $Ba(Co_{0.074}Fe_{0.926})_2As_2$: Evidence for multiple superconducting gaps. Phys. Rev. B, **80**, 094501 (2009). ◇ Cited on page 63.

169 Sonier, J. E., et al. Magnetism and Disorder Effects on Muon Spin Rotation Measurements of the Magnetic Penetration Depth in Iron-Arsenic Superconductors. Phys. Rev. Lett., **106**, 127002 (2011). ◇ Cited on page 63.

170 Kogan, V. G., Martin, C., and Prozorov, R. Superfluid density and specific heat within a self-consistent scheme for a two-band superconductor. Phys. Rev. B, **80**, 014507 (2009). ◇ Cited on page 63.

171 Pereg-Barnea, T., Turner, P. J., Harris, R., Mullins, G. K., Bobowski, J. S., Raudsepp, M., Liang, R., Bonn, D. A., and Hardy, W. N. Absolute values of the London penetration depth in $YBa_2Cu_3O_{6+x}$ measured by zero field ESR spectroscopy on Gd doped single crystals. Phys. Rev. B, **69**, 184513 (2004). ◇ Cited on page 67.

172 Ager, C., et al. Angular-dependent muon-spin rotation and torque magnetometry on the mixed state of the high-temperature superconductor $YBa_2Cu_3O_{6+x}$. Phys. Rev. B, **62**, 3528–3533 (2000). ◇ Cited on page 67.

173 Johnson, S. T., et al. Flux-Line Lattice Structures in Untwinned $YBa_2Cu_3O_{6+x}$. Phys. Rev. Lett., **82**, 2792–2795 (1999). ◇ Cited on page 67.

174 Prozorov, R., Tanatar, M., Gordon, R., Martin, C., Kim, H., Kogan, V., Ni, N., Tillman, M., Bud'ko, S., and Canfield, P. Anisotropic london penetration depth and superfluid density in single crystals of iron-based pnictide superconductors. Physica C: Superconductivity, **469**, 582 – 589 (2009). ◇ Cited on page 67.

175 Luan, L., Lippman, T. M., Hicks, C. W., Bert, J. A., Auslaender, O. M., Chu, J.-H., Analytis, J. G., Fisher, I. R., and Moler, K. A. Local Measurement of the Superfluid Density in the Pnictide Superconductor $BaCo_xFe_{2-x}As_2$ across the Superconducting Dome. Phys. Rev. Lett., **106**, 067001 (2011). ◇ Cited on page 67.

176 Lindstrom, M. Asymptotic and numerical modeling of magnetic field profiles in superconductors with rough boundaries and multi-component gas transport in PEM fuel cells. University Of British Columbia (2010). ◇ Cited on page 68.

177 Aeppli, G., Ansaldo, E. J., Brewer, J. H., Cava, R. J., Kiefl, R. F., Kreitzman, S. R., Luke, G. M., and Noakes, D. R. Magnetic penetration depth and flux-pinning effects in high-T_c superconductor $La_{1.85}Sr0_{.15}CuO$. Phys. Rev. B, **35**, 7129–7132 (1987). ◇ Cited on page 68.

178 Huebener, R. P. Flux Structures in Superconductors. Springer (2001). ◇ Cited on page 68.

179 Konczykowski, M., Burlachkov, L. I., Yeshurun, Y., and Holtzberg, F. Evidence for surface barriers and their effect on irreversibility and lower-critical-field measurements in Y-Ba-Cu-O crystals. Phys. Rev. B, **43**, 13707–13710 (1991). ◇ Cited on page 68.

180 Dolan, G. J., Holtzberg, F., Feild, C., and Dinger, T. R. Anisotropic vortex structure in $YBa_2Cu_3O_7$. Phys. Rev. Lett., **62**, 2184–2187 (1989). ◇ Cited on page 68.

181 Jooss, C., Forkl, A., Warthmann, R., Habermeier, H. U., Leibold, B., and Kronmüller, H. Thickness and roughness dependence of magnetic flux penetration and critical current densities in $YBa_2Cu_3O_{7-\delta}$ thin films. Physica C: Superconductivity, **266**, 235 – 252 (1996). ◇ Cited on page 68.